מכון ויצמן למדע
WEIZMANN INSTITUTE OF SCIENCE

Thesis for the degree
Doctor of Philosophy

עבודת גמר (תזה) לתואר
דוקטור לפילוסופיה

Submitted to the Scientific Council of the
Weizmann Institute of Science
Rehovot, Israel

מוגשת למועצה המדעית של
מכון ויצמן למדע
רחובות, ישראל

By
Mirta Dumancic

מאת
מירטה דומנצ׳יץ׳

יצרת בוזון מסוג Z בהתנגשויות של פרוטון-פרוטון ושל עופרת-עופרת באנרגיה של 5.02 TeV בניסוי ATLAS ב LHC

Z boson production in 5.02 TeV proton-proton and lead-lead data measured by the ATLAS experiment at the LHC

Advisor:
Prof. Alexander Milov

מנחה:
פרופ׳ אלכסנדר מילוב

October 2019

תשרי תש״פ

Acknowledgments

I acknowledge the essential help from my advisor Prof. Alexander Milov during all the years of my graduate program. I am grateful for all the transferred knowledge and many opportunities to be a part of the scientific work at the front of what is currently studied by the heavy-ion physics community. I acknowledge all the work and help from Prof. Zvi Citron (BGU, Israel) who worked with me during my early years here at the Weizmann Institute and helped to bring to completion the results presented in this thesis. Specifically, Zvi worked on the muon reconstruction performance in the Pb+Pb system. I am very grateful to all of my other colleagues in the WIS HI group that made these Ph.D. years fun and interesting - to Markus, Sourav, Petr, Anna, Zhenia and Yasha. I thank Pierre Choukroun for all of his help and availability in solving computing problems.

Working as a member of the ATLAS Collaboration allowed me to meet many respectable scientists, young as well as established. I would like to thank Peter Steinberg (BNL, USA) for his patience and mentorship in working with photon triggers and for many discussions we had related to UPC physics. Special thanks to Jakub Kremer (AGH Krakow, Poland) who worked on the muon reconstruction performance measurements in the pp system. For the theoretical calculations of the Z-boson cross section in pp and Pb+Pb systems, I owe special thanks to Piotr Janus (AGH Krakow, Poland) and Fabrice Balli (IRFU Saclay, France). I acknowledge the expertise and work done by Maarten Boonekamp (IRFU Saclay, France) on the combined Z and W cross section in pp collisions. Working with you was a real privilege.

I thank my family and friends who supported me during my years here at the Weizmann Institute. Mum, dad and my sister Iva - thank you for all the encouragement you provided in love and care. Many thanks to my roommates Lisha, Karen, Qian and Carol for all the comforting conversations and meals we had together; to my friends Heidi, Deb, Lora and Yael, who were there when I needed you and much more; to Tobias for his patience and help with putting this thesis together; to Kevin, Sonu, Carol and Dahvyd who did some painful proofreading. I am so thankful for all of you who are an essential part of my journey.

Once again, thank you all for fruitful years of work, research and friendship that brought forth this final result. And beyond that - it taught me both science and life that I will always carry with me.

Declaration

I hereby declare that except where specific reference is made to the work of others, the contents of this thesis are original and have not been submitted in whole or in part for consideration for any other degree or qualification in this, or any other university. This thesis is my work and contains nothing which is the outcome of work done in collaboration with others, except as specified in the text and Acknowledgements.

Mirta Dumančić

Contents

Abbreviations

ALICE A Large Ion Collider Experiment.

ATLAS A Toroidal LHC Apparatus.

CERN European Organization for Nuclear Research (French: *Conseil Européen pour la Recherche Nucléaire*).

CKM Cabibbo–Kobayashi–Maskawa.

CMS Compact Muon Solenoid.

CNM Cold Nuclear Matter.

CSC Cathode-Strip Chambers.

DGLAP Dokshitzer-Gribov-Lipatov-Altarelli-Parisi.

DIS Deep-Inelastic Scattering.

EM Electromagnetic.

EMC European Muon Collaboration.

EW Electroweak.

FCal Forward Calorimeter.

GMC Glauber Monte Carlo.

HEC Hadronic End-Cap Calorimeter.

HERA Hadron-Electron Ring Accelerator (German: *Hadron-Elektron-Ringanlage*).

HI Heavy Ion.

HLT High-Level Trigger.

ID Inner Detector.

LAr Liquid Argon.

LEP Large Electron–Positron Collider.

LHC Large Hadron Collider.

LHCb Large Hadron Collider beauty.

MB Minimum-Bias.

MC Monte Carlo.

MDT Monitored Drift Tubes.

MS Muon Spectrometer.

NLO Next-to-Leading-Order.

NNLO Next-to-Next-to-Leading-Order.

nPDF Nuclear Parton Distribution Function.

PDF Parton Distribution Function.

pQCD Perturbative Quantum Chromodynamics.

QCD Quantum Chromodynamics.

QED Quantum Electrodynamics.

QGP Quark-Gluon Plasma.

RHIC Relativistic Heavy Ion Collider.

RPC Resistive Plate Chamber.

SCT Silicon-Microstrip Detector.

SF Scale Factor.

SM Standard Model.

TGC Thin Gap Chambers.

TileCal Tile Hadronic Calorimeter.

TRT Transition Radiation Tracker.

UPC Ultra-Peripheral Collisions.

ZDC Zero-Degree Calorimeter.

Abstract

The study of electroweak bosons in proton–proton, proton–nucleus and nucleus–nucleus collisions provide an important insight into initial state effects of hadron and nuclear collisions, such as collision geometry and modification of parton distribution functions. This research focuses on studying the Z boson production in Run-2 data collected with the ATLAS detector at the Large Hadron Collider. Measurements are obtained with the data from proton–proton and nucleus–nucleus collisions at a center-of-mass energy of 5.02 TeV per nucleon pair. Fiducial Z-boson cross section in proton-proton data is measured in electron and muon decay channels. The combined cross section is found to be in good agreement with next-to-next-to-leading-order QCD calculations. Rapidity differential cross section is found to agree with calculations within 1 to 2 standard deviations, with the biggest discrepancy measured in the rapidity region $|y| < 1$. The results from the pp system are used to form the nuclear modification factor of the previously measured Z-boson cross section in p+Pb collisions. The nuclear modification factor, measured as a function of Z boson rapidity, shows an asymmetry qualitatively consistent with nuclear modification of the parton distribution functions. This asymmetry is more pronounced in central p+Pb collisions compared to peripheral events. In the Pb+Pb system, the Z-boson differential cross section is measured in electron and muon decay channels as a function of dilepton rapidity and event centrality. The measurements in Pb+Pb collisions are compared with the measured proton–proton results. The nuclear modification factor is found to be consistent with unity in central and mid-central collisions. After rejecting photon-induced backgrounds, the nuclear modification factor in peripheral collisions is found to be above unity, although consistent with it. The results are compared with theoretical predictions obtained at next-to-leading-order using proton and nuclear par-

ton distribution functions. The measured Z boson yields in Pb+Pb collisions lie about 1 to 3 standard deviations above the predictions. The nuclear modification factor measured as a function of rapidity agrees with unity while showing a trend consistent with next-to-leading-order QCD calculation including the isospin effect.

1 Introduction

An overarching quest in the field of nuclear physics is to determine the exact form and different regimes of the strong force. Exploring the phase diagram of nuclear matter in the high-temperature region became possible in the particle accelerator era starting with first experiments at Bevatron (Lawrence Berkeley National Laboratory, USA) and in Dubna (Joint Institute for Nuclear Research, Russia) in the 1950s. With the development of the collider technology in the 1960s and the first hadronic machine in 1971 (Intersecting Storage Rings at CERN) it became feasible to reach higher collision energies for heavy-ion (HI) systems and hence to explore new regimes of nuclear matter in unprecedented experimental conditions.

With high enough ion collision energies (roughly 200 GeV per nucleon pair), strong experimental evidence shows that the nuclear system transitions into a new color deconfined phase. The system behaves as a strongly interacting plasma of quarks and gluons (sQGP) that allows us for the first time to study the collective behavior of these partons. At the Large Hadron Collider (LHC), this new phase of matter is studied at the highest reached temperature known to this day. As currently understood and confirmed by lattice gauge theory calculations, the phase transition to QGP occurs at zero baryon chemical potential via a crossover.

Valuable tools in studying the hot dense medium formed in HI collisions are electroweak (EW) probes. They include high-energy isolated photons and heavy vector bosons, Z and W. These particles are produced in collisions with a high momentum transfer, which are only possible in the interactions of the participating nucleons inside the colliding ions in the initial stage of the collision. Z and W bosons decay much faster compared to the quark-gluon plasma evolution timescale while also their leptonic decay products do not interact with the medium. Therefore, being immune to the strong interaction, these probes carry the information about the initial stage of the collision, the geometry and the parton dynamics inside the colliding nuclei. This Ph.D. research project focuses on measuring the Z boson production in the dilepton decay mode in different collisions systems using the ATLAS detector at the LHC.

By measuring the integrated and differential cross sections of EW probes in nucleus-nucleus (A+A), proton-nucleus (p+A), and proton-proton (pp) collisions at the same center-of-mass energy, one can extract the information about the initial state of the collision and the role of cold nuclear matter (CNM) effects as opposed to the ones coming from the QGP medium evolution. The ratio of cross sections for the EW observable measured in different systems allows extracting nuclear effects present in colliding systems involving ions. It is important to note that such a ratio is now available for the first time for the Z boson production measurement due to the high enough luminosity and collision energy delivered by the LHC machine. The measurement in the pp system is at the same time an important contribution to the Standard Model program of precision measurements at the LHC. Combined with a W-boson cross section measurement, one can derive W/Z boson ratios as an important test of the theory of the perturbative QCD.

The Z boson production occurs via hard scattering of two initial partons. The kinematics of this process depends on the fraction of the nucleon momentum x carried by each of the two partons. The probability density of the momentum distribution for partons at a given momentum transfer (Q^2) is defined as the parton distribution function, PDF(x, Q^2). To this day there exists ample experimental evidence that shows that the PDF of nucleons in a bound state does not correspond to a mere convolution of all the free constituent nucleon PDFs, but rather a new set of probability distribution functions needs to be derived from the nuclear collision data. There are different CNM effects observed inside the nucleus that are categorized as *shadowing*, *anti-shadowing*, the *EMC effect* and the *Fermi motion* [1–3]), depending on the region of x-values probed by the measurement. Deriving the free proton PDFs as well as the nuclear PDFs (nPDFs) consists of obtaining global fits to the measured data from fixed-target or collider experiments. A particular observable sensitive to the (n)PDF distribution is the differential cross section of Z bosons measured as a function of rapidity. The experimental distributions in data can further be used by theorists for the next iteration of (n)PDF fits.

The measurement of Z bosons can be used to study the agreement of the Glauber model [4] with data. This model of describing multi-particle scattering processes is used by all HI experiments to estimate the initial collision geometry. The model further introduces the number of participants N_{part} and relates it to the number of binary collisions N_{coll} and other geometrical quantities. Within the numerical implementation of the Glauber Monte Carlo model (GMC) these geometric quantities can be mapped onto a detector observable such as the total energy measured in the forward rapidity which is used by

ATLAS. By measuring Z boson production yields, unaffected by the medium produced in HI collisions, the GMC model can undergo the highest scrutiny test and its results then can be used for all other measurements that require the knowledge of the initial geometry in HI collisions. For the first time in this work, the Z boson measurement is extended to the ultra-peripheral centrality region where additional physical processes that do not enter Glauber modeling need to be considered.

The thesis is organized in the following way: In Chapter 2 we introduce the theoretical background and the physics motivation for the research project; Chapter 3 discusses the experimental characteristics of the ATLAS detector at the LHC and some of the main methods and observables employed in the measurement; later on, in Chapter 4, we present an overview of the current experimental results on EW boson production; in Chapter 5 we present a detailed measurement procedure for extracting final results in three collision systems presented in Chapter 6. Finally, In Chapter 7 we discuss the impact of results presented in this work in the context of the current status of the field and their contribution in the light of new upcoming experiments.

2 Theoretical background

In this chapter, we introduce the main physics questions related to the understanding of the hot and dense nuclear matter, commonly referred to as Quark-Gluon Plasma. Both from the applied theoretical standpoint and the experiment, it remains challenging to properly characterize this state of matter. After introducing general features of the QGP in Section 2.1, in Section 2.2 we motivate using heavy vector bosons to access the information about the nuclear system contained in the initial stage of the collision before entering the regime of the QGP thermodynamic expansion. The main theoretical quantity accessed by measurements of heavy bosons is the distribution of quark momenta inside the colliding nuclei, namely the Parton Distribution Function described in Section 2.3. Later on, in Section 2.4 we derive the geometrical model used for describing the many-body scattering occurring in HI collisions also known as the Glauber model. In that context, we further introduce the centrality parameter and the model expectation for the hard-scattering production yield that is of particular interest in the Z boson measurement.

2.1 Quark Gluon Plasma

Ultra-relativistic HI collisions serve as an experimental method for exploring high-temperature regions of the nuclear phase diagram and theoretical predictions of the quantum chromodynamics (QCD). The main challenge to the theory is the non-perturbative regime of the strong coupling for which no overarching analytical framework is developed which gave rise to many model descriptions used today. Even though the QCD thermodynamics [5] and lattice QCD [6] have greatly advanced since the 1960s [7], there are still many open questions regarding the description of the hot nuclear matter. After discovering the asymptotic freedom of the strongly interacting matter [8], it was predicted that there should exist a state in which interactions between quarks and gluons become weaker. That state was later referred to as Quark-Gluon Plasma. At high enough energy density accessible at hadron colliders it is anticipated that the hadronic matter (containing confined colored partons) undergoes a phase transition shown in Figure 1, where different phases of nuclear matter are illustrated as a function of the baryon chemical potential μ_B (essentially the difference in the number of quarks and antiquarks) and the system temperature.

At LHC collider energies, which is the case for this study, the energy is sufficiently high so that the produced amount of particles overrides the initial excess in baryon number coming from the colliding nuclei, especially at midrapidity. Therefore, a balanced amount of produced quark and antiquark pairs yields essentially $\mu_B \approx 0$, while the produced system has high energy density and temperature, around 300 MeV (derived from measurements of thermal radiation [9]). This is almost twice of the critical value T_c predicted by lattice QCD calculations [10] and previously motivated by simple fermion gas models [11] or more than the Hagedorn critical temperature for hadronic matter [12]. Using simple calculations for the fermion gas [11], the energy density of the quark-gluon matter created at temperature $T = 300$ MeV is $\epsilon = \frac{37}{30}\pi^2 T^4$, which yields 16.5 GeV/fm^3 for 3 quark flavors. Similarly, the baryon number density of the medium is given by $n_B = \frac{27}{6\pi^2}\zeta(3)T^3$, which gives $n_B = 1.93/\text{fm}^3$. This is around 14 times larger than the nucleon number density of ordinary nuclear matter $n_B = 0.14/\text{fm}^3$.

Intense studies of the medium created in HI collisions at the Super Proton Synchrotron at CERN and Alternating Gradient Synchrotron at Brookhaven and finally at the Relativistic Heavy Ion Collider (RHIC) lead to a discovery of the strongly interacting plasma

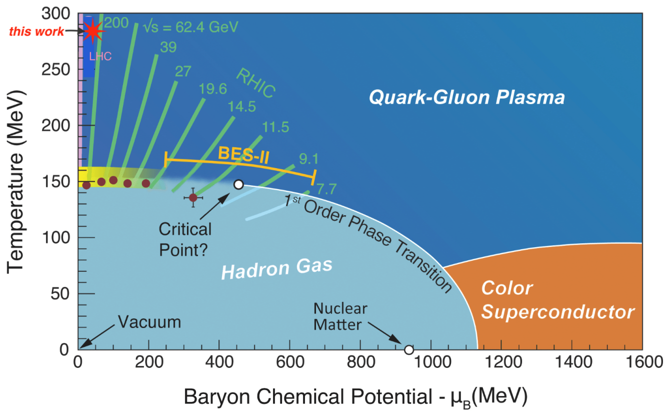

Figure 1: A proposed phase diagram of nuclear matter as a function of the baryon chemical potential and temperature of the system. The lines of medium evolution corresponding to different collision energies for RHIC and LHC are drawn in green and violet, respectively. The region of the phase space explored with the Beam Energy Scan program (BES) at RHIC is denoted with a yellow line. A point in the diagram that approximately corresponds to the system studied in this work is denoted in the figure with a red star. (Figure adapted from https://deixismagazine.org/2016/06/early-universe-soup/.)

(sQGP) [13–16], in contrast to the previously expected gas-like nuclear matter [17]. The order of the phase transition and whether there exists a critical point are still open questions addressed by experiments at RHIC [18] and future projects such as NICA and FAIR. The region of phase space explored in this work in denoted in Figure 1 and it suggests strongly that at the high energies achieved at the LHC, the system undergoes a crossover transition from the QGP phase to a hadronic gas phase.

The evolution of nuclear matter after the collision is illustrated in Figure 2. At the initial state of the collision, highly energetic partons interact via hard scattering (parton–parton interaction with a large transfer momentum) and produce energetic probes in the final state such as jets and electroweak (EW) bosons. Subsequently, a thermalized system of quarks and gluons (QGP) is formed over time comparable to the time of the ion–ion interaction (5–10 fm/c). The liquid then expands and cools following relativistic hydrodynamics until the crossover phase transition occurs at 155 MeV when the plasma hydronizes ("chemical freeze-out"). The produced hadronic system then continues to interact, expand and cool until the temperature falls to about 95 MeV when the interactions between hadrons cease ("thermal freeze-out") and they finally reach the detector [19].

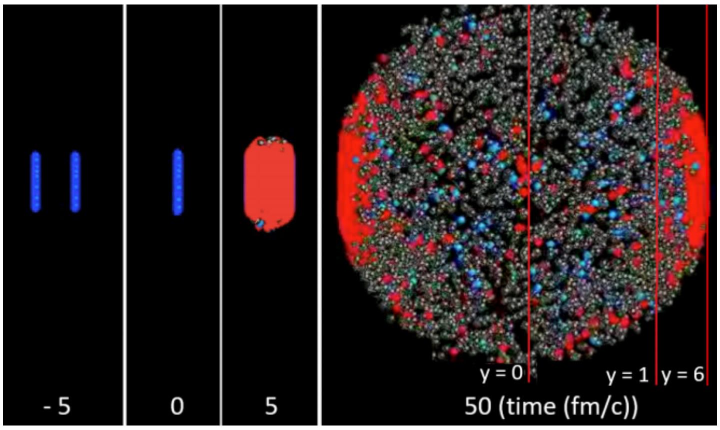

Figure 2: Snapshots of a central 2.76 TeV Pb+Pb collision at different times (different horizontal slices of the space-time picture) with hadrons presented with blue and grey spheres and QGP in red. At a given time the hottest regions can be found at high rapidity close to the outgoing remnants of the nuclei. The red lines indicate the approximate longitudinal location of particles with rapidity y = 0, y = 1, and y = 6. (Figure adapted from http://web.mit.edu/mithig/movies/LHCanmation.mov.)

Through measuring the final state particles in the detector it is possible to uncover the presence of the QGP and also measure its properties. While measuring the soft particle production leads to an understanding of the collective modes of the system behavior as a whole, studies of hard processes provide an insight into the transport characteristics of the medium and its initial stage. A particular case of such hard-scattering observable is the measurement of the vector boson production discussed in the next section.

2.2 Vector boson production

The W and Z bosons were discovered in 1983 by the UA1 and UA2 experiments at CERN [20–23]. Since then extensive studies have been performed at the LEP [24] and Tevatron [25] colliders. The EW boson measurements are an integral part of the scientific program at the LHC for all four experiments whether included in Standard Model (SM) precision measurements, beyond SM searches or as a part of the HI program.

The leading order (LO) of the W and Z boson production at the high-energy hadron collisions is the Drell-Yan mechanism of the quark-antiquark annihilation with leptons in the final state (both valence and sea quarks contribute to the process). The higher-order contribution includes $2 \rightarrow 2$ QCD processes (including also gluons in the initial state) with an additional quark or a gluon in the final state that will be observed as hadronic jets in the detector. Vector bosons predominantly decay through hadronic channels (70% of the time) but measurements in that decay channel suffer from large QCD background, especially in HI collisions where the outcoming jets interact with the QGP. Therefore, of particular experimental interest are the leptonic decay channels as they provide a much cleaner signal. The branching ratios are approximately 3.46% for the Z boson and 10.8% for the W boson in each of the leptonic decay channels.

As mentioned above, W and Z bosons are produced in the hard scattering that occurs at the initial stage of a HI collision. Due to a large Q^2 which corresponds to $M^2_{Z/W}$, no medium effect is expected to interfere in their production. Since their decay takes place at a short time scale of ∼0.01 fm/c, EW boson interference via QED effects with the medium is considered to be negligible. Besides, decay leptons that could in principle traverse the medium before and after thermalization are not expected to interact with the QGP, except for some residual QED interaction with charges in the QGP. This type of process has been shown to affect dilepton angular correlations in measurements of photon-induced dimuon pairs [26]. In this study, such effects are neglected and overall no medium effect is expected to contribute to the Z boson production and decay processes. This allows us to uniquely relate measured Z boson kinematic distributions to initial-stage effects that primarily modify momentum distributions of incoming partons involved in the hard scattering.

2.3 Parton distribution functions

In hadronic collisions, the kinematics of a hard scattering depends on the fraction of the nucleon momentum carried by the two incoming partons. The probability density of the longitudinal momentum distribution for partons is described by parton distribution functions (PDFs), denoted in the following as $f_i(x, \mu)$, where x is the momentum fraction of the parton i and μ is the factorization scale. The QCD factorization theorem suggests that at a high momentum transfer Q^2, the PDFs are universal and process independent which makes them an essential ingredient in cross section calculations of countless processes measured at the LHC. This emphasizes the relevance of obtaining these distributions for the quark and the gluon sector in different regions of the phase space.

In the case of the Drell-Yan Z production cross section, one can write the factorization as:

$$\sigma_{pp\to l\bar{l}X} = \sum_{i,j=q,\bar{q},g} \int_{x1}^{1} dz_1 \int_{x2}^{1} dz_2 \times f_i(z_1,\mu) f_j(z_2,\mu) \hat{\sigma}_{ij\to l\bar{l}X}\Big(\frac{x_1}{z_1}, \frac{x_2}{z_2}, \frac{Q}{\mu}\Big) + \mathcal{O}\Big(\frac{\Lambda^2_{QCD}}{Q^2}\Big), \quad (1)$$

where $f_{i,j}(z_{1,2},\mu)$ are the PDFs of the incoming partons and the $\hat{\sigma}$ is the matrix element on the parton level calculable in pQCD. PDFs obey the Dokshitzer-Gribov-Lipatov-Altarelli-Parisi (known as DGLAP) equations:

$$Q^2 \frac{\partial f_i}{\partial Q^2} = \sum_j P_{ij} \otimes f_j, \quad (2)$$

where P_{ij} are the splitting functions governing the scale evolution. Unlike the Q^2 evolution, a direct functional form of the x-dependence of the PDFs is not known from the first principles of QCD (even though there have been many recent developments based on lattice QCD approaches; for a comprehensive overview see for example Ref. [27]). Instead, a general approach is to determine the initial conditions for DGLAP equations by fitting experimental data by a process of a *global QCD analysis* where PDFs are essentially obtained by fits to a large span of data in the (x, Q^2) space. The experimental data included in the most recently published PDF sets comprises DIS HERA data from H1 and ZEUS experiments (for the full list of publications see [28, 29]), fixed target Drell-Yan results from NMC [30, 31], BCDMS [32, 33], SLAC [34], CHORUS [35], NuTeV [36] and finally the collider data from Tevatron (D0 [37] and CDF [38, 39]) and a plethora of data from the LHC experiments (ATLAS, CMS and LHCb). An example of the data set included in the global fit is shown in the left panel of Figure 3 as a function of x and Q^2 for the recent NNPDF3.0 PDF set [40].

In the context of HI collisions, one needs to derive PDFs for nucleons bound in incoming nuclei which can differ from the ones for nucleons in a vacuum. Formally, for a nucleus A with Z protons and N neutrons, one can write the nuclear PDF as:

$$f_i^A(x,Q^2) = \frac{Z}{A} f_i^{p/A}(x,Q^2) + \frac{N}{A} f_i^{n/A}(x,Q^2), \quad (3)$$

where $f_i^{p/A}$ is the bound proton PDF and the neutron PDF $f_i^{n/A}$ is obtained by employing the isospin symmetry. In the nPDF calculation approach one usually also assumes that the bound proton PDFs have the same evolution equations and sum rules as the free proton PDFs.

In the DIS measurements quoted above, it was shown that the bound proton PDF gets modified compared to the free proton case (a comprehensive review can be found in

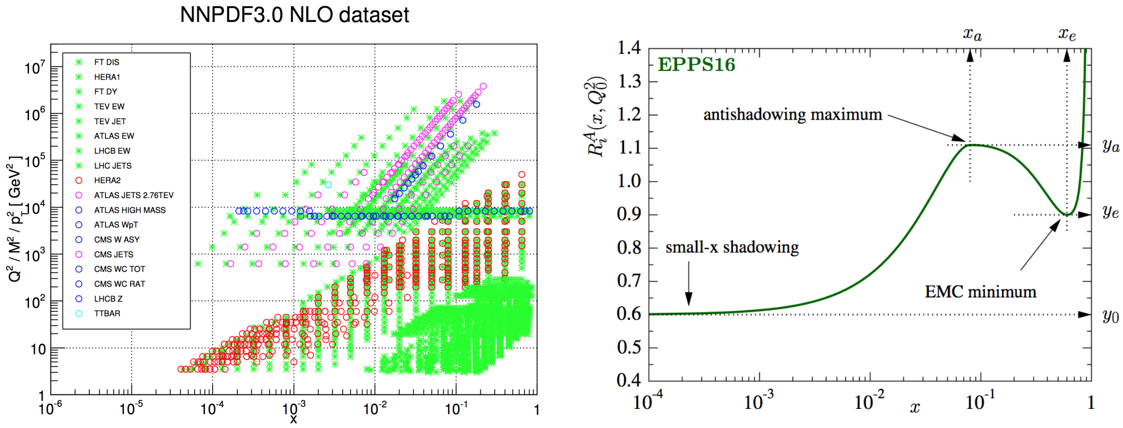

Figure 3: (*Left*) The kinematical coverage in the (x, Q^2) plane of the data included in the NNPDF3.0 PDF fit [40]. (*Right*) Illustration of the PDF modification in the nucleus R_i^A in different regions of the longitudinal momentum fraction x [41].

Ref. [42]). The ratio of the bound to the free proton PDF is usually quantified by the nuclear modification factor:

$$R_i^A(x, Q^2) = \frac{f_i^{p/A}(x, Q^2)}{f_i^p(x, Q^2)}. \tag{4}$$

Figure 3 in the right panel shows the fit function $R_i^A(x, Q^2)$ for the nuclear modifications in the most recent EPPS16 nPDF set [41]. A significant reduction in the ratio in the region $x < 0.1$ is called shadowing, while the region from $0.3 < x < 0.6$ is generally referred to as the EMC effect. The rise of the ratio above unity for x around 0.1-0.2 represents a transition region in the data and in the models and is know as the anti-shadowing region. As x approaches 1, the ratio steeply rises due to nuclear effects such as the intrinsic motion of the nucleons in a nucleus at rest (Fermi motion). Different kinematic regions of the phase space are mapped with the variety of the available data and are included in the latest nPDF fits used in this work for comparisons to the measured data.

2.4 Glauber model of HI collisions

In this section, we derive a theoretical framework for describing HI collisions in the context of many-body scattering theory. A major contribution in this field is usually attributed to R. J. Glauber and his pioneering work in the 1950s [43, 44]. The theory was successful in describing the total cross section in $d + \bar{p}$ collisions [45] and proton–nucleus collisions [46] where in the latter it was able to reproduce distinct features of the measured differential elastic cross section [47]. Hence, many of the models used to calculate geometric quantities in the initial state of HI collisions are still called "Glauber" models, even though significant developments have been done by others [48, 49]. A brief overview of the model is given below.

Figure 4 illustrates a collision of two nuclei in a side view where they are moving along the beam axis z with their centers displaced by $|\boldsymbol{b}|$. One usually wants to derive a probability of inelastically colliding two nucleons from each nucleus. It has to be noted that these calculations are done in the eikonal approach, which assumes that nucleons travel on straight trajectories and that the inelastic cross section does not change in subsequent binary interactions.

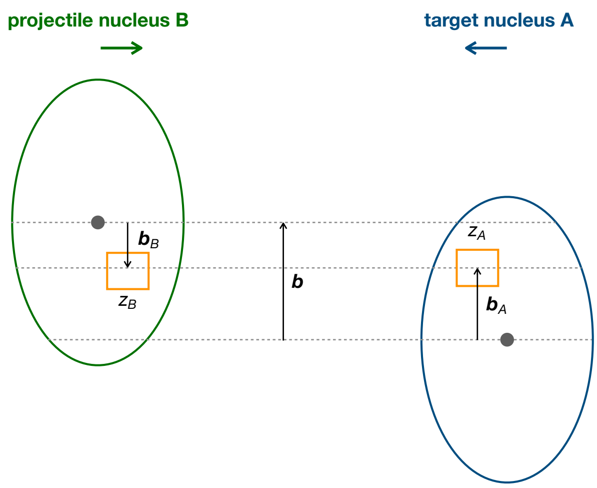

Figure 4: Schematic illustration of the Glauber model description of a HI collision transversal to the beam direction.

Essential ingredients to this model are the inelastic nucleon–nucleon (nn) cross section σ_{in}^{nn} (extracted from proton–proton measurements) and the probability of finding a nucleon in the nucleus in a volume of $2\pi b\, db\, dz$ that is given with the nucleon number density ρ. One can introduce the probability for a nn inelastic collision in a HI collision as $t(\mathbf{r})\sigma_{in}^{nn}$ where r is the nn impact parameter and the $t(\mathbf{r})$ is called the nn thickness function, an equivalent of a partonic luminosity. The nn impact parameter is given by $\mathbf{r} = \boldsymbol{b} - \boldsymbol{b}_A - \boldsymbol{b}_B$. If a probability of finding a nucleon in a nucleus is given by $\rho_i(\boldsymbol{b}_i, z_i)d\boldsymbol{b}_i dz_i$ where $(i =$

A, B), then the probability element of an nn inelastic collision is given by:

$$dP = \rho_A(\boldsymbol{b}_A, z_A)d\boldsymbol{b}_A dz_A \; \rho_B(\boldsymbol{b}_B, z_B)d\boldsymbol{b}_B dz_B \; t(\mathbf{r})\sigma_{in}^{nn} \quad (5)$$

$$= T_A(\boldsymbol{b}_A)d\boldsymbol{b}_A \; T_B(\boldsymbol{b}_B)d\boldsymbol{b}_B \; t(\mathbf{r})\sigma_{in}^{nn}, \quad (6)$$

where normalized thickness functions was introduced, $T_i(\boldsymbol{b}_i) = \int \rho_i(\boldsymbol{b}_i, z_i)dz_i$ for $i = A, B$. From this one derives the total probability for the nn inelastic collision as:

$$T_{AB}(\boldsymbol{b})\sigma_{in}^{nn} = \int T_A(\boldsymbol{b}_A)d\boldsymbol{b}_A \; T_B(\boldsymbol{b}_B)d\boldsymbol{b}_B \; t(\boldsymbol{b} - \boldsymbol{b}_A - \boldsymbol{b}_B)\sigma_{in}^{nn}, \quad (7)$$

where T_{AB} is the total thickness function. To calculate the total inelastic cross section for $A + B$ collision σ_{in}^{AB}, one needs to add all the possible number of collisions between the nucleons in crossing, ranging from 1 to AB. The probability for k inelastic events to occur when nuclei are $\boldsymbol{b}$ apart is:

$$P(k, \boldsymbol{b}) = \binom{AB}{k} [T(b)\sigma_{in}^{nn}]^k \, [T(b)\sigma_{in}^{nn}]^{AB-k}, \quad (8)$$

where for simplicity one usually considers spherically symmetric nuclei ($T(\boldsymbol{b}) = T(b)$); finally the total cross section yields:

$$\sigma_{in}^{AB} = \int \sum_{k=1}^{AB} P(k, \boldsymbol{b})d\boldsymbol{b}$$

$$= \int 1 - [1 - T(b)\sigma_{in}^{nn}]^{AB} d\boldsymbol{b}. \quad (9)$$

One can show that the average number of nucleon-nucleon collisions at $\boldsymbol{b}$ is given by [11]:

$$\langle N_{\text{coll}}(b)\rangle = \sum_{k=1}^{AB} kP(k, b) = ABT_{AB}(b)\sigma_{in}^{nn}, \quad (10)$$

and the number of nn collisions per inelastic nucleus-nucleus collision after integrating over the impact parameter is

$$\langle N'_{\text{coll}}\rangle = AB\sigma_{in}^{nn}/\sigma_{in}^{AB}. \quad (11)$$

2.4.1 Glauber Monte Carlo calculations

Practically, the modeling of HI collisions relies on Monte Carlo (MC) methods that implement the Glauber model approach in computer calculations. Firstly, the nucleons are distributed in the transverse plane according to the nuclear charge density distribution. For spherical nuclei such as ^{208}Pb, the density is a function only of the nuclear radius and is modeled by a Fermi distribution:

$$\rho(r) = \rho_0 \frac{1 + w(r/R)^2}{1 + exp(\frac{r-R}{a})}, \quad (12)$$

where ρ_0 is the nucleon density, R is the nuclear radius, a is the skin depth and w models deviations from the Fermi distribution. These constants are extracted from low-energy scattering experiments [50] and for ^{208}Pb one usually has $R = 6.624$ fm, $a = 0.549$ fm and $w = 0$ (overall normalization does not enter the calculation) [51].

The collision itself is simulated by randomly choosing the value of the impact parameter from a distribution $dN/db \propto b$ (up to $2R$) and then registering inelastic nucleon–nucleon collisions if their radial distance does not exceed $\sqrt{\sigma_{in}^{nn}/\pi}$. The generator therefore provides the number of nn collisions per event, $N_{\rm coll}$ and the number of total participating nucleons in the collision, $N_{\rm part}$.

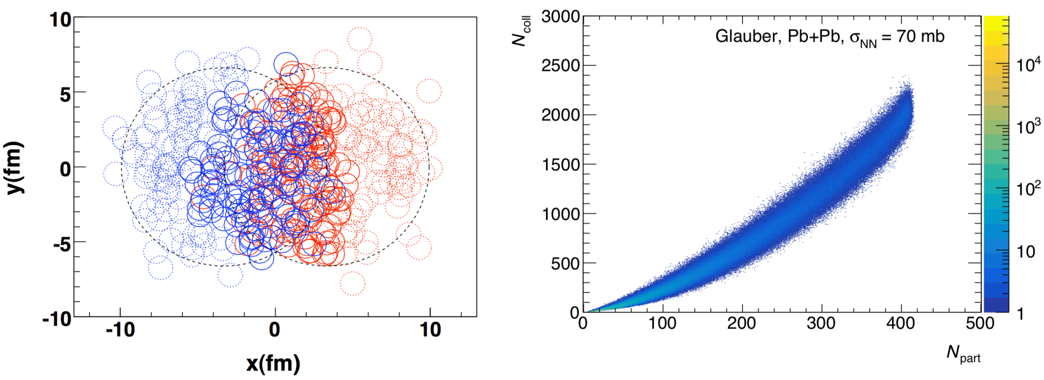

Figure 5: (*Left*) One simulated Pb+Pb collision in the transverse plane. Nucleons that interacted inelastically are indicated as solid circles, while others are dotted circles [51]. (*Right*) Distribution of the number of binary nucleon-nucleon collisions ($N_{\rm coll}$) versus the number of participating nucleons ($N_{\rm part}$) for a simulated Glauber MC sample used in this work [52]. Low values of $N_{\rm coll}$ and $N_{\rm part}$ correspond to events simulated with large impact parameter values or to more peripheral events. The colored z-axis shows the number of events in each bin of $N_{\rm coll}$ and $N_{\rm part}$.

The example of a simulation is given in Figure 5 where in the left panel one sees the nucleon distribution in the transverse plane for one Pb+Pb collision and in the right panel the distribution of N_{coll} versus N_{part} for a large simulated sample of events. The derived geometrical quantities are further related to the experimental data by a mapping procedure that involves a full detector simulation and is described in detail in Section 3.2.

3 Experimental methods

In this chapter, we introduce the main ingredients necessary for measuring the Z production cross section in the data collected with the ATLAS detector. The detector is described in Section 3.1 with the emphasis on relevant subsystems used for extracting Z boson yields from measuring decay leptons. In Section 3.2 we describe the procedure of centrality determination in the experimental data within the Glauber model framework. The concept of the nuclear modification factor as an experimental observable used for HI measurements is introduced in Section 3.3.

3.1 ATLAS experiment at the LHC

The ATLAS experiment [53] is a multi-purpose particle detector with a forward-backward symmetric cylindrical geometry and nearly 4π coverage in solid angle. The collision point is surrounded by inner tracking devices followed by a superconducting solenoid providing a 2 T magnetic field, a calorimeter system, and a muon spectrometer. Below we discuss the main detector subsystems and their properties used for the measurements discussed in this work.

Inner detector. The inner-detector (ID) system is immersed in the magnetic field and provides charged-particle tracking in the range $|\eta| < 2.5$. On average, a central HI collision can record about 4500 charged particles in midrapidity, which forms a substantial challenge for the detector performance. To satisfy the physics requirements of physics analyses for the vertex and momentum resolution, the tracking system is designed as a multi-layer silicon detector. This enables the hit reconstruction through robust pattern recognition and high precision in both R-ϕ and z coordinates.

The first hit is usually detected in the insertable B-layer [54–56] and followed by three more layers of the silicon pixel detector and four double layers of silicon microstrip trackers (SCT). These silicon detectors are complemented by the transition-radiation tracker (TRT), which enables radially extended track reconstruction up to $|\eta| = 2.0$. In HI collisions the TRT is not used in the track reconstruction due to occupancy saturation. The ATLAS ID system cross-section summary is shown in Figure 6.

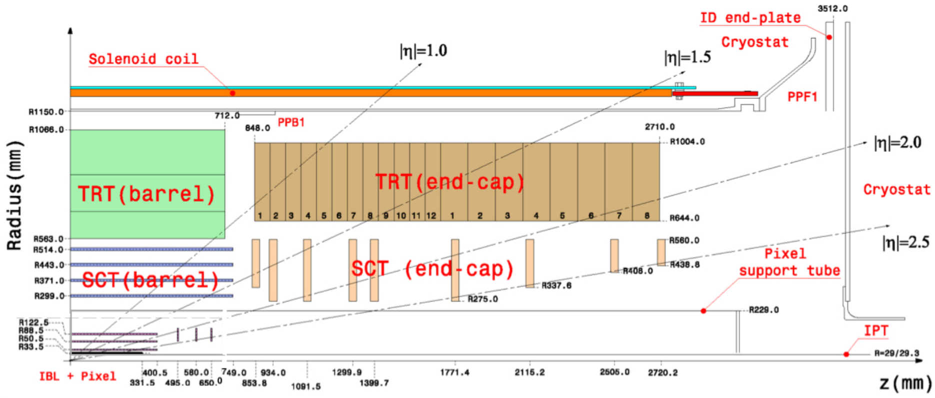

Figure 6: The layout of the ATLAS inner tracking detector: IBL, Pixel, SCT and TRT detector layers. (Figure adapted from Ref. [56].)

The primary vertex resolution improves with detector occupancy and so in *pp* events it ranges from 30 μm for events with 70 tracks to about 80 μm for events with 20 tracks, while in HI events it about 10 μm. The momentum resolution depends linearly on the track momentum both in *pp* and Pb+Pb systems and it grows in the forward η region. Typically, for $|\eta| < 1.9$ it ranges from 3% up to 10 GeV and rises to approximately 10% at 100 GeV. For more forward tracks, the momentum resolution rises from 8% to 15% in the same momentum range.

Calorimeters. The two main components of the ATLAS calorimetry system are the Liquid Argon (LAr) Calorimeter and the Tile Hadronic Calorimeter (TileCal). They cover a wide range of $|\eta| < 4.9$ and are designed to stop and measure the energy loss of electrons, photons and charged hadrons (jets). The total thickness of the EM calorimeter is > 22 radiation lengths (X_0) in the barrel and > 24 (X_0) in the end-caps. The approximate 9.7 interaction lengths (λ) of active calorimeter in the barrel (10λ in the end-caps) are adequate to provide a good resolution for high energy jets. The cross-section view of the ATLAS calorimeter system is shown in the left panel of Figure 7 with all the subsystems.

LAr calorimeters are divided into EM barrel ($|\eta| < 1.475$) and endcap ($1.375 < |\eta| < 3.2$), LAr hadronic end-cap calorimeter ($1.5 < |\eta| < 3.2$) and LAr forward calorimeter

(3.1 < $|\eta|$ < 4.9). They are placed inside of three aluminum cryostats and supplied by liquid Argon at -183 °C. The operation technology is based on the noble-liquid sampling calorimetry where alternating layers of absorbers (lead or copper) and active gas components with high-voltage kapton electrodes are used to degrade the energy of an incident particle and measure the ionization signal coming from the EM or hadronic shower. Electrodes are arranged in the accordion geometry that provides complete ϕ symmetry without azimuthal cracks. The energy resolution for the EM barrel and endcap is about $10\%/\sqrt{E}$. Schematic representation of the EM calorimeter basic structure is shown in the right panel of Figure 7. The barrel calorimeter consists of two identical half-barrels, separated by a small gap (4 mm) at $z = 0$. Each end-cap calorimeter is mechanically divided into two coaxial wheels: an outer wheel covering the region $1.375 < |\eta| < 2.5$, and an inner wheel covering the region $2.5 < |\eta| < 3.2$.

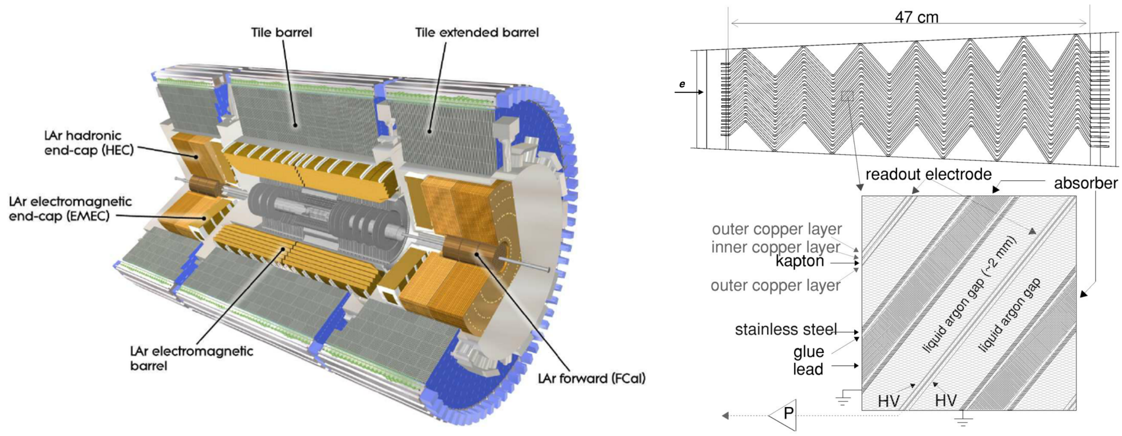

Figure 7: (*Left*) Side-view of the ATLAS calorimeter system [53]. (*Right*) Schematic view of the structure of the ATLAS EM calorimeter [57].

The forward calorimeters (FCals) are located in the same cryostat as the end-cap calorimeter and they consist of three modules in each end-cap: the first, made of copper, is optimized for electromagnetic measurements, while the other two, made of tungsten, measure predominantly the energy of hadronic interactions. Due to a very high incoming particle flux, the design of the FCal modules is based on the electrode structure of small-diameter rods, centered in tubes that are oriented parallel to the beam direction. The LAr gaps which are the sensitive element are smaller than 2mm. The energy resolution of FCal is about $100\%/\sqrt{E}$.

LAr hadronic end-cap calorimeter (HEC) provides hadronic coverage and provides an energy resolution of about $60\%/\sqrt{E}$. It has parallel copper plate absorbers orthogonal to the beam axis assembled into two consecutive wheels. The forward calorimeter (FCal) consists of three modules in each end-cap: the first, made of copper, is optimized for electromagnetic measurements, while the other two, made of tungsten, measure predominantly the energy of hadronic interactions. The energy resolution of the EM layer is about $30\%/\sqrt{E}$ and of the hadronic modules around $80\%/\sqrt{E}$ [58].

TileCal is a sampling calorimeter using iron as absorber material and scintillating tiles as an active material. It is placed directly outside the EM calorimeter. Both sides of the tiles are read by wavelength shifting fibers into two separate photomultipliers. The calorimeter is split into a barrel and two extended barrel parts. It provides an energy resolution of approximately $40\%/\sqrt{E}$ for pions.

In addition to the calorimeters described above, the ATLAS system also uses Zero-Degree Calorimeters (ZDCs) for detecting forward neutrons with $|\eta| > 8.3$ in HI collisions. The ZDCs are divided into two arms and reside inside the TAN (Target Absorber Neutral) absorber ± 140 m from the interaction point. Their design is based on scintillating sampling calorimeter technology using quartz rods as an active material readout by photomultipliers and tungsten and steal as absorption material. The single neutron energy resolution for the spectator neutron energy of 2.51 TeV is about 17%. By requiring a tight coincidence from the two arms of the ZDC's, background processes from beam-gas and beam-halo effects can be significantly reduced. The ZDC coincidence is also a basis of the minimum-bias (MB) trigger algorithm in HI collisions. Such triggers are designed to collect a large fraction of the total inelastic Pb+Pb cross section while introducing as little selection bias as possible. By requiring a single-sided ZDC signal or no signal in the ZDCs (below the energy of a single neutron), one can tag photon-nuclear and ultra-peripheral EM processes that leave one or both of the incident nuclei intact.

Muon Spectrometer. The Muon Spectrometer (MS) was designed to detect muons in the pseudorapidity region up to $|\eta| = 2.7$ and to provide better momentum resolution measurement in the central part of the detector after combining the information with the ID. The measurement technology is based on the magnetic deflection of muon tracks in the large superconducting air-core toroid magnets, instrumented with separate trigger and high-precision tracking chambers. The layout of the MS is shown in Figure 8. The magnetic system consists of a barrel toroid magnet that covers the regions of $|\eta| < 1.4$

and two smaller endcap toroids that deflect muons in the region $1.6 < |\eta| < 2.7$; the magnetic field in the transition region is provided by a combination of both barrel and endcap magnets. The bending power of the magnets, quantified as $\int Bdl$ where integral is evaluated between the first and the last chamber, is in the range from 1 to 7.5 Tm.

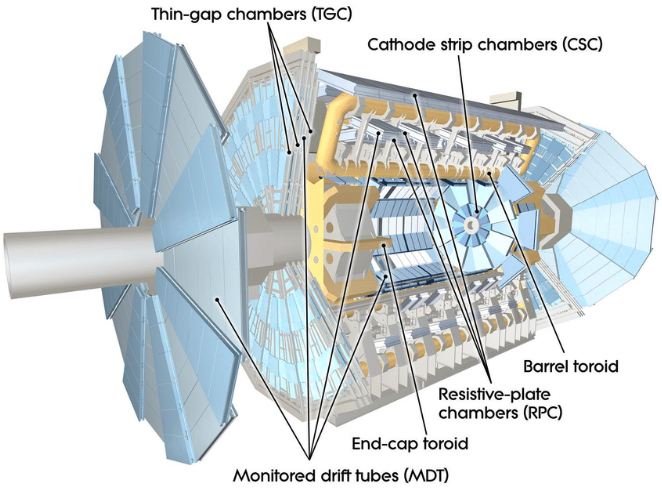

Figure 8: The layout of the ATLAS muon spectrometer with all types of muon chambers indicated [53].

Precision tracking of muons is done by Monitored Drift Tubes (MDTs) in the coverage of $|\eta| < 2.7$. A basic measuring element is a gas-filled tube, 1-6m long, with an anode that is at +3300 V so that it creates an avalanche of ionization electrons created by an incident muon. The gas mixture used is Ar-CO_2 (93-7%) at 3 bar, where Ar ensures a large primary ionization yield and CO_2 is a quencher gas that absorbs the UV photons from excited Ar atoms. The tubes are assembled into multilayers inside chambers that finally provide 50μm position resolution (single drift tube resolution is about 80 μm). Muon momentum resolution measured with MDTs is from 2–4% for muons from 10–200 GeV and rises to 12% for 1 TeV muons.

In the region $|\eta| > 2$ the counting rate exceeds the MDT requirements for safe operation (above 150 Hz/cm^2). Therefore, MDTs are replaced with cathode-strip chambers (CSC) which are multiwire proportional chambers with the wires oriented in the radial direction and segmented into strips to provide the position measurements. The position resolution of the CSC plane is 60 μm with a good two-track resolution. CSC can be operated safely up to 1 kHz/cm^2 rate.

An additional detector subsystem is installed inside the MS for triggering purposes.

In the barrel ($|\eta| \leq 1.05$), Resistive Plate Chambers (RPCs) are used which are gaseous parallel electrode-plate detectors. They have good spatial (~1 mm) and time resolution (about 2 ns) as well as adequate rate capability. In the end-cap region, Thin Gap Chambers (TGCs) have been selected which operate on the same principle as multi-wire proportional chambers, and they provide good time resolution (~4 ns) and high rate capability.

ATLAS Trigger. A two-level trigger system is used to select events for this analysis. The first-level trigger is implemented in hardware and uses a subset of the detector information. High-p_{T} muons are identified using RPC and TGC signals as described above. Calorimeter selections are based on reduced-granularity information from all the calorimeters. Results from the L1 muon and calorimeter triggers are processed by the central trigger processor, which implements a trigger "menu" made up of combinations of trigger selections. There is a possibility of implementing additional "event prescales" which further reduce the recorded output rate for each trigger in the menu. For the Z boson analysis one usually relies on the trigger with the lowest p_{T} requirement, defined by the allocated bandwidth, with no prescale reduction in both channels to maximize the measured boson yield. The L1 trigger sequence is followed by the software-based High-Level Trigger (HLT) system, which can run offline reconstruction and calibration software, further reducing the event rate. An example of this is quality requirements applied to the EM shower associated with electron and photon HLT objects.

In the 2015 *pp* reference run, the L1 rate for the main electron trigger (requiring $p_{\mathrm{T}} > 13$ GeV) was about 1 kHz and for the muon trigger about 2 kHz (for $p_{\mathrm{T}} > 10$ GeV muons). The HLT output rate for electrons and muons was around 20 Hz. During the Pb+Pb 2015 run the main electron L1 physics trigger ($p_{\mathrm{T}} > 12$ GeV) sampled the rate of about 1 kHz and the muon L1 trigger up to 200 Hz ($p_{\mathrm{T}} > 6$ GeV). The HLT rates went up to 200 Hz for the muon trigger (with $p_{\mathrm{T}} > 8$ GeV) and up to 40 Hz for the electron trigger (requiring $p_{\mathrm{T}} > 15$ GeV and additional quality cuts).

3.2 Centrality association in data

To estimate geometrical quantities within the Glauber model that can be associated with the experimental data, one usually applies a procedure called "mapping". It consists of finding the observable sensitive to the event activity in a HI collision that can be simultaneously employed in a Glauber MC simulation and also measured in the data. Then one can "map" geometric parameter distributions – such as N_{part}, N_{coll}, and T_{AA}– from simulation to data. Within the ATLAS framework, this observable is the total transverse energy measured in the forward calorimeters ($\Sigma E_{\text{T}}^{\text{FCal}}$) which cover the acceptance of $3.1 < |\eta| < 4.9$. The advantage of this particular calorimeter is that it is located at high rapidity and away from the main energy production region in the transverse direction. This reduces the bias that would have been otherwise introduced by an energy deposition of a hard scattering in the event.

The $\Sigma E_{\text{T}}^{\text{FCal}}$ distribution in data that is used for mapping is obtained from a minimum-bias (MB) event sample in the 2015 Pb+Pb collision data [52]. This sample of events is recorded by requiring two triggers: "L1TE50" is designed to register events with $E_{\text{T}} > 50$ GeV in the calorimeters, and "L1ZDC_A_C_VTE50" is designed to register peripheral inelastic events by requiring the ZDC coincidence signal and $E_{\text{T}} < 50$ GeV in the calorimeters. The collected sample contains inelastic collision events by introducing minimal selection biases. However, only a fraction of this distribution above $\Sigma E_{\text{T}}^{\text{FCal}} = 40$ GeV is used for the centrality association; below that value, a significant fraction of diffractive and photonuclear events compared to Glauber-like events is found to contaminate the sample. The left panel of Figure 9 shows the $\Sigma E_{\text{T}}^{\text{FCal}}$ distribution sampled by the two MB triggers, where the negative and positive tails show contributions from multiple inelastic events recorded together (*pile-up*).

An equivalent distribution is then obtained in the full Glauber MC sample where one can relate geometric parameters to $\Sigma E_{\text{T}}^{\text{FCal}}$ via the *two-component-model* [59]. This model assumes that the soft particle production rate, or the particle production with the low momentum transfer, depends on the "soft" contribution proportional to N_{part} and the "hard" contribution that scales with N_{coll} (or T_{AA}). One derives the linear weight of these two contributions from *pp* events and obtains that $P(\Sigma E_{\text{T}}^{\text{FCal}}; N_{\text{part}} = 2, N_{\text{coll}} = 1) = Gaus(\Sigma E_{\text{T}}^{\text{FCal}})$ which is then used for convolution into the final $\Sigma E_{\text{T}}^{\text{FCal}}$ distribution in Pb+Pb events. When fitted to the data, the fraction of Glauber-like events or the fit efficiency is at the level of 85%, as it can be seen in the right panel of Figure 9. By dividing then the MB distribution in the data into 85 bins of equal sizes, one obtains the $\Sigma E_{\text{T}}^{\text{FCal}}$ cuts that determine the centrality intervals. Finally, $\langle N_{\text{part}} \rangle$ and $\langle N_{\text{coll}} \rangle$ in

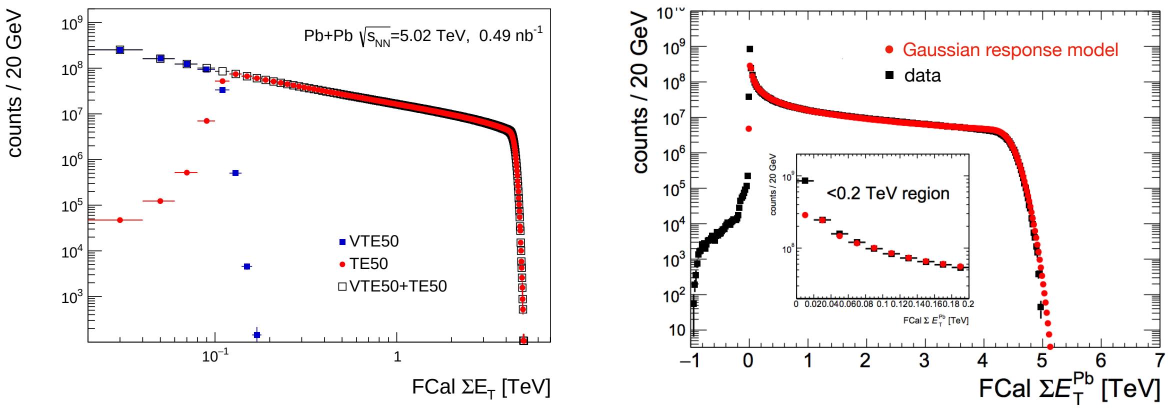

Figure 9: (*Left*) $\Sigma E_{\mathrm{T}}^{\mathrm{FCal}}$ distributions in the 2015 Pb+Pb data collected with two MB triggers "VTE50" (blue squares) and "TE50" (red circles). A sum of the two distributions used in the GMC mapping procedure is given in open squares. (*Right*) Fit result showing a Glauber + Gaussian fit (red circles) to the MB data (black squares) in the region $\Sigma E_{\mathrm{T}}^{\mathrm{FCal}} > 40$ GeV. (Figure adapted from Ref. [52].)

centrality intervals are derived from ($\Sigma E_{\mathrm{T}}^{\mathrm{FCal}}$, N_{part}) and ($\Sigma E_{\mathrm{T}}^{\mathrm{FCal}}$, N_{coll}) distributions derived from the fits and the T_{AA} is obtained as a ratio of $\langle N_{\mathrm{coll}} \rangle$ to σ_{in}^{nn}.

Centrality	$\langle N_{\mathrm{part}} \rangle$	$\langle T_{\mathrm{AA}} \rangle$ [mb^{-1}]	Centrality	$\langle N_{\mathrm{part}} \rangle$	$\langle T_{\mathrm{AA}} \rangle$ [mb^{-1}]
0–2%	399.0 ± 1.6	28.30 ± 0.25	20–25%	205.6 ± 2.9	9.77 ± 0.18
2–4%	380.2 ± 2.0	25.47 ± 0.21	25–30%	172.8 ± 2.8	7.50 ± 0.17
4–6%	358.9 ± 2.4	23.07 ± 0.21	30–40%	131.4 ± 2.6	4.95 ± 0.15
6–8%	338.1 ± 2.7	20.93 ± 0.20	40–50%	87.0 ± 2.4	2.63 ± 0.11
8–10%	317.8 ± 2.9	18.99 ± 0.19	50–60%	53.9 ± 2.0	1.28 ± 0.07
10–15%	285.2 ± 2.9	16.08 ± 0.18	60–80%	23.0 ± 1.3	0.39 ± 0.03
15–20%	242.9 ± 2.9	12.59 ± 0.17	80–100%	4.80 ± 0.36	0.052 ± 0.006
			0–100%	114.0 ± 1.1	5.61 ± 0.06

Table 1: Centrality intervals and their corresponding geometric quantities with systematic uncertainties, from Ref. [60].

Table 1 summarizes geometric quantities, $\langle N_{\mathrm{part}} \rangle$ and $\langle T_{\mathrm{AA}} \rangle$, corresponding to centrality intervals as calculated with Glauber MC v2.4 [60]. A special treatment is employed for the 20% most peripheral interval of events, where diffractive and photonuclear processes significantly contribute to the MB event sample. This requires extrapolating the total number of MB events in this region and employing a special requirement on the Z boson event topology and so ensuring no background contamination. The total number of minimum-bias events in 0–80% centrality interval is $(2.99 \pm 0.05) \times 10^9$ which is then distributed in different centrality intervals according to their size.

3.3 Nuclear modification factor

In this section, we introduce the main observable constructed by taking the ratio of the Z boson production yields in pp and Pb+Pb systems. Due to its normalization, this observable reflects the presence of nuclear effects in the Pb+Pb system not taken into account in the Glauber model.

In Pb+Pb collisions, a Z boson can be produced in a hard interaction of any two nucleons from the colliding nuclei. Since the production of a Z requires large momentum exchange and has a low cross section, one can neglect any other "soft" interaction into which the same nucleons can also be involved. Therefore:

$$\sigma^Z_{\mathrm{AA}} \approx A^2 \sigma^Z_{pp}, \tag{13}$$

where the number of nucleons in the ion A is the sum of the number of protons (the nucleon charge Z) and neutrons. Taking into account the isospin effects:

$$\begin{aligned} \sigma^Z_{\mathrm{AA}} &= Z^2 \sigma^Z_{pp} + (A-Z)^2 \sigma^Z_{nn} + 2Z(A-Z)\sigma^Z_{pn} \\ &= A^2 \sigma^Z_{pp} \Big(\frac{Z^2}{A^2} + \frac{Z(A-Z)^2}{A^2} \frac{\sigma^Z_{pn}}{\sigma^Z_{pp}} + 2 \frac{(A-Z)}{A} \frac{\sigma^Z_{nn}}{\sigma^Z_{pp}} \Big) \\ &= c_{\mathrm{iso}} A^2 \sigma^Z_{pp}, \end{aligned} \tag{14}$$

where σ^Z_{pp}, σ^Z_{pn} and σ^Z_{nn} denote the corresponding nucleon-nucleon cross sections and c_{iso} accounts for the isospin effects. Since for the Z boson the cross sections $\sigma^Z_{pp} \approx \sigma^Z_{pn} \approx \sigma^Z_{nn}$, the coefficient c_{iso} is close to 1 and independent of b_{imp}. From the simulation one obtains $c_{\mathrm{iso}} = 1.02$.

The total number of Z bosons in the sample can be found from Eq. 14,

$$N^Z_{\mathrm{AA}} = c_{\mathrm{iso}} A^2 \sigma^Z_{pp} \mathcal{L} \approx A^2 \sigma^Z_{pp} \mathcal{L}, \tag{15}$$

where $\mathcal{L}$ is the integrated luminosity of the collected data. This number can further be related to the total number of inelastic (non-singly diffractive) Pb+Pb collisions, N_{evt}, that corresponds to the inelastic Pb+Pb cross section $\sigma^{\text{inel}}_{\text{AA}}$. The luminosity $\mathcal{L}$ cancels out leading to:

$$\frac{N^Z_{AA}}{N_{\text{evt}}} = \frac{A^2}{\sigma^{\text{inel}}_{\text{NN}}}\sigma^Z_{pp} = T_{\text{AA}}\sigma^Z_{pp}, \tag{16}$$

which shows that the hard probe production rate must scale with the magnitude of the nuclear overlap which depends on b_{imp}. Therefore, in the Pb+Pb measurement of the Z production presented in this work, a main observable according to Equation 16 is the Z boson yield scaled by the number of MB inelastic collisions and the average nuclear thickness function $\langle T_{\text{AA}}\rangle$, later referred to as the *normalized yield*.

Equation 16 leads to the experimental observable that is widely used in HI studies and is called the Nuclear Modification Factor (R_{AA}). The R_{AA} is used to quantify nuclear effects on particle production and is defined as:

$$R_{\text{AA}} = \frac{1}{T_{\text{AA}}}\frac{1}{N_{\text{evt}}}\frac{d^2N^Z_{AA}/dydp_{\text{T}}}{d^2\sigma^Z_{pp}/dydp_{\text{T}}}. \tag{17}$$

Here, the R_{AA} is derived for the Z production but is equivalently defined for any hard probe observable. For colored processes, the R_{AA} is measured to be significantly less than unity for any color-sensitive probes: charged particles, jets, heavy flavor mesons. However, the yields of Z bosons measured in electron and muon decay channels are not affected by the medium. Therefore, up to the isospin effects (c_{iso} discussed above), the R_{AA} of Z boson should be unity. Other effects that can lead to the departure of the Z boson R_{AA} from unity are the cold nuclear matter (CNM) effects, such as the nPDF modification discussed in Section 2.3 and inaccurate measurement of the initial collision geometry discussed in Section 2.4. These considerations make the R_{AA} of a Z boson a very interesting object to study.

4 Overview of current results

Measurements of Z and W boson production in HI collisions became feasible only in the last 10 years after the turning on of the LHC machine. For the first time, it was possible to reach sufficiently high enough center-of-mass energy and the data luminosity for the yields to be abundant in spite of their low cross section and the low branching ratio in leptonic decay channels. Run-1 physics results (2010-2013) predominantly came from ATLAS [61–64] and CMS [65–68] collaborations with an addition of the Z observation from the LHCb experiment [69]. In Run-2 (2015-2018), together with new results reported by ATLAS [70, 71] and CMS [72], the first result also came from the ALICE collaboration [73]. Table 2 summarizes data delivered by the LHC relevant for these studies.

period	year	collision system	$\sqrt{s_{\rm NN}}$, $\sqrt{s}$ [TeV]	luminosity	Ref.
Run-1	2010, 2011	Pb+Pb	2.76	$147\,\mu$b^{-1}	[61, 62, 65, 66]
	2011, 2013	pp	2.76	$4.2\,$pb^{-1}	[66]
	2013	p+Pb	5.02	$28\,$nb^{-1}	[69, 63, 64, 67, 68]
Run-2	2015	Pb+Pb	5.02	$0.49\,$nb^{-1}	[73, 70, 71]
	2015	pp	5.02	$25\,$pb^{-1}	[74, 70, 71]
	2016	p+Pb	8.16	$165\,$nb^{-1}	[72]

Table 2: Summary of published EW boson results by the four LHC experiments from Run-1 and Run-2 data sets.

As explained in the Introduction, there are three main focal points in measuring the production rates of EW bosons in HI collisions which are: 1) PDF modification, 2) rates in centrality classes and 3) yields in peripheral events. In this chapter, we overview the present status of experimental measurements and their agreement with currently available model predictions. We start with nPDF model comparisons in Section 4.1 and move to the current results on the EW boson production as a function of centrality in Section 4.2. Finally, we introduce recent model corrections to Glauber model predictions in peripheral collisions in Section 4.3 and discuss the contribution from electromagnetic processes in ultra-peripheral Pb+Pb events in Section 4.4.

4.1 Nuclear parton distribution functions

As it was discussed in Section 2.3, possible nuclear modification of the free proton PDF can be addressed by measuring the fraction of longitudinal momentum x (or rapidity y) of the produced bosons. In the following, we review the recent data recorded by the LHC experiments used to constrain the nPDFs.

While Run-1 results from Pb+Pb measurements were unable to distinguish between free proton and modified PDF predictions, ATLAS results in the p+Pb system [63, 64] preferred a model with nPDF modification as seen in the left panel of Figure 10; the free

PDF predictions were not excluded, however. A strong confirmation of that indication came from the CMS Run-2 p+Pb result [72] where the experimental data clearly prefers the nuclear modification and excludes the free PDF prediction (with the best probability for the free PDF at the level of 10^{-8} [72], therefore below the exclusion limit). The CMS result on the W differential cross section is shown in the right panel of Figure 10.

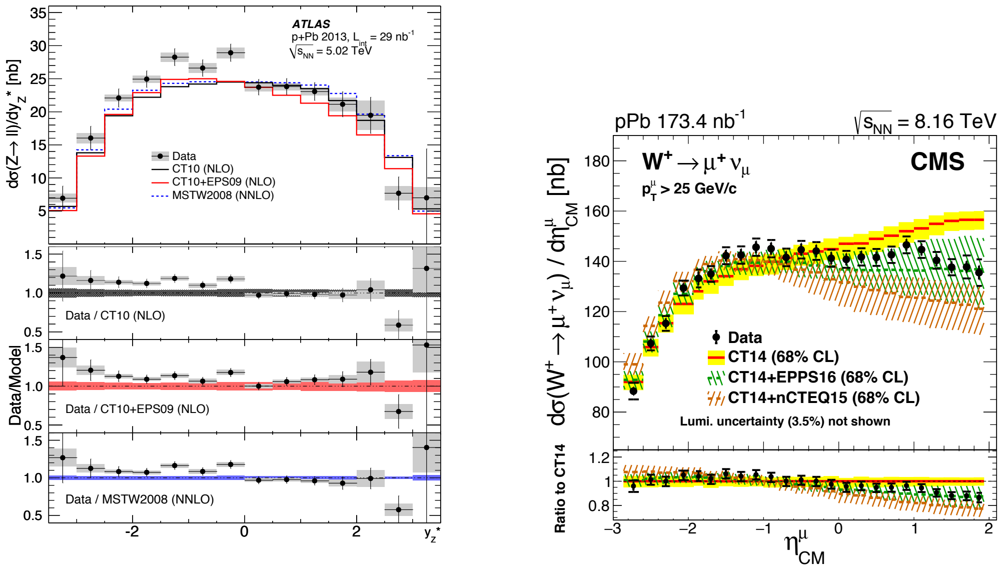

Figure 10: (*Left*) Differential cross section $d\sigma/dy^*_Z$ for $Z \to \ell\ell$ measured in the p+Pb system at $\sqrt{s_{\rm NN}} = 5.02$ TeV by ATLAS compared with several model calculations including free proton PDF and nPDFs [63]. (*Right*) The $d\sigma/d\eta^\mu$ distribution for $W^- \to \mu^+\nu_\mu$ measured in the p+Pb system at $\sqrt{s_{\rm NN}} = 8.16$ TeV by CMS compared with the most recent free PDF and nPDF sets [72].

New results from the Run-2 LHC data have recently been reported concerning PDF and nPDF predictions in the Pb+Pb system. The measurement by ALICE [73] reported better agreement with nPDF calculations for Z bosons in forward rapidity, $2.5 < y < 4.0$, while the free PDF prediction deviates from the measurement at the level of 2–3 standard deviations. In contrast with this, a most recent ATLAS measurement of W boson production in Pb+Pb [70] indicates a better agreement with free proton PDF predictions at midrapidity, $|\eta_\ell| < 2.5$, while the nPDF calculations tend to underestimate the yields measured in data. The left panel of Figure 11 shows ALICE results of Z boson yield normalized by $T_{\rm AA}$ measured in the muon decay channel in two bins of rapidity, where better agreement is observed with the EPPS16 nPDF as compared to CT14 proton PDF. In the right panel the differential yield of W^- bosons is shown as a function of lepton η measured by ATLAS where the trend is opposite to that from ALICE. These results point to different conclusions concerning the nPDF agreement with data. This advocates for more precise measurements in the Pb+Pb system.

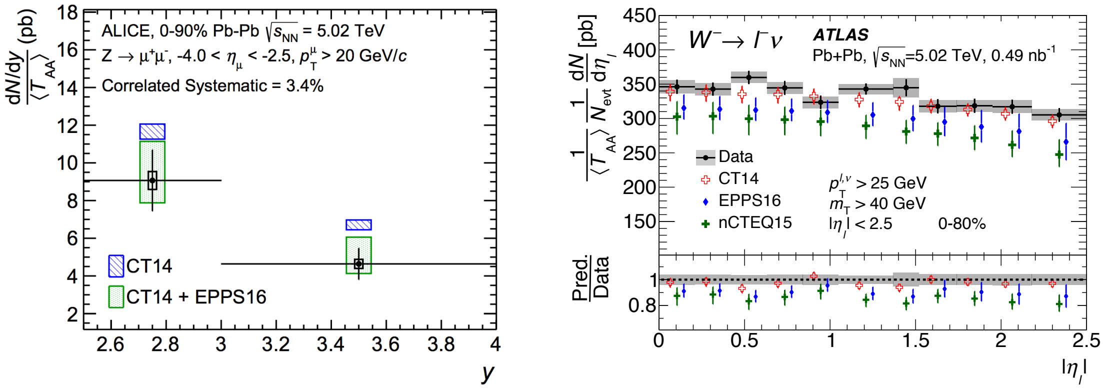

Figure 11: (*Left*) Normalized production yields of dimuon pairs from Z decays as a function of rapidity in $2.5 < y < 4.0$ for the 0–90% centrality interval measured in $\sqrt{s_{\mathrm{NN}}} = 5.02$ TeV Pb+Pb data by ALICE [73]. (*Right*) Normalized production yields of W^- as a function of absolute lepton pseudorapidity for combined electron and muon channels in the 0–80% centrality interval measured by ATLAS in $\sqrt{s_{\mathrm{NN}}} = 5.02$ TeV Pb+Pb collisions [70].

What this shows is that while in the asymmetric system data favors the nPDF scenario and can distinguish between different distribution functions with the current precision, more studies are required to reach the same conclusion in the larger nucleus-nucleus collision system.

4.2 Electroweak boson production rates

The data presented in the previous section is used to measure the production yields in different centrality classes of HI collisions. As discussed in Section 3.3, the expectation of the Glauber model is that Z and W production rates scale with the nuclear thickness function T_{AA} or the amount of the nuclear overlap in a collision. This statement includes our current understanding of a hard process within pQCD (factorization theorems) as well as our current understanding of multi-particle scattering and geometry in HI collisions. In terms of the nuclear modification factor, this predicts that R_{AA} should be constant across centrality intervals for both species. In previous studies, this expectation is confirmed within the available precision of the data.

To study this prediction, yields have been measured by ATLAS [61, 62] and CMS [65, 66] in Run-1 data as a function of centrality and have been shown to scale with the nuclear overlap or the number of binary collisions. Results from the two Run-1 ATLAS measurements are shown in Figure 12 and they demonstrate the scaling as predicted by models, with statistical precision of the data at the level of ∼3% for W result and ∼10% for the Z result per bin (including full data luminosity from 2010 and 2011 runs superior to CMS results).

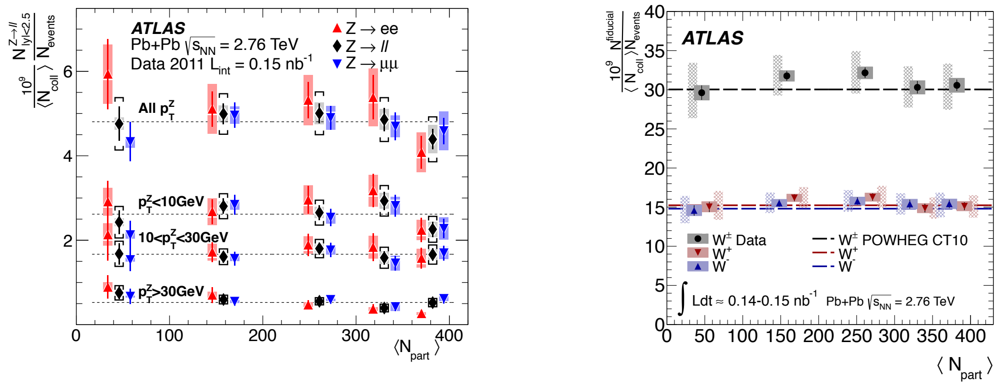

Figure 12: (*Left*) Normalized yield for Z bosons, in the dielectron, dimuon, and combined channels, from Run-1 ATLAS data for $\sqrt{s_{\rm NN}}$ = 2.76 TeV Pb+Pb collisions, as a function of the mean number of participants $\langle N_{\rm part}\rangle$, for different $p_{\rm T}$ slices [62]. (*Right*) Normalized W boson production yield as a function of $\langle N_{\rm part}\rangle$ for W^+, W^-, and $W^\pm$ bosons for combined muon and electron channels measured by ATLAS in the same data set [61].

Controversially, a number of measurements done in the p+Pb system have observed similar effects to the ones measured in the Pb+Pb system that have been traditionally attributed to QGP-medium interactions: results from long-range azimuthal correlations in p(d)+A system [75–78], enhancement of particles coming from heavy meson decays [79–81] and deviations from binary scaling in the high-$p_{\rm T}$ jet and hadron production [82–84], all point to further investigation of the current understanding of QGP signatures. One possible way of answering the questions arising from these effects is using the EW bosons to probe the initial state conditions of the system. From the CMS and ATLAS measurements of the W [67, 64] and Z [68, 63] boson yields it follows that certain adjustments and constraints on the PDF sets used in models have to be imposed, and it is still a matter of discussion which geometrical model should be applied to p+Pb collisions.

New Run-2 results on EW boson scaling in Pb+Pb system were reported by ALICE [73] for Z bosons and ATLAS [70] for W bosons. ALICE data suffers from large statistical uncertainties since the Z yield is measured in the forward region but the measurement is consistent with T_{AA} scaling for two reported centrality intervals. In that respect, the new ATLAS data provides insight on this subject with unprecedented precision. For the first time, one sees an indication of deviation from the predicted T_{AA} scaling in peripheral Pb+Pb collisions at the level of 1–2σ, as shown in Figure 13. Nevertheless,

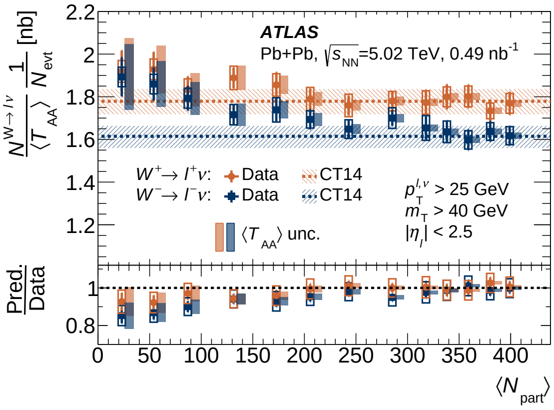

Figure 13: Normalized production yields of W^+ (orange circles) and W^- bosons (blue squares) as a function of $\langle N_{\mathrm{part}} \rangle$ shown for the combination of electron and muon decay channels and compared with CT14 NLO PDF calculations measured by ATLAS in the $\sqrt{s_{\mathrm{NN}}} = 5.02$ TeV Pb+Pb data [70]. The lower panel shows the ratio of the predictions to the measured yields in data.

the result shows that the T_{AA} scaling holds for mid-central and central collisions as anticipated. Together with this result, the Z boson measurement presented in Section 6.3 provides a significant contribution to the current understanding of HI collision geometry.

It should be noted that for the first time in Run-2, the reference pp data is available at the same partonic luminosity as in Pb+Pb to construct EW boson R_{AA} (that was previously estimated with calculations). This better captures possible PDF and nPDF effects since data-to-data ratio should to some degree cancel out possible deviations in valence u and d quark distributions (for free proton PDF) in data compared to simulations including various PDFs (as it is already known from the pp measurements that free PDFs exhibit deviations from the data at midrapidity, see for example [85]). The W and Z boson R_{AA} will be discussed in more detail in Chapter 6.

4.3 Corrections to the Glauber model in peripheral collisions

All the results presented above inherently depend on the centrality model and the mapping procedure employed by the experimental group. Recently, however, corrections to the Glauber model have been introduced in a model known as HG-PYTHIA which uses insights from the measured jet production in peripheral Pb+Pb collisions. Suppression of jets and charged particles in Pb+Pb collisions has been measured in Run-1 and Run-2 Pb+Pb data at the LHC and established as one of the primary signatures of final state medium effects [86–90, 84]. An interesting feature of these measurements is that the high-p_{T} jet and charged particle R_{AA} stays below unity for peripheral Pb+Pb collisions as is shown in the left panel of Figure 14, indicating that significant jet suppression is still present for a considerably small amount of nuclear overlap. The measurements at this point extend to 80% for ATLAS and to 90% centrality interval for CMS. As opposed to that, the data so far points to no suppression in the p+Pb system [91]. Even though the interpretation of the measured nuclear modification factor in p+Pb data ($R_{p\mathrm{Pb}}$) for jets and charged hadrons depends on the employed geometrical model and can contain strong nPDF effects, overall the data indicates no suppression comparable to the level measured in peripheral Pb+Pb collisions. Since a common expectation coming from the consideration of the system size implies a smooth transition between peripheral Pb+Pb and p+Pb collisions, these results introduce a tension in the current understanding of HI collision geometry and medium effects on colored probes.

An alternative explanation for the low measured charged-particle R_{AA} in peripheral Pb+Pb collisions was recently introduced by Loizides and Morsch [93] by exploring possible biases in geometry estimation introduced by the Glauber model. In that work, two sources of biases were studied: 1) geometry bias, which relates to correlations between Pb+Pb impact parameter and the nucleon–nucleon impact parameter (b_{nn}), and 2) selection bias that takes into account possible correlations between hard and soft particle production that bias the centrality estimators in forward rapidities.

The reason for the first source of bias is coming from the fact that the displacement of nucleons in a beam of ions is different compared to the one of the beams of protons. That implies that peripheral Pb+Pb collisions tend to be more biased towards more peripheral nn collisions which affects the rate of the multiple parton scatterings. The selection bias further arises due to the fact that hard and soft production equally reflect the geometry

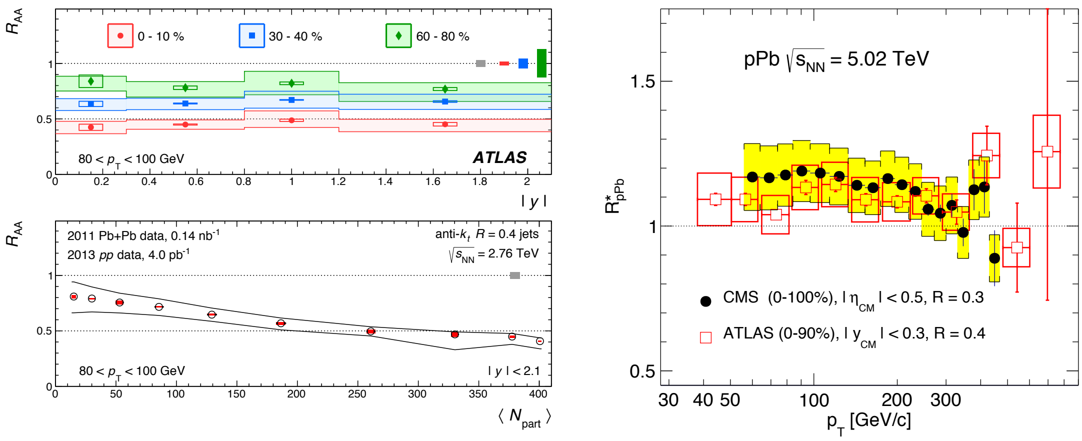

Figure 14: (*Left*) The upper panel shows the nuclear modification factor R_{AA} of high-p_{T} jets versus jet rapidity measured in three centrality intervals by ATLAS in the $\sqrt{s_{\mathrm{NN}}} = 2.76$ TeV Pb+Pb data [87]. In the lower panel the jet R_{AA} is shown as a function of $\langle N_{\mathrm{part}} \rangle$ for jets with $|y| < 2.1$ and $80 < p_{\mathrm{T}} < 100$ GeV. (*Right*) Nuclear modification factor $R_{p\mathrm{A}}$ as a function of p_{T} for jets in the p+Pb system measured by ATLAS (open squares) [82] and CMS (filled circles) [92] in the $\sqrt{s_{\mathrm{NN}}} = 5.02$ TeV p+Pb data.

bias and the centrality selection in the data is determined by the soft production. In that case. more peripheral centrality classes will be biased towards larger values of b_{nn}.

To formally model these biases, the value of the R_{AA} absent of any nuclear effects was determined using the HG-PYTHIA model, which describes nucleus-nucleus collisions using the HIJING [94] event generator and superimposes a PYTHIA 6.4 [95] event for each hard sub-interaction specified by the generator. HIJING was tuned such that no quenching or shadowing effects were simulated. The centrality association in the model was done by ordering events according to the charged-particle multiplicity measured in $2.5 < \eta < 5$.

Figure 15 shows the model prediction for the charged hadron R_{AA} compared with CMS data (left) and ALICE data (right). The model can qualitatively explain the measured peripheral suppression and it implies that biases in R_{AA} calculation need to be taken into account before the measurement is interpreted as a charged particle energy loss in the QGP medium. Within the model, the same is expected to hold for the peripheral R_{AA} associated with observables produced by any hard scattering process, such as EW bosons. In this work, we further investigate this prediction by measuring the Z boson yields in

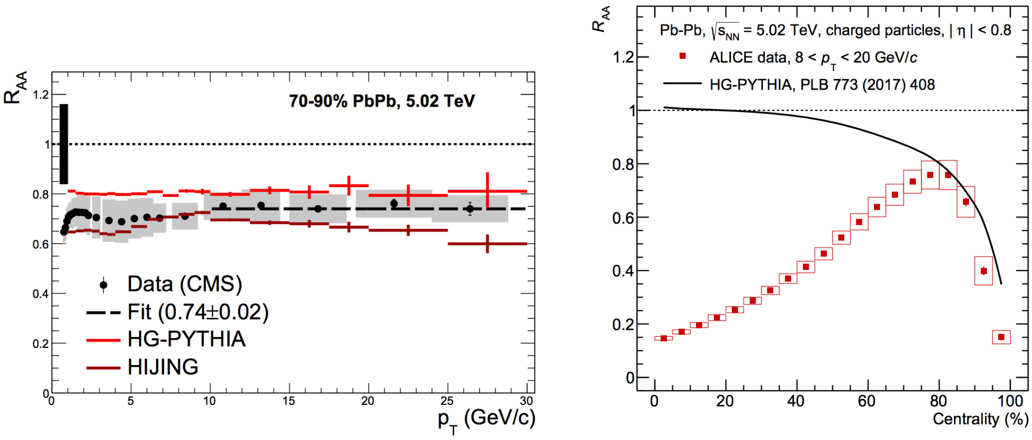

Figure 15: (*Left*) Nuclear modification factor R_{AA} for charged particles versus p_{T} in 70–90% central Pb+Pb collisions at $\sqrt{s_{\mathrm{NN}}} = 5.02$ TeV for the CMS data [84] compared to HG-PYTHIA and HIJING calculations. (*Right*) Average R_{AA} for $8 < p_{\mathrm{T}} < 20$ GeV as a function of centrality percentiles in Pb+Pb collisions at $\sqrt{s_{\mathrm{NN}}} = 5.02$ TeV by ALICE [96] compared to predictions from HG-PYTHIA.

ultra-peripheral Pb+Pb collisions, extended for the first time beyond 80% centrality. In this region, it is no longer justifiable to neglect electromagnetic corrections to Z boson production yield.

4.4 Photon-induced interactions in ultra-peripheral collisions

In peripheral Pb+Pb collisions, the contribution from electromagnetic (EM) processes becomes significant compared to the rate of hadronic collisions. The reason for this are the strong EM fields of fully ionized colliding nuclei that in the equivalent photon approximation correspond to a flux of high-energy photons. These coherent photon fields from the two nuclei can interact and scatter even when the impact parameter is large (more than twice the nuclear radius); hence, this class of physics processes is usually referred to as "ultra-peripheral collisions" (UPC) [97]. Since the photon spectrum is enhanced by Z^2, the rates of EM interactions are comparable to rates of hard processes that scale with T_{AA}.

UPC events are used to study exclusive vector-meson production in photon–nucleus collisions [98–102], lepton-pair production in photon–photon collisions [103] and recently the light-by-light scattering [104, 105]. In this class of events there are two physical processes that contribute to the final Z boson yield: photon–photon scattering, $\gamma\gamma \to \ell^+\ell^-$ [106–108] shown in the left panel of Figure 16 and photon–nucleus scattering $\gamma + A \to Z \to \ell^+\ell^-$ [109] (right panel of Figure 16).

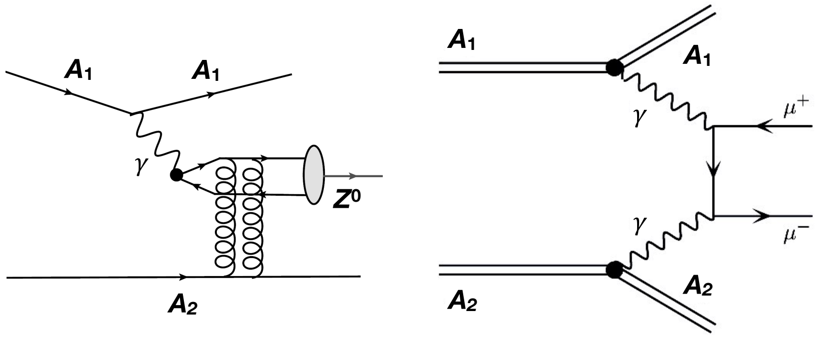

Figure 16: (*Left*) An illustration of the Z photoproduction mechanism in an ultra-peripheral nucleus-nucleus collision. (*Right*) A diagram for the exclusive dimuon production in the photon-photon scattering.

Although measurements of exclusive high-mass dilepton production have been performed in *pp* and Pb+Pb collisions by ATLAS [110, 111] and in *pp* collisions by CMS [112], a photo-nuclear Z boson production has not yet been observed in HI collisions. Both physics processes are characterized by large rapidity gaps on one or both sides of the detector (regions with no particle production recorded in the detector). This feature of the event topology of the UPC production allows identifying and subtracting these events when treated as a background contribution to the nominal hadronic Z boson production.

5 Measurement methodology

In this chapter, we discuss the exact measurement procedure required to extract the Z boson yield. In Section 5.1 we introduce all the relevant detector observables used in the measurement which are: the total number of reconstructed Z boson candidates, the various background processes that need to be subtracted, the detector efficiency correction and the overall measured normalization factor. The quantities are presented in greater detail in subsequent sections. Section 5.2 summarizes conditions for the event selection and the lepton reconstruction in the ATLAS detector applied for reconstructing Z bosons.

In Section 5.3 we list all the simulation samples used in the analysis, while in Section 5.4 we discuss different physics processes contributing to the total number of background events. Section 5.5 discusses the derivation of the correction factor for the detector efficiency and resolution while Section 5.6 describes how this correction is measured in different decay channels and collision systems. Finally, in Section 5.7 we describe different sources of measurement uncertainties for the final result.

5.1 Definition of observables

The fiducial cross section for Z boson decays is defined for particles in the mass range of $66 < m_Z < 116$ GeV decaying into leptons in the phase space defined by kinematic cuts $|\eta^l| < 2.5$ and $p_{\mathrm{T}}^l > 20$ GeV calculated on the generated level. The methodology of the measurement consists of counting the number of reconstructed Z boson candidates in the fiducial space defined by the lepton selection, subtracting the number of background candidates and finally correcting the data for the detector effects. The same methodology is employed for both muon and electron decay channels before channels are combined for the final result. The expression for the fiducial cross section times the branching ratio of the Z boson is:

$$\sigma_{\mathrm{fid}}^Z \times BR(Z \to ll) = \frac{N_{\mathrm{fid}}^Z}{C_Z \cdot \mathcal{L}} = \frac{N_{\mathrm{reco}}^Z - N_{\mathrm{bkg}}^Z}{C_Z \cdot \mathcal{L}}, \tag{18}$$

where

- N_{fid}^Z represents the number of Z bosons in the fiducial acceptance,
- N_{reco}^Z is the number of Z boson candidates, selected on the reconstructed level,
- N_{bkg}^Z is the number of background candidates,
- C_Z is the correction factor accounting for the detector acceptance, efficiency and resolution,
- $\mathcal{L}$ is the total integrated luminosity of the analyzed data sample.

In Pb+Pb collisions, an equivalent of the measured cross section is the normalized yield of Z bosons, i.e. the Z yield per inelastic collision normalized by the amount of the nuclear overlap. From Equations 16 and 18 it follows:

$$N_{AA}^{Z'} = \frac{N_{\text{reco}}^{Z} - N_{\text{bkg}}^{Z}}{C_Z \cdot N_{\text{evt}} \cdot T_{\text{AA}}},$$

where $N_{AA}^{Z'}$ denotes the normalized Z yield in the Pb+Pb system, T_{AA} is the nuclear thickness function and N_{evt} is the number of MB events as explained in Section 2.4.

5.2 Event selection

The number of reconstructed Z boson candidates, N_{reco}^{Z}, is obtained in both muon and electron decay channels after applying the selection at the event level and on the reconstructed leptons. All events are selected according to detector quality conditions during the data taking summarized in the "Good Run List" (GRL) to ensure a high quality of events selected for physics analyses. Events are required to have a reconstructed primary vertex which is required to have least two tracks associated with and the highest sum of the associated-track transverse momenta among all vertices.

According to the allocated bandwidth in the trigger menu, the lowest-p_{T} triggers used to select events with high-energy muons required a muon candidate with at least 14 GeV (8 GeV) transverse momentum in *pp* (Pb+Pb) events. In the electron channel, due to a larger background contribution a trigger algorithm applies selection on the electron shower in the calorimeter (defined as "loose") while requiring candidates with $p_{\text{T}} > 15$ GeV. Further offline kinematic requirements applied to leptons include $p_{\text{T}} > 20$ GeV (in the plateau of the trigger efficiency) and $|\eta| < 2.4$ (2.47) for muons (electrons) that limits the measurement to the precision region of the EM calorimeter and the muon (RPC trigger) system.

5.2.1 Muon reconstruction and identification

The combined ID–MS muon reconstruction is performed according to various algorithms based on the information provided by the ID, MS and calorimeters. Four muon types are defined depending on which subdetectors are used in reconstruction:

- *Combined (CB) muon*: track reconstruction is performed independently in the ID and MS, and a combined track is formed with a global refit that uses the hits from both the ID and MS subdetectors;

- *Segment-tagged (ST) muons*: a track in the ID is classified as a muon if, once extrapolated to the MS, it is associated with at least one local track segment in the MDT or CSC chambers;

- *Calorimeter-tagged (CT) muons*: a track in the ID is identified as a muon if it can be matched to an energy deposit in the calorimeter compatible with a minimum-ionizing particle;

- *Extrapolated (ME) muons*: the muon trajectory is reconstructed based only on the MS track and a loose requirement on compatibility with originating from the IP.

Offline muons used in *pp* and Pb+Pb systems are required to be combined muons. Further muon identification requirements are imposed to suppress background muons, mainly from pion and kaon decays. Several variables useful for the discrimination of prompt and background muons are listed below:

- q/p significance, defined as the absolute difference between the muon charge-to-momentum ratios measured in the ID and MS divided by the sum in quadrature of the respective uncertainties;

- ρ, defined as the absolute difference between transverse momentum measurements in the ID and MS divided by the transverse momentum of the combined track;

- normalized χ^2 of the combined track fit;

- specific requirements on the number of hits (precision layers) in the MS.

This analysis uses the *medium* identification working point which is the default selection for muons in ATLAS. For the ID tracks, the quality cuts require at least one Pixel hit, at least five SCT hits and fewer than three Pixel or SCT holes. Medium selection requires muons to have at least 3 hits in at least two MDT layers, except for tracks in the $|\eta| < 0.1$ region, where tracks with at least one MDT layer but no more than one MDT hole layer are allowed. A loose selection on the compatibility between ID and MS momentum measurements is applied, requiring the q/p significance to be less than seven. In the Pb+Pb system, due to the saturation of the TRT detector, no requirements are made on the TRT signatures while all the order requirements are the same as applied in the *pp* system.

Analysis performed in the pp system uses isolation requirements, imposed on muon candidates in order to suppress the multi-jet background. Specifically, *FixedCutTight* requirement consists of cuts on track-based and calorimeter-based variables:

- $p_{\mathrm{T}}^{\mathrm{varcone30}}/p_{\mathrm{T}}^{\mu} < 0.06$, where $p_{\mathrm{T}}^{\mathrm{varcone30}}$ is the sum of transverse momenta of tracks in a cone around a muon, excluding the muon track itself. The cone size $\mathrm{d}R = \sqrt{\Delta\eta^2 + \Delta\phi^2}$ is chosen as Min(10 GeV/p_{T}^{μ}, 0.3).

- $E_{\mathrm{T}}^{\mathrm{topocone20}}/p_{\mathrm{T}}^{\mu} < 0.06$, where $E_{\mathrm{T}}^{\mathrm{topocone20}}$ is the sum of transverse energies of topoclusters in a cone of radius $\mathrm{d}R = 0.2$ around the muon, excluding the muon energy deposit itself.

The isolation requirement is not used in the analysis of Pb+Pb data due to a much larger size of the underlying event. That results in a strong dependence of the signal loss on event centrality, and as a result, a significant additional correction with the corresponding systematic uncertainty.

5.2.2 Electron reconstruction and identification

Electrons are reconstructed in ATLAS from the combination of a cluster of energy deposits in the EM calorimeter (EM cluster) and a matching ID track. Electromagnetic-energy cluster candidates are then seeded from localized energy deposits using a sliding-window algorithm [113] of size 3×5 towers in $\eta \times \phi$, whose summed transverse energy exceeds 2.5 GeV. The efficiency to detect an energy cluster with the sliding window algorithm in the EM calorimeter is found to be above 99% for $E_{\mathrm{T}} > 15$ GeV [114]. The track matching starts with track reconstruction from seeds formed of three space-points in the silicon detector layers and proceeds with a Gaussian-sum filter [115] fitting procedure that performs matching to EM clusters. Above $E_{\mathrm{T}} = 15$ GeV, the efficiency to reconstruct an electron having a track of good quality (at least one pixel hit and at least seven silicon hits) varies from approximately 97% to 99%. The energy of the final electron candidate is computed from the calibrated energy of the EM cluster while the ϕ and η directions are taken from the corresponding track parameters.

To further reduce the background coming from hadronic jets or converted photons, algorithms for electron identification are applied. The identification algorithms use quantities related to the electron cluster and track measurements including calorimeter shower shapes, information from the TRT, track-cluster matching related quantities, track properties, and variables measuring bremsstrahlung effects for distinguishing signal from background candidates. The baseline identification algorithm used for Run-2 data analyses is the likelihood (LH) method. It is a multivariate analysis technique that simultaneously evaluates several properties of the electron candidates when making a selection decision. In *pp* data, *LH medium* working point is selected for the analysis that is optimized for identification efficiency from 80% at 20 GeV to 95% at 120 GeV, with on average 5% higher efficiency in the EM barrel compared to the endcaps. Dedicated studies have been performed in order to optimize the working points of the LH method to conditions observed in Pb+Pb collisions [116]. Finally, *LH loose* working point is used for the electron candidate selection providing the identification efficiency in the range from 80%–90% that is approximately constant with $\Sigma E_{\mathrm{T}}^{\mathrm{FCal}}$. The same isolation definition as in the muon channel is further required in the *pp* data to suppress the multi-jet background. Due to a large EM calorimeter occupancy in Pb+Pb events, no isolation condition is required in addition to the Loose LH working point.

Selection criteria applied on reconstructed muons and electrons in *pp* and Pb+Pb systems together with the number of identified candidates are given in Table 3.

system	mode	trigger	p_T^ℓ	$\lvert\eta^\ell\rvert$	ID	Iso	counts
pp	$\mu\mu$	HLT_mu14	> 20 GeV	< 2.4	medium	fixed tight	7368
pp	*ee*	HLT_e15_lhloose _L1EM13VH	> 20 GeV	< 2.47	LH medium	fixed tight	4820
Pb+Pb	$\mu\mu$	HLT_mu8	> 20 GeV	< 2.4	medium, no TRT	none	5375
Pb+Pb	*ee*	HLT_e15_loose _ion_L1EM12	> 20 GeV	< 2.47	LH loose	none	4034

Table 3: Summary of the event and object selection requirements used in the analysis.

5.3 Monte Carlo simulation samples

To calculate both C_Z and N^Z_{bkg}, several Monte Carlo (MC) samples were used in the *pp* and Pb+Pb analyses for simulating signal and background processes. The Z and W boson production samples were generated with the Powheg Monte Carlo program [117] interfaced with the Pythia v.8.1 parton shower program [118]. The generators used the CT10 PDF set [119] and the AZNLO CTEQL1 tune for Powheg+Pythia samples. Background process samples for $t\bar{t}$ decays were generated with the Powheg v2 generator and Pythia v.6.4 (Perugia 2012 tune).

Process	Generator	σ·BR [pb]	Events $\times 10^6$
$Z \to \mu\mu$	Powheg+Pythia8	642.8	1.0
$Z \to ee$	Powheg+Pythia8	642.8	1.3
$Z \to \tau\tau$	Powheg+Pythia8	642.7	0.3
$t\bar{t}$	Powheg+Pythia6	56.6	0.069
$W^+ \to \mu^+\nu$	Powheg+Pythia8	4190.1	1.0
$W^- \to \mu^-\bar{\nu}$	Powheg+Pythia8	2737.2	0.7

Table 4: List of simulation samples used in the *pp* analysis denoting the generator used, cross section for the physics process and the number of simulated events.

The number of simulated events is motivated by the desired percent-level precision in p_{T} and y kinematic bins of reconstructed Z bosons. Table 4 shows the summary of simulated signal and background samples for *pp* analysis together with their corresponding cross sections and the produced number of events.

In Pb+Pb analysis, a proper isospin combination of the samples needed to be produced including the *pp*, *pn*, *np* and *nn* MC events. For lead, A=208 and Z=82; hence all the samples with two neutrons have the weight of 36.7%, events with two protons 15.5% and different nucleon combinations have weights of 23.9% (*pn*, *np*). Once produced, the simulated events are overlaid onto minimum bias events taken during the Pb+Pb run in order to account for detector effects related to the high occupancy and are finally reconstructed by the usual ATLAS event reconstruction. The minimum bias events used for the overlay are taken with different prescales such that the distribution in centrality, based on the energy deposited in the forward calorimeters $\Sigma E_{\mathrm{T}}^{\mathrm{FCal}}$ roughly approximates that of Z boson events. To account for the residual effects the MC events were given weight to match the energy distribution in the forward calorimeter measured in the Z-boson sample. The EW background samples were simulated only in the pp configuration since the impact of isospin effects on the background estimation is negligible. Table 5 shows the summary of simulated samples for Pb+Pb analysis.

Process	Generator	p_{T} range [GeV]	Events $\times 10^6$			
			pp	pn	np	nn
$Z \to \mu\mu$	Powheg+Pythia8	inclusive	0.2	0.3	0.3	0.45
$Z \to \mu\mu$	Powheg+Pythia8	> 25	0.22	0.34	0.34	0.51
$Z \to ee$	Powheg+Pythia8	inclusive	0.31	0.47	0.47	0.72
$Z \to ee$	Powheg+Pythia8	> 25	0.43	0.66	0.66	1.01
$Z \to \tau\tau$	Powheg+Pythia8	inclusive	0.2			
$t\bar{t}$	Powheg+Pythia6	inclusive	0.07			

Table 5: List of simulation samples used in the Pb+Pb analysis denoting the generator used, p_{T} range and the number of simulated events.

5.4 Background

Several background sources contribute to N_{bkg}^{Z} defined in Equation 18. They can be divided into two categories - background sources that are estimated from MC simulation and those estimated directly from data. All background sources described below are considered in both pp and Pb+Pb events, except for the electromagnetic background that is subtracted only in Pb+Pb events.

5.4.1 Electroweak and top quark decays

Contribution to background events originate from Z decays to τ lepton that further decays into an electron or a muon, W boson decays in leptonic channels, diboson production and finally, top quark ($t\bar{t}$) decays into lepton+jets and dilepton final states. The expected number of background events for these sources has been evaluated from MC samples after scaling the number of events to the data luminosity. The diboson background is subtracted only in *pp* events following the procedure from previous ATLAS publications [85, 120]. The diboson background contributes 0.08% in the muon channel and 0.14% in the electron channel. The $Z \rightarrow \tau^+\tau^-$ background is found to be at the level of 0.07% in both decay channels. The top-quark background is at the level of 0.06% in the electron channel and 0.08% in the muon channel. The W boson background is found to be below 0.01% in both channels. Figure 17 shows detector-level dilepton rapidity distributions for electron

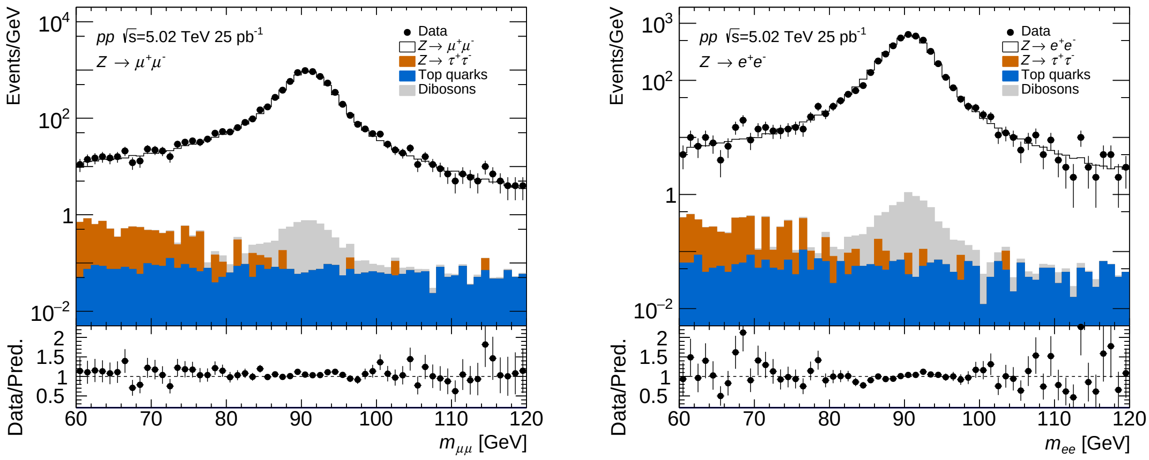

Figure 17: Detector-level invariant mass distribution of dimuon (*left*) and dielectron pairs (*right*) from Z boson decays together with EW and top quark background contributions. Only the statistical uncertainties of the data are shown.

and muon candidates from Z boson decays. Good agreement is found between the data and the sum of the signal and background contributions.

In the Pb+Pb system, the $Z \rightarrow \tau^+\tau^-$ background is found to be 0.05% of all signal candidates in the muon channel and 0.06% in the electron channel. The top-quark background amounts to 0.08% in the muon channel and 0.05% in the electron channel. The background contribution from W boson decays and W+jet production is found to be negligible.

5.4.2 Multi-jet background

A significant contribution to the background is coming from the QCD multi-jet events with dileptons in the final state originating from jets, misidentified hadrons and, in the electron channel, from converted photons. In the pp measurement, this background contribution is estimated in the muon channel from samples that simulate $b\bar{b}$ and $c\bar{c}$ production. Performed studies yield estimates at the level below 0.01%. A previous ATLAS measurement at $\sqrt{s} = 7$ TeV [85] estimated the multi-jet contribution at the level of 0.02–0.15% for the electron channel and 0.09% for the muon channel. This background also includes jets coming from the pile-up event and therefore is expected to increase with an increasing pile-up. Since 7 TeV data were taken at higher pile-up conditions compared to 5.02 TeV data the two independent estimates of the multi-jet background do not contradict each other. In the pp analysis, this small contribution is neglected.

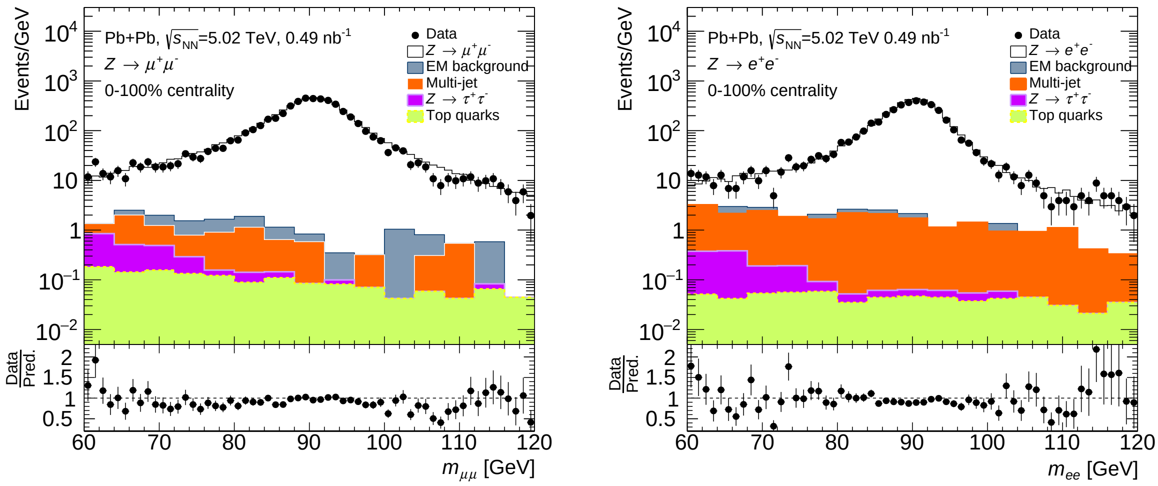

Figure 18: Detector-level invariant mass distribution of dimuon (*left*) and dielectron (*right*) pairs together with the $Z \to \tau^+\tau^-$, top quark, multi-jet and EM background contributions measured in the 0–100% centrality interval. Only the statistical uncertainties of the data are shown.

In the Pb+Pb system, the multi-jet background contribution is found to be significant. In the muon channel, its contribution is estimated from the distribution of the same-sign Z boson candidates in rapidity and centrality. Due to the low charge misidentification rate in the muon spectrometer, their invariant mass distribution does not exhibit a peak in the Z boson mass region as is seen in the left panel of Figure 18. In the muon channel, this background amounts to 0.5% of all signal candidates. In the electron channel, there is a significant contribution from charge misidentification, fakes and conversions. The electron same-sign pairs, therefore, cannot be used to estimate the multi-jet background. Its contribution is estimated using background templates extracted from data in Z boson rapidity and event centrality. Templates shown in Figure 19 are derived from events

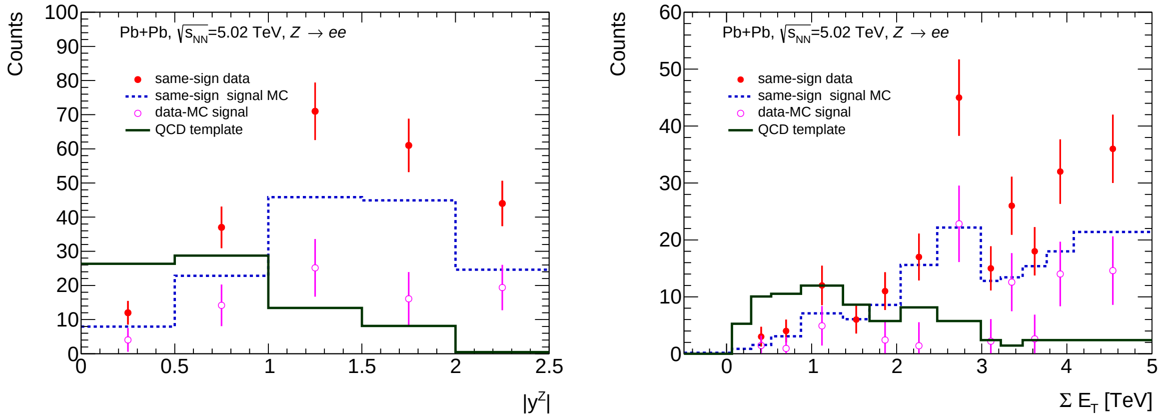

Figure 19: Multi-jet background templates in the Pb+Pb electron channel measurement obtained from data as a function of rapidity (*left*) and $\Sigma E_{\mathrm{T}}^{\mathrm{FCal}}$ (*right*) shown in green histograms. Same-sign candidates from data (red markers) and simulation (blue dashed line) are also shown, together with their difference (open magenta markers).

corresponding to misidentified jets, i.e. electrons with a very poor reconstruction quality. Both templates are normalized to the same-sign data distribution shown in the right panel of Figure 18 in the region of $60 < m_{ee} < 70$ GeV after subtracting the signal obtained from the MC simulation. Due to the small number of signal candidates satisfying conditions for the template selection, same-sign electron pairs with the same kinematic requirements are also added to this background template.

5.4.3 Photon-induced background

Photon-induced events constitute a background source specific to the Pb+Pb system, as described in Section 4.4. This background has been studied for the first time in this work, and therefore it is described in greater detail. EM reactions are enhanced by the strong fields of colliding heavy nuclei generated by their electric charge. It has recently been shown that at the LHC energies the EM processes can be detected in all centrality classes [26], including the most central Pb+Pb collisions. However, the EM dilepton production in the high-mass range relevant to this study has a low rate and therefore significantly affects Z boson yields only in peripheral collisions.

For all photon-induced processes, the event topology is expected to contain large pseudorapidity gaps on one side or on both sides that start at the edge of the detector.

Generally, the photon-photon scattering interactions would have a two-sided gap topology and the photonuclear collisions a one-sided. Excluding events with large rapidity gaps eliminates most of the background, except those events that occur simultaneously with a hadronic collision, in which the gap is masked by a hadronic interaction. Those events are treated separately by studying the kinematic of the dilepton pair and introducing additional requirements on the dilepton acoplanarity for the final background estimate.

The ATLAS detector subsystems that are used to measure the event activity and calculate gaps are the ID with the coverage extending to 2.5 units, calorimeters extending to 5 units, and the ZDC covering the rapidity range above 8 units. The physics processes that produce signals in the ZDC are different from those in the central part of the detector, however, if the Pb ion undergoes a hadronic collision the probability of it staying intact is very small and the ZDC would register neutrons emitted from fragmenting ions. In this regard, the presence of a gap in the central part of ATLAS and an absence of a neutron in the ZDC indicate that the underlying interaction possesses an EM nature. The yields of EM events, therefore, can be significantly suppressed by requiring the ZDC coincidence signal. This corresponds to requiring at least 1 TeV of energy (which is 40% of the single neutron energy) measured in ZDC on each side of the detector.

Figure 20 shows activity in detector subsystems for four selected events in the peripheral centrality interval. An event shown in the top left panel is a typical event of the Z boson produced in a hadronic interaction – the recorded energy in ZDC and FCal detectors is large and there is a significant activity in EMCal and ID. The top right panel shows an event with a single-sided ZDC signal. On the same side as the ZDC there is a number of tracks and clusters of a GeV-energy scale. This event is consistent with the photonuclear ($\gamma + A$) Z-boson event topology. Two lower panels show events with gaps on both sides of the detector. The lower left panel shows that due to the dissociation of one of the participating nuclei the UPC-like events can have fragmenting neutrons registered in one arm of the ZDC detector. All three events shown in the figure where no ZDC coincidence was recorded are treated as background.

The rapidity gap analysis is implemented using the technique developed in [121]. Events with the gap larger than 2.5 are marked as having a gap on one or two sides. Table 6 shows all events selected for the analysis with respect to ZDC signal and the gap measurement. Events with ZDC < 2 as well as the events with gaps are excluded

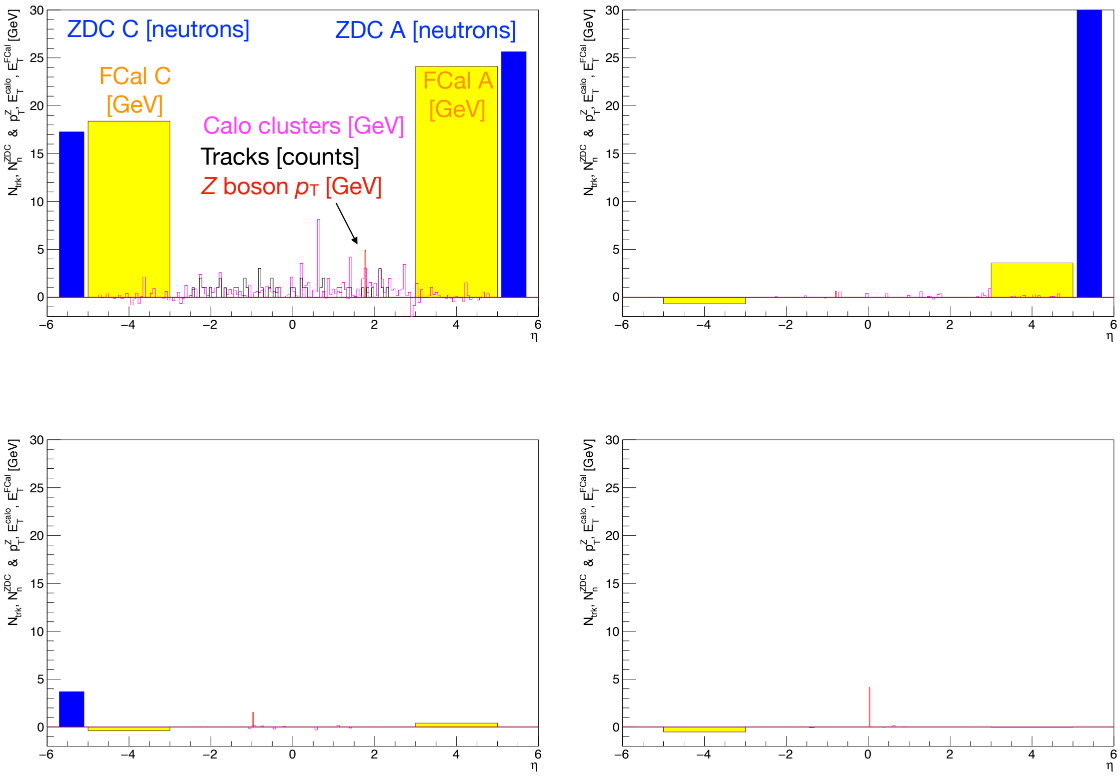

Figure 20: Pseudorapidity distributions of the detector activity in four selected peripheral events showing signals from ZDC (blue), FCal (yellow), EMCal (magenta) and ID tracks (black). The position of the Z boson is indicated in red. Magnitude of each signal is in GeV or in counts, depending on the subsystem.

from the analysis leading to the final result. These two conditions exclude mostly the same events. The total of 27 events with two gaps are candidates for UPC photon-photon scattering events. The STARLIGHT 1.1 Monte Carlo generator [122] in the Z boson mass region and the lepton fiducial space defined for this measurement ($p_{\mathrm{T}} > 20$ GeV, $|\eta| < 2.5$, $66 < m_{ll} < 100$ GeV) predicts 15.7 ± 1.0 UPC $\gamma + \gamma$ events. A similar excess in data compared with simulation has already been seen in the dedicated measurement in the high-mass region [111]. The ZDC fractions can also be obtained from the generator and they yield $f_0 = 0.37$, $f_1 = 0.41$, $f_2 = 0.21$ for ZDC=0, ZDC=1 and ZDC=2, respectively. This is consistent with data shown in the table where the measured fractions are $f_0 = 0.6 \pm 0.2$, $f_1 = 0.2 \pm 0.1$, $f_2 = 0.2 \pm 0.1$. The probability of the neutron fragmentation can also be estimated from the UPC candidates identified in this analysis and it yields

	ZDC=0	ZDC=1	ZDC=2
2 gaps	14	7	6
1 gap		4	3
no gap		1	9483

Table 6: ZDC signals and gaps in all events for both decay channels. Few very central events having one sided ZDC signal due to no neutrons left after interaction, are still attributed as ZDC=2 in this table.

about 0.4.

The 34 events with gaps were used to understand the contribution of the photon-induced collisions in more central interactions in which the topology analysis is not feasible because gaps are masked by a simultaneous hadronic interaction. It was estimated by re-weighting the gap distribution measured in *pp* events with the ratio of multiplicity distributions in events with Z and in inclusive events that the contribution of hadronic Z production among those events is approximately 0.05 events.

Instead of the topological analysis, one can use the fact that in the photon-photon scattering, the final state is produced mostly at rest, i.e. leptons must be back-to-back in azimuth with nearly identical transverse momenta. One can characterize this by defining the acoplanarity as:

$$Aco \equiv 1 - \frac{|\phi^+ - \phi^-|}{\pi},$$

where $\phi^\pm$ are the azimuthal angles of two leptons. Data and the STARLIGHT simulation agree that about 96% of dilepton candidates produced by $\gamma + \gamma$ scattering have $Aco < 0.01$ [111]. It is further assumed that the photonuclear reaction would also produce a final state with low transverse momentum and therefore small acoplanarity. Since photonuclear reaction with the Z boson in the final state was not yet positively identified in any experiment, this assumption was treated as false when working out the systematic uncertainties.

Among the 34 events with gaps that are identified as the background, 26 events also have $Aco < 0.01$. This demonstrates that the acoplanarity is highly sensitive to the photon-induced reactions in the Z boson invariant mass region. Using the last two numbers, the data-driven estimation that the EM background event survives the acoplanarity cut is $\epsilon_1 = 24 \pm 8\%$ based on the available statistics in both decay channels. The acoplanarity selection cut $Aco > 0.01$ applied to hadronic Z boson candidates selects $\epsilon_0 = 86.4 \pm 0.4\%$ fraction of all event, where the error is calculated from the difference between the estimators obtained from the data in more central collisions and the MC simulation shown in Figure 21. The data and the MC simulations agree well for $\Sigma E_{\mathrm{T}} > 1$ TeV

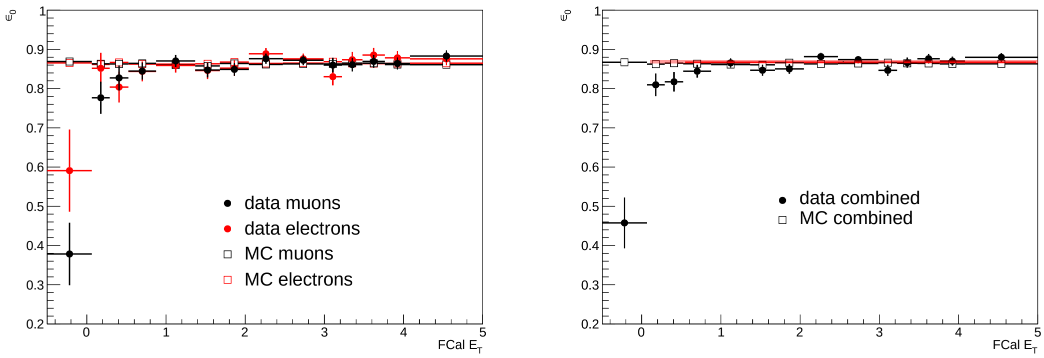

Figure 21: (*Left*) Fraction ϵ_0 of Z boson candidates after applying the acoplanarity selection $Aco > 0.01$ versus $\Sigma E_{\mathrm{T}}^{\mathrm{FCal}}$ for data and simulation separately for electron (red markers) and muon (black markers) decay channels. (*Right*) The same fraction ϵ_0 shown for the combined data. The red line shows the uncertainty on the linear fit of the data in the region of 0–50% centrality.

but below this value, the fraction of survived events in the data diminishes due to presence of the EM background. An energy to which the EM background contributes significantly is hard to asses due to limited statistics, therefore in the analysis we apply the EM background rejection to the three most peripheral centrality intervals because the points in them are more than two standard deviations below the MC simulation and below the fit to the points at higher centrality.

Using values of ϵ_0 and ϵ_1 it is estimated that in the 80–100% centrality interval, besides the events with a large rapidity gap, 7 ± 3 out of 28 remaining candidates originate from photon-induced reactions. In the 60–80% interval this number is 15 ± 5 out of 182, and in the 50–60% interval it is 18 ± 8 out of 258, where the uncertainty includes statistical and systematic uncertainties in the background, but not in the number of event candidates. In more-central collisions, the method of estimating the photon-induced background is limited by the statistical precision of the sample and this contribution is consistent with zero. These 40 ± 10 events are a contribution to N_{bkg}^{Z} in Eq. 18, and shown in Figure 18 using mass distribution of 34 events listed in Table 6.

5.4.4 Pile-up events

Unrelated collisions or part of those, recorded together with the collision of interest are referred to as "pile-up". Pile-up typically does not affect the Z boson reconstruction directly, but it modifies the underlying event or the event counting. For the measurement of the cross section done in pp, the pile-up is properly taken into account by the luminosity determination. In Pb+Pb it alters the FCal energy leading to incorrect determination of the event centrality.

Pile-up modifies the FCal response in two different ways. Multiple interactions within the same bunch crossing (*in-time pile-up*) increase the $\Sigma E_{\mathrm{T}}^{\mathrm{FCal}}$, shifting the Z boson to a more-central interval. Collision preceding the trigger event (*out-of-time pile-up*), add negative values to $\Sigma E_{\mathrm{T}}^{\mathrm{FCal}}$ due to long temporal response of signal shapers used in the calorimeters [123] that also flip the sign of the signal. In this case, the Z boson candidate is shifted to a more-peripheral interval. A transfer of Z boson candidates between centrality intervals shall be compared to an undisturbed centrality profile. Z-boson production, as a hard process, is known to rapidly grow from peripheral to central events following the $\langle T_{\mathrm{AA}} \rangle$ scaling [62].

The probabilities of both pile-up processes depend on the instantaneous luminosity during data taking. At any time during the HI run, the number of hadronic interactions per bunch crossing was less than 0.01 (with an average value of 0.002). Due to that small instantaneous luminosity, the effect of the in-time pile-up that moves events from less-populated peripheral to more-populated central intervals is found to be negligibly small. The effect of the out-of-time pile-up transferring in the opposite direction has been studied using several independent data-driven and simulation-based approaches. The largest contribution to the most peripheral 80–100% centrality interval due to this type of the pile-up is less than 2%, i.e. less than one count, and is significantly less in any other centrality range.

5.5 Correction factor C_Z

The correction factor C_Z is evaluated from the MC simulation for each decay channel and is defined as:

$$C_Z(p_{\mathrm{T}}^Z, y^Z) = \frac{N_{\mathrm{reco}}^Z(p_{\mathrm{T}}^Z, y^Z)}{N_{\mathrm{gen}}^Z(p_{\mathrm{T}}^Z, y^Z)}, \tag{19}$$

where N_{gen}^Z is the number of generated Z bosons in the fiducial acceptance and N_{reco}^Z is the number of reconstructed Z bosons after the full analysis selection and cuts that are listed in Table 3. The denominator is computed by applying the fiducial phase-space requirements to the generator-level leptons originating from Z boson decays. The measurement is corrected for QED final-state radiation effects by using the generator-level lepton kinematics before photon radiation. In the case where the MC simulation perfectly models the detector performance during the run, the correction factor given by Equation 19 that accounts for the detector efficiency and resolution would unfold the result to the particle level cross section defined by Equation 18.

In the Pb+Pb system due to the limited size of the MC simulation, the dependence of C_Z on rapidity, momentum and centrality is calculated from the simulation as:

$$C_Z(p_{\mathrm{T}}, y, \Sigma E_{\mathrm{T}}^{\mathrm{FCal}}) = F(p_{\mathrm{T}}, y) \cdot G(y, \Sigma E_{\mathrm{T}}^{\mathrm{FCal}}), \tag{20}$$

where $F(p_{\mathrm{T}}, y)$ is the centrality-averaged efficiency calculated per y and p_{T} interval of the dilepton system and $G(y, \Sigma E_{\mathrm{T}}^{\mathrm{FCal}})$ is a factor that accounts for the centrality dependence of the efficiency. In each rapidity bin, the factor G is obtained from a parabolic fit to the ratio of the efficiency in a particular centrality bin to the value averaged over all centrality values, i.e. $F(p_{\mathrm{T}}, y)$. Figure 22 shows the correction map $F(p_{\mathrm{T}}, y)$ in the left panel and the parametrization $G(y, \Sigma E_{\mathrm{T}}^{\mathrm{FCal}})$ in the right panel for the muon decay channel.

Scale Factor Approach. In some analyses, there exists a possibility to derive detector subsystem efficiency based on a data-driven approach. It uses the redundancy of information provided by several ATLAS detector subsystems, which greatly improves the accuracy of the measurements. Technically, the approach is based on the so-called *tag-and-probe method*, explained in detail in Section 5.6.

Deriving efficiency entirely from simulation or data both have disadvantages. For example possible inconsistencies in the MC description of the detector or presence of

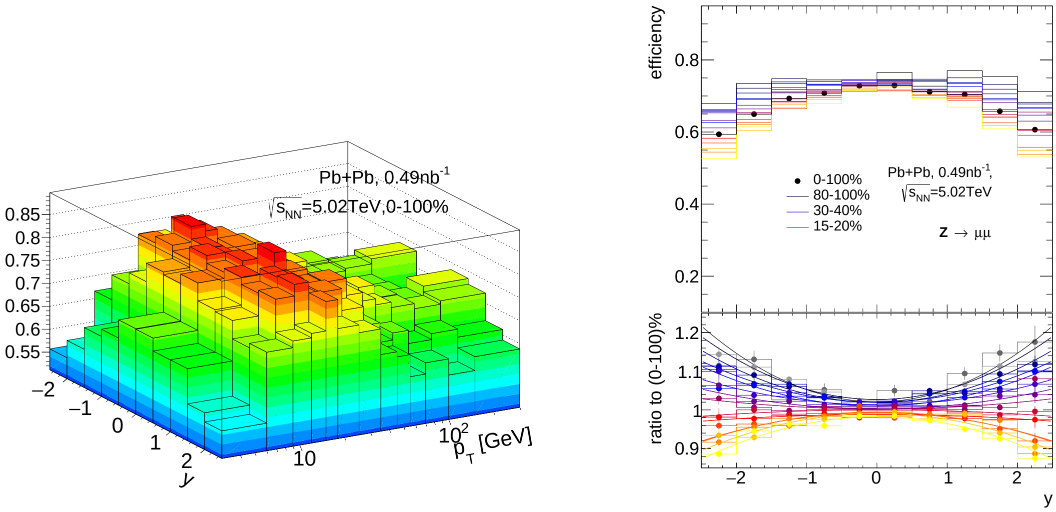

Figure 22: (*Left*) The Z boson reconstruction efficiency $F(p_{\mathrm{T}}, y)$ in the muon decay channel. (*Right*) The $F(y)$ distribution in different centrality classes (colored histograms) and averaged in 0-100% centrality (black markers) in the upper panel and $G(y, \Sigma E_{\mathrm{T}}^{\mathrm{FCal}})$ for different centrality classes in the bottom panel fitted to parabolas.

physics biases in the data. To achieve the best of the two measurements, the ATLAS experiment uses the approach based on so-called scale factors (SF) that are the ratios of the two efficiencies measured in data and MC using the identical TnP approach. In the construction of the ratio, physics biases that are present in both samples cancel out, and inconsistencies of the MC descriptions are corrected for. Scale factors are defined for particular efficiency measurement as:

$$\mathrm{SF}_i(\mathrm{X}) = \frac{\epsilon_i^{\mathrm{data}}(\mathrm{X})}{\epsilon_i^{\mathrm{MC}}(\mathrm{X})}, \tag{21}$$

where $\epsilon_i(X)$ denotes the efficiency for a particular quality selection i (isolation, trigger etc.) calculated as a function of kinematic variables X (p_{T}, η, $\Sigma E_{\mathrm{T}}^{\mathrm{FCal}}$). SF can be calculated for different effects such as detector inactive areas, lepton momentum resolution, efficiency of lepton identification and alike.

Equation 22 describes the weighting method for calculating the final correction factor C_Z from simulation:

$$C_Z(p_{\mathrm{T}}^Z, y^Z) \rightarrow C_Z(p_{\mathrm{T}}^Z, y^Z) \times \Pi_i \mathrm{SF}_i(\mathrm{X}), \tag{22}$$

where the product is taken by multiplying SFs of all individual efficiencies that are relevant for the analysis in a particular Z boson decay channel, such as reconstruction, identification, trigger, isolation, etc. Specifically, one can write:

$$\mathrm{SF}_{\mathrm{total}} = \mathrm{SF}_{\mathrm{reco}} \times \mathrm{SF}_{\mathrm{id}} \times \mathrm{SF}_{\mathrm{iso}} \times \mathrm{SF}_{\mathrm{trig}}. \tag{23}$$

The factorization holds since the individual SFs are very close to unity ($|\mathrm{SF}-1| << 1$) and they are subsequently defined with respect to other requirements, e.g. isolation efficiency is measured for reconstructed and identified leptons, the trigger efficiency is further measured for identified and isolated leptons, etc.

5.6 Scale factor measurement

Scale factors are measured using the tag-and-probe (TnP) method [124], a well-established data-driven procedure of evaluating detector performance by using the information redundancy of various subsystems. The method selects a sample of high-purity leptons coming from a resonance decay (in this case a Z boson) by applying strict selection on one of the decay products (*tag*) and on the invariant mass of the pair involving this lepton and the second particle (*probe*) traced from only a part of the detector. This ensures that the probe is also a lepton, even without identifying it as such in the detector. This opens the possibility of measuring the properties of the selected probe in all subsystems of the detector by changing the definition of the probe particle. An example is shown in Figure 23 wl

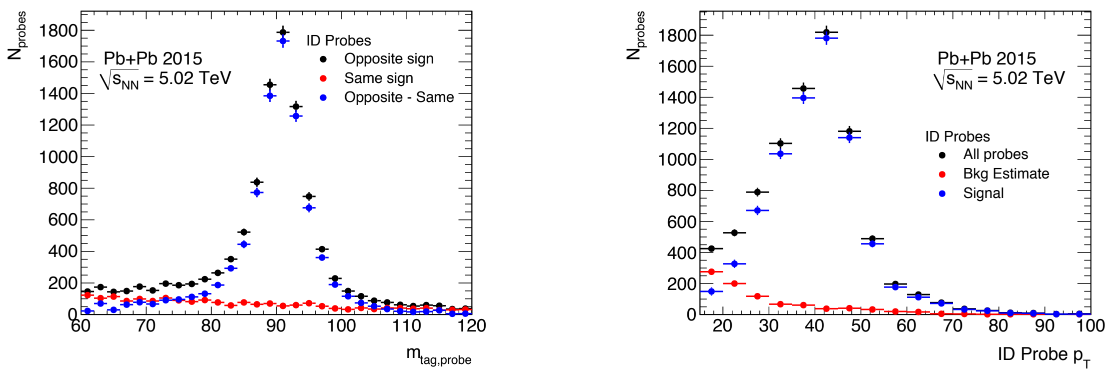

Figure 23: (*Left*) The invariant mass of the TnP muon pairs used for the reconstruction efficiency measurement (black markers). The same-sign pairs are shown in red markers and correspond to the background estimate. (*Right*) The p_{T} distribution of the probes, as well as the background estimate composed of probes with the same charge as the tags and their difference taken as signal probes.

By applying conservative selection criteria on the quality of the tag and the properties of the resonance decay, one can reach a high purity of the probe particle sample. Since the TnP method can be applied independently to data and simulation, the resulting efficiencies can be used to construct the scale factors already defined in Equation 21. Uncertainties on the SFs are worked out by varying the selection requirements on the tag and the pair selection (such as quality requirements on the tag and the invariant mass of the pair), and by varying the background estimates where their contribution is significant.

A general approach for measuring the efficiency of a particular lepton selection is given by:

$$\epsilon_i = \frac{N^{\text{pass}} - N^{\text{pass}}_{\text{bkg}}}{N^{\text{pass}} - N^{\text{pass}}_{\text{bkg}} + N^{\text{fail}} - N^{\text{fail}}_{\text{bkg}}}, \tag{24}$$

where i stands for reco, ID, isolation or trigger requirement, N^{pass} (N^{fail}) is the number of probes that pass (fail) a specific requirement and $N^{\text{pass}}_{\text{bkg}}$ ($N^{\text{fail}}_{\text{bkg}}$) is the number of background probes that pass (fail) the same requirement. This method was used in deriving all the efficiencies and scale factors relevant to the analyses in both systems and both lepton decay channels for the Z measurement. The next two sections describe particular cases of such measurements for muons and electrons in both collision systems.

5.6.1 SF in the muon channel

The muon reconstruction efficiency measurement consists of two stages: first, the efficiency of medium muon quality is measured with respect to the reconstructed ID tracks (or CT muons) and then the efficiency of the ID track reconstruction (or CT muons) is measured with respect to MS tracks. The reconstruction efficiency for medium muons is hence given by:

$$\epsilon(\text{medium}) = \epsilon(\text{medium}|\text{ID}) \cdot \epsilon(\text{ID}) = \epsilon(\text{medium}|\text{ID}) \cdot \epsilon(\text{ID}|\text{MS}),$$

where one assumes that the ID track reconstruction efficiency is independent of the MS track reconstruction ($\epsilon(\text{ID})$=$\epsilon(\text{ID}|\text{MS})$). CT muons are used for the $\epsilon(\text{medium})$ measurement instead of ID tracks to reduce the background contribution, while any possible bias in the efficiency measurement introduced by this choice cancels in the SF ratio. These assumptions have been tested in previous ATLAS measurements [124]. Subsequently, isolation and trigger efficiencies are defined with respect to the measured reconstructed and identified medium muons.

5.6.1.1 SF(μ) in the pp system

Reconstruction and identification. The efficiency for different quality selection requirements is measured with the TnP method in $Z \to \mu\mu$ candidate events in both data and MC simulation. Kinematics and quality selections imposed on the tag muon ensure a clean sample for the probe efficiency measurement. Tag is selected with $p_{\mathrm{T}} > 24$ GeV and $|\eta| < 2.5$, required to be of at least medium identification quality and to pass "loose" isolation requirements. In addition, cuts on transverse and longitudinal impact parameters of the tag track are imposed, namely $|z_0| < 10$ mm and $|\frac{d_0}{\sigma(d_0)}| < 3$. Finally, matching to the online trigger element is required to further suppress the background.

For the $\epsilon\,(\mathrm{ID}|\mathrm{MS})$ measurement, a ME track is selected that corresponds to a isolated muon probe and passes $p_{\mathrm{T}} > 10$ GeV and $|\eta| < 2.5$. ID tracks are selected to pass the same kinematic requirements, a set of quality cuts on track impact parameters and on the number of hits in different ID subsystems, together with isolation requirements. The invariant mass of the pair is required to be inside the interval $81 < m_{\mathrm{Tag+Probe}} < 101$ GeV. The matching criteria is imposed on the cone distance $\mathrm{d}R = \sqrt{\Delta\eta^2 + \Delta\phi^2} < 0.05$ between ME and ID tracks for the efficiency measurement. Finally, residual background contributions in the TnP selection are accounted for by subtracting the contribution from combinatorial same-sign pairs which pass the TnP selection criteria. Figure 24 presents the efficiency $\epsilon\,(\mathrm{ID}|\mathrm{MS})$ of the ID track reconstruction algorithms measured with respect to MS track probes. It is measured to be above 99% and constant as a function of both the probe η and p_{T}. The efficiency does not depend on the charge of the probe track. No significant difference between the efficiencies measured in data and MC is observed.

CT muon probes are selected for the $\epsilon\,(\mathrm{medium}|\mathrm{CT})$ measurement with $p_{\mathrm{T}} > 10$ GeV and $|\eta| < 2.5$. They are required to pass "loose" isolation and ID track quality cuts on the number of hits. Additional track impact parameter requirements are also imposed. Matching to the medium muon is performed with the same cone requirement $\Delta R < 0.05$ for the invariant mass window of $81 < m_{\mathrm{Tag+Probe}} < 101$ GeV. The number of same-sign pairs observed for this measurement is negligible. Figures 25 shows the invariant mass distribution of TnP pairs for the medium muon efficiency measurement.

Figure 26 presents the efficiency $\epsilon\,(\mathrm{medium}|\mathrm{CT})$ of the medium muon reconstruction and identification measured with respect to CT probes. The efficiency measured in the $Z \to \mu\mu$ MC sample and in data is above 99% and constant as a function of both the

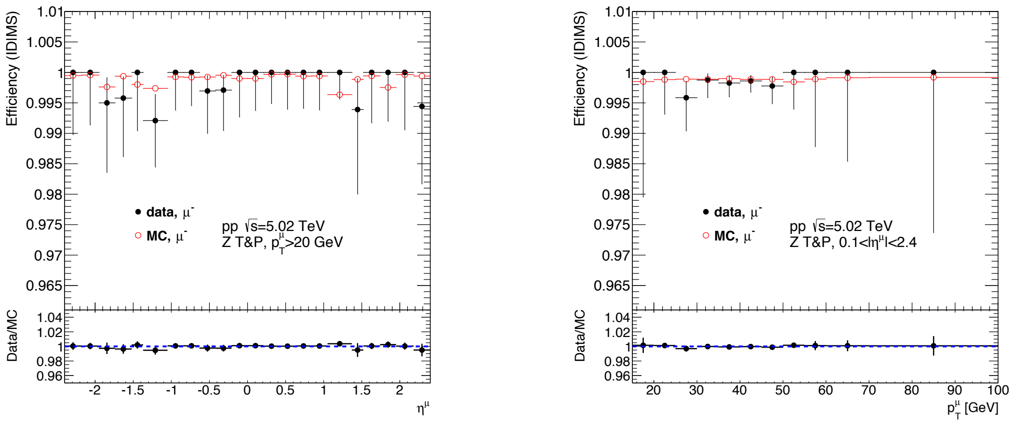

Figure 24: The efficiency of reconstructing ID tracks given the MS track probes as a function of the probe η (*left*) and p_{T} (*right*) shown for negative charges. The ratio of efficiencies measured in data and simulation is shown in the lower panels.

probe η and p_{T}. Small differences at the level of 1–2% are observed between the efficiencies measured in data and MC.

The total efficiency of the medium muon reconstruction and identification algorithms is obtained as $\epsilon\,(\mathrm{medium}) = \epsilon\,(\mathrm{medium|CT}) \cdot \epsilon\,(\mathrm{ID|MS})$ and presented in Figure 27. The differences of efficiencies measured in data and simulation are translated into scale factors defined as $\mathrm{SF}\,(\mathrm{medium}) = \epsilon_{\mathrm{data}}\,(\mathrm{medium})\,/\epsilon_{\mathrm{MC}}\,(\mathrm{medium})$.

Systematic uncertainties considered for the medium muon efficiency are estimated by varying the background contribution (by 0.5 to 2), varying the probe matching cone size and by taking into account the difference between TnP and truth level efficiency. The average systematic uncertainty over muon η is about 0.1%.

Trigger. For the trigger efficiency measurement, both the tag and the probe muon are required to pass medium identification and are selected in the kinematic region of $p_{\mathrm{T}} > 24$ GeV and $|\eta| < 2.4$. Track impact parameter variables for TnP candidates are required to pass $|z_0| < 10$ mm and $|\frac{d_0}{\sigma(d_0)}| < 3$. Matching to the trigger element is imposed only on the tag muon.

The measurement of the trigger efficiency is performed using opposite-sign TnP pairs while same-sign pairs are used for a background estimate. The measurements of the combined HLT and L1 trigger efficiency as a function of the muon η is presented in Figure 28 for data and MC simulation. In data, the trigger efficiency is measured to

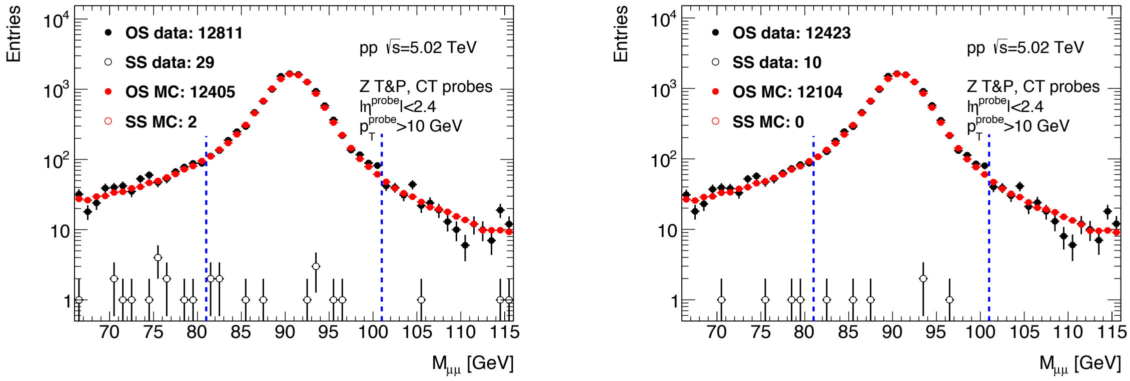

Figure 25: The invariant masses of TnP muon pairs used in the $\epsilon\,(\text{medium}|\text{CT})$ efficiency measurement. Distributions are presented for the efficiency denominator (*left*) and numerator (*right*). Both the opposite-sign and same-sign pairs are shown and the MC distributions are normalized to the number of counts in data.

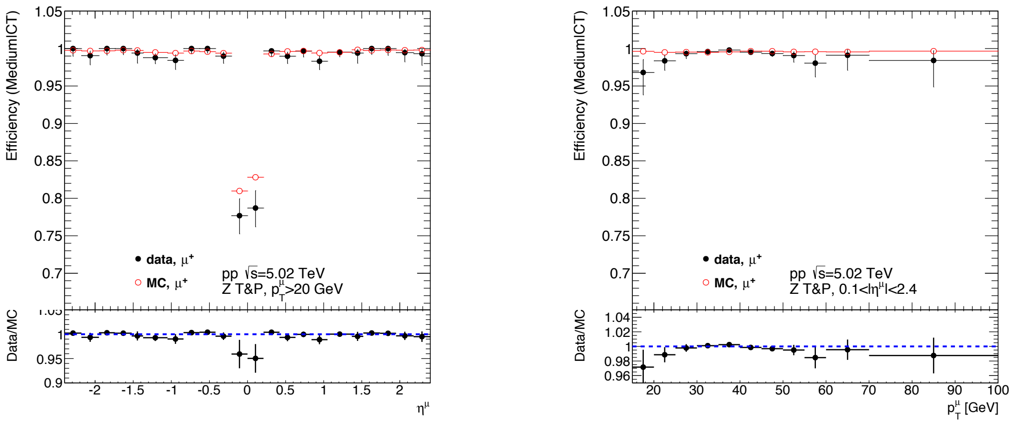

Figure 26: The efficiency of reconstructing and identifying medium quality muons with respect to CT probes as a function of the probe η (*left*) and p_{T} (*right*) shown for positive charges. The ratio of efficiencies measured in data and simulation is shown in the lower panels.

be around 75% in the barrel region ($|\eta| < 1.05$) and around 90% in the endcap region ($1.05 < |\eta| < 2.4$) of the detector. This large difference can be attributed to different acceptance of the L1 trigger systems used in these two regions.

The trigger efficiency measured in simulation agrees with the efficiency measured in data in the endcap region. However, in the barrel region, it is 5–10% higher in simula-

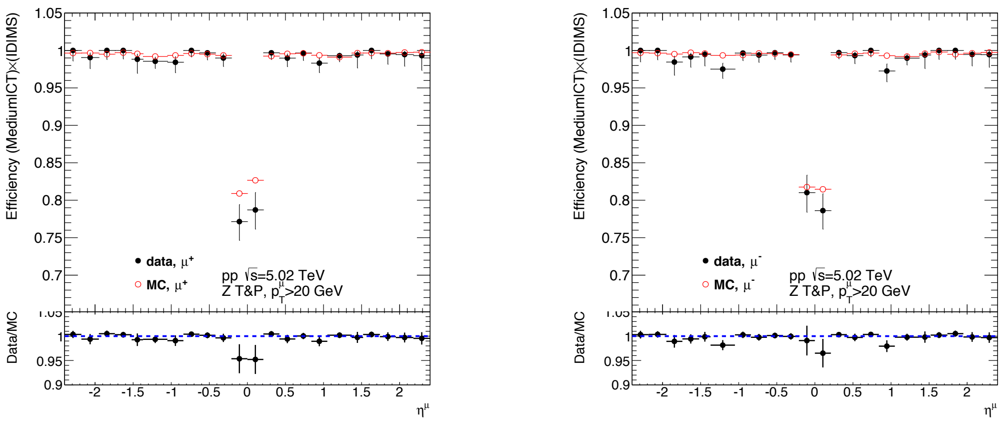

Figure 27: The total efficiency of reconstructing and identifying medium muons as a function of the muon η for positive (*left*) and negative (*right*) muons. The ratio of efficiencies measured in data and simulation is shown in the lower panels.

tion compared to data. This is corrected for by introducing scale factors for the trigger efficiency calculated as defined by Equation 21 and measured as a function of muon η. Figure 28 in the left panel shows the trigger efficiency measured in data and simulation in the upper panel and SFs in the lower panel as a function of muon η.

Systematic uncertainties for the trigger efficiency measurement are estimated by varying the mass range for the invariant mass of the pair, varying the matching cone size and the background contribution and finally by introducing a cut on the azimuthal correlation between a tag and a probe muon ($\Delta\phi_{\text{tag, probe}} < \phi - 0.1$) to account for any measurement bias. An average systematic uncertainty yields 1.2% for this measurement.

Isolation. The selection of the TnP event sample for the isolation efficiency measurement is very similar to the one for the muon trigger efficiency measurement. Opposite-sign dimuon pairs are used to calculate the isolation efficiency, while same-sign pairs are used to estimate background. This contribution is found to be negligible.

The measurements of the *FixedCutTight* isolation efficiency as a function of the probe muon η are presented in the right panel of Figure 28 for TnP candidate events selected in data and simulation. In the simulation, the measured efficiency is constant at 97.5% in the barrel region ($|\eta| < 1.05$) and varies between 96.5% and 98.5% in the endcap region ($1.05 < |\eta| < 2.4$) of the detector. The efficiency measured in data is lower by 2–3% in $|\eta| < 0.6$ and higher by 2–3% in $1.74 < |\eta| < 2.4$. This difference comes from the

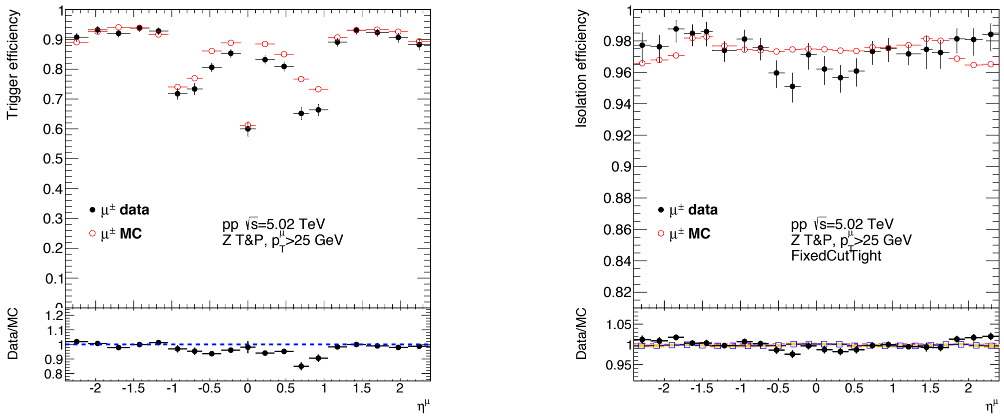

Figure 28: (*Left*) The efficiency of the single-muon trigger HLT_mu14 measured as a function of muon η in data and simulation. (*Right*) The efficiency of the isolation selection *FixedCutTight* measured as a function of muon η in data and simulation. The bottom panels present SFs from this measurement (black markers) and from 13 TeV studies (open blue markers).

mismodeling of the calorimetric isolation in the simulation. In order to correct for this discrepancy, scale factors for the isolation selection efficiency are introduced as a function of muon η, presented in the right panel of Figure 28. They are compared to 13 TeV scale factors which are constant as a function of η, not deviating significantly from unity.

Systematic uncertainties for the isolation efficiency measurement are estimated by varying the mass range for the invariant mass of the pair, varying the minimal distance between a tag and a probe candidate, varying the distance between a probe and the closest jet and finally by varying the background contribution. This yields a contribution of about 0.3% averaged over muon η.

5.6.1.2 SF(μ) in the Pb+Pb system

TnP measurements in the Pb+Pb system are similar to the ones described for the *pp* system above, with the main difference being the abundance of background events due to a larger UE event and bigger detector occupancy. The tag is selected in the kinematic region defined with $p_{\mathrm{T}} > 25$ GeV ($p_{\mathrm{T}} > 30$ GeV) and $|\eta| < 2.5$ for ID (medium) efficiency measurement. It is required to be a *tight* quality muon that matches the online trigger element. Different requirements are imposed on muon probes in order to measure the medium muon reconstruction efficiency and ID reconstruction efficiency, as described below.

SF(medium|ID). ID probes are used as a baseline to study the efficiency of medium muon reconstruction efficiency. To select a clean sample of muons reconstructed as ID tracks, the probes must combine with the tag to have an invariant mass of $81 < m_{\mu\mu} < 101$ GeV and have opposite charges. The invariant mass distribution of TnP pairs is shown on the left side of Figure 23. Even with this selection, the ID probes still have a significant combinatorial background which is estimated by the same sign TnP pairs. The background rises towards lower muon $p_{\rm T}$ as shown on the right side of Figure 23.

The medium muon reconstruction efficiency is defined as the ratio of the number of ID probes which are matched to a medium quality muon to the total number of ID probes. The combinatorial background is subtracted from both the numerator and denominator in order to calculate the efficiency. A systematic uncertainty estimated by varying the background by 15% around the number of same charge probes is assigned to this subtraction procedure. The efficiency is calculated with the background subtraction as a function of $p_{\rm T}$ and η, and event $\Sigma E_{\rm T}^{\rm FCal}$ and is shown in Figure 29 also without background subtraction for control.

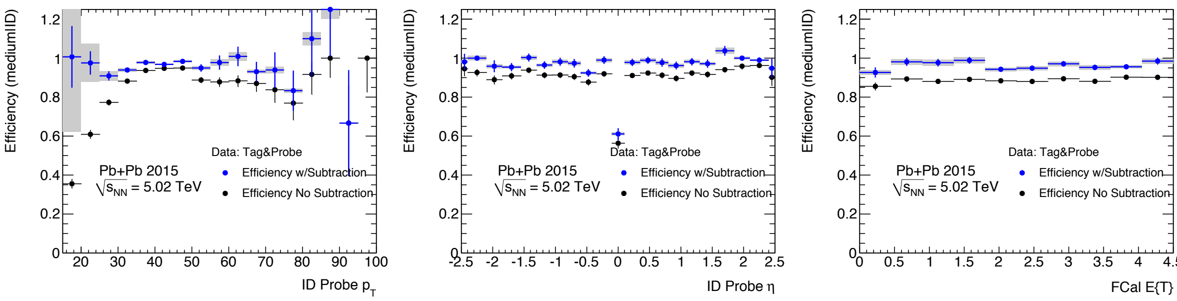

Figure 29: The efficiency to reconstruct a medium quality muon given an ID track as a function of ID probe $p_{\rm T}$ (*left*), ID probe η (*middle*), and event $\Sigma E_{\rm T}^{\rm FCal}$ (*right*). A biased efficiency contaminated by the presence of combinatorial background in the ID probes is also shown.

The same procedure is applied to the MC simulation sample and the SF are obtained according to 21. Due to the background subtraction, the efficiency can exceed one, which occurs in a few points in the analysis of the data. In such case, the SF is taken to be unity. The SF for ϵ(medium|ID) plotted in Figure 30 do not strongly depend on p_{T} or the event $\Sigma E_{\mathrm{T}}^{\mathrm{FCal}}$, but they are sensitive to η.

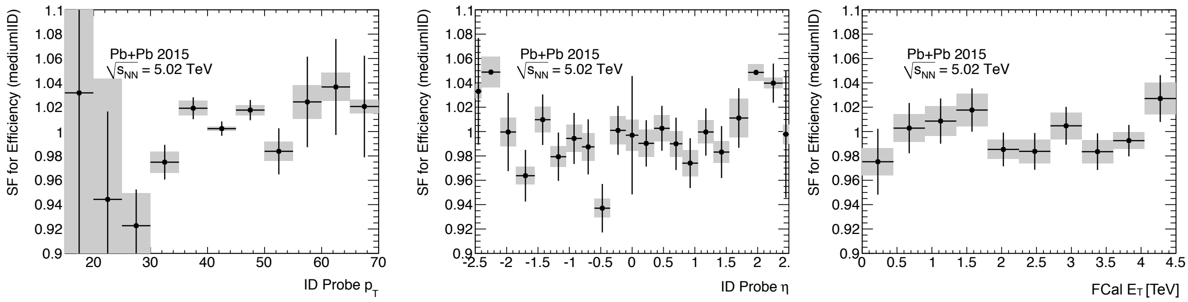

Figure 30: The scale factors for ϵ(medium|ID) as a function of ID probe p_{T} (*left*), ID probe η (*middle*), and event $\Sigma E_{\mathrm{T}}^{\mathrm{FCal}}$ (*right*).

SF(ID|MS). The ME tracks are used as probes to study the performance of the ID tracking for muons. The sample of MS probes is much cleaner than ID probes, and the only requirement on the MS track to be a probe is imposed on the transverse impact parameter, d_0 significance < 3. As in the ID probe sample, the MS probe must have the opposite charge of the tag and pair with it for an invariant mass of $81 < m_{\mu\mu} < 101$ GeV.

The probes are used to study the efficiency of the ID tracking for muons and so the efficiency is defined as the number of MS probes that are matched to an ID track divided by all MS probes. A match to an ID track is defined with dR <0.05. The same subtraction procedure as used in the ID probe analysis is applied for the MS probe analysis as well. Figure 31 shows the final scale factor calculated from the efficiencies measured in the data and the MC.

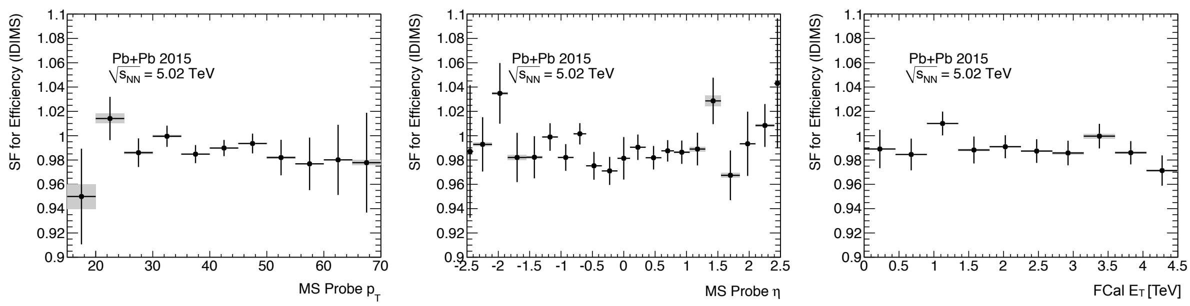

Figure 31: The scale factors for the efficiency of the ID measured with MS tracks as a function of MS probe p_{T} (*left*), MS probe η (*middle*), and event $\Sigma E_{\mathrm{T}}^{\mathrm{FCal}}$ (*right*).

Combined SF. It follows from equation 5.6.1, that the total scale factor which should be used to correct the simulation is the product of the scale factors for ϵ (medium|ID) and ϵ (ID|MS). For the purpose of calculating the total scale factor, the kinematic quantities of the muons measured by the ID probes and MS probes are considered to be compatible. The total scale factor is shown in Figure 32. There is no significant dependence of the

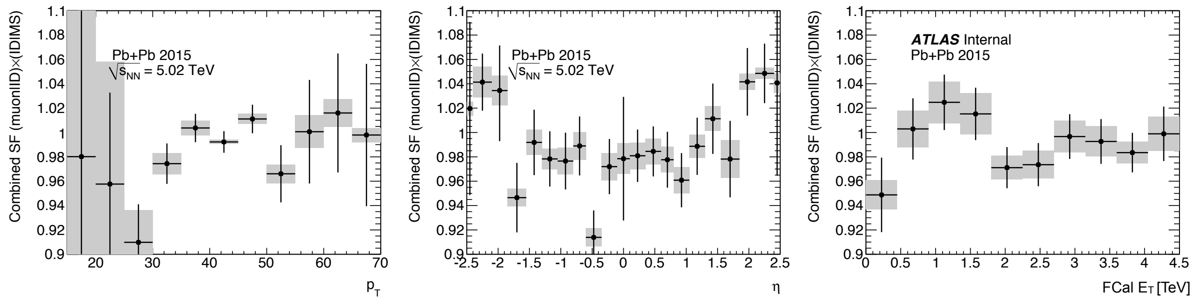

Figure 32: The product of the scale factors for ϵ(medium|ID) and ϵ(ID|MS) as a function of the probe p_{T} (*left*), the probe η (*middle*), and event $\Sigma E_{\mathrm{T}}^{\mathrm{FCal}}$ (*right*).

total scale factor on the muon p_{T} or event $\Sigma E_{\mathrm{T}}^{\mathrm{FCal}}$. There does appear to be a difference between forward and midrapidity in the distribution of muon η. The final scale factor in the analysis was therefore evaluated in three η bins as: 1.04 ± 0.02 for $\eta < -1.8$, 0.97 ± 0.01, and 1.04 ± 0.02 for $\eta > 1.8$.

5.6.2 SF in the electron channel

The SF and the efficiency for the electron channel measurement are factorized according to Equation 23. In the case of the *pp* measurement, the total efficiency $\epsilon_{\mathrm{total}}$ is calculated as:

$$\epsilon_{\mathrm{total}} \quad = \quad \epsilon_{\mathrm{EMclus}} \times \epsilon_{\mathrm{reco}} \times \epsilon_{\mathrm{id}} \times \epsilon_{\mathrm{iso}} \times \epsilon_{\mathrm{trig}},$$

where the first term, $\epsilon_{\mathrm{EMclus}}$, is the efficiency to reconstruct the electromagnetic cluster candidates and is evaluated entirely from the simulation. Subsequent terms are efficiencies for applying tighter requirements on electrons - starting from a reconstructed electron with the minimum track quality requirements (ϵ_{reco}) to an identified electron with the likelihood-based quality definitions (ϵ_{id}), to the isolation requirement by restricting the amount of energy around the electron and therefore suppressing the jet background contribution (ϵ_{iso}). The last term, (ϵ_{trig}), is a requirement on the trigger efficiency after all the selections have been made. Similarly, in the Pb+Pb system, the reduced efficiency has been measured due to specific analysis requirements applied, that is:

$$\epsilon_{\text{total}} = \epsilon_{\text{EMclus}} \times \epsilon_{\text{id}} \times \epsilon_{\text{trig}},$$

where the first term, ϵ_{EMclus}, is evaluated entirely from the simulation as in the *pp* case and subsequent terms are measured in data and simulation. From the calculated efficiencies, a set of electron SFs is derived according to Equation 21 to improve agreement between data and simulation.

5.6.2.1 SF(e) in the *pp* system

Reconstruction efficiency. The electron reconstruction efficiency is defined as a fraction of all electromagnetic clusters (effectively all reconstructed electrons and photons) that match the inner detector track. The inefficiency of the electron reconstruction is manifested in reconstructing an electron as a photon which is usually at the level of $\sim 1\%$. The background for this measurement consists of the multi-jet contribution and the falling photon spectrum (in the denominator). Electrons are considered reconstructed if they pass a loose track requirement imposed on the number of silicon hits in the detector. Explicitly,

$$\epsilon_{\text{reco}} = \frac{N^{\text{pass}} - N^{\text{pass}}_{\text{bkg}}}{N^{\text{pass}} - N^{\text{pass}}_{\text{bkg}} + N^{\text{fail}} - N^{\text{fail}}_{\text{bkg}} + N^{\text{photon}} - N^{\text{fit}}},$$

where N^{pass} and N^{fail} are the numbers of electrons passing or failing the minimal track requirement ($N_{\text{Pix}} > 1, N_{\text{SCT}} > 7$ for pixel and SCT hits) respectively. $N^{\text{pass}}_{\text{bkg}}$ and $N^{\text{fail}}_{\text{bkg}}$ are the numbers of the passed (failed) electrons in the background template, N^{photon} is the number of photons and the N_{fit} is the number of estimated background photons.

The tag cluster has tighter quality requirements and a transverse momentum cut of $p_{\text{T}} > 20$ GeV being matched to a trigger element. Probes are required to be classified as reconstructed electrons or photons, with $p_{\text{T}} > 15$ GeV and finally a veto for the probes being inside of an energetic 0.4 cone jet with $E^{\text{jet}}_{\text{T}} > 20$ GeV is imposed. Converted photons are also excluded from the measurement. The mass distribution of TnP candidates is shown in Fig 33 for the denominator (*left*) and numerator (*right*).

Background subtraction is performed independently in the numerator and the denominator from the data-driven templates requiring poorly identified and anti-isolated

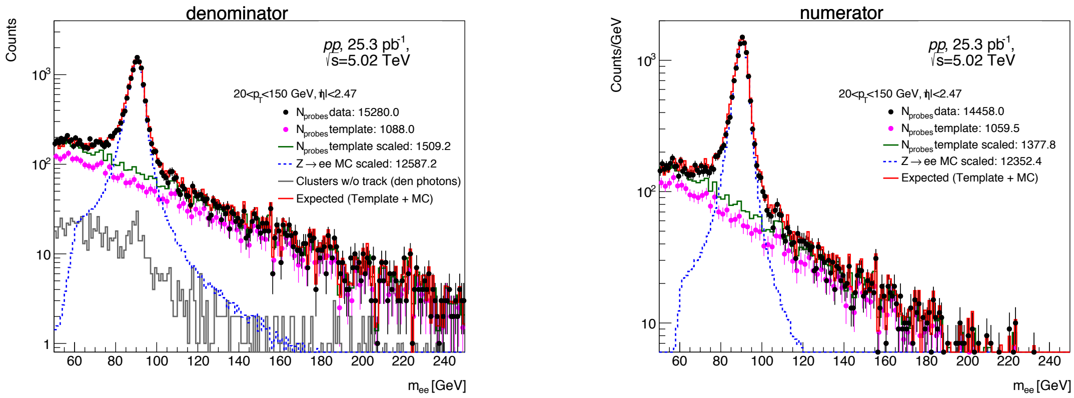

Figure 33: TnP invariant mass distributions for all probes (*left*) and reconstructed electron probes (*right*) shown for data (black points), data-driven background template (magenta markers), template scaled to the high-mass tail (green line), MC prediction scaled to data luminosity (dashed blue line) and total template+MC prediction (red).

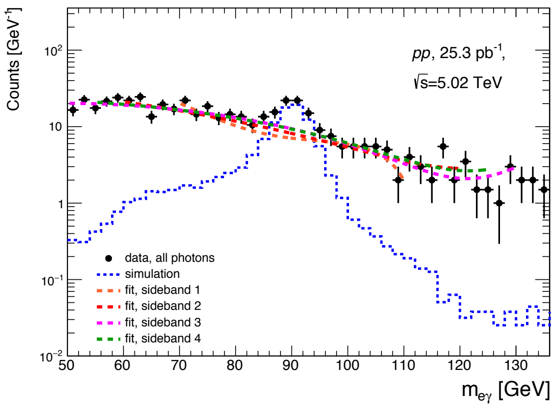

Figure 34: TnP invariant mass distributions where probes are required to be reconstructed only as photons. Data points are shown in black markers, signal MC is shown in dashed blue line and different side-band fits are shown in colors as indicated in the panel.

electrons. The denominator term N^{photon}, which consists only from photons passing the probe requirements, is estimated by subtracting the background N^{fit} obtained by a side-band fit away from the signal region. This fit was obtained after integrating over different p_{T} and η bins as shown in Figure 34. A polynomial of the third order is used as a fit model and was found to converge well. The number of background photons obtained in different side-bands is used to obtain measurement systematics. To determine kinematic distributions of the background-subtracted photons, a data-driven method was used. The results of the fit were used to normalize kinematic distributions obtained from the 13 TeV 2015/2016 data.

Systematic variations used for the measurement consist of varying the tag quality requirement, the pair mass and the background estimates. The example of results for two p_{T} bins is shown in Figure 35. The upper panel of each figure shows the efficiencies in the MC and the data versus the electron pseudorapidity for a specific range of the electron momentum and in the lower panel is the comparison of the scale factors between 13 TeV data set (red markers) and the 5 TeV data set (black markers). The blue bands are showing the systematic uncertainties on the 5 TeV measurement and the back bars are just the statistical uncertainty.

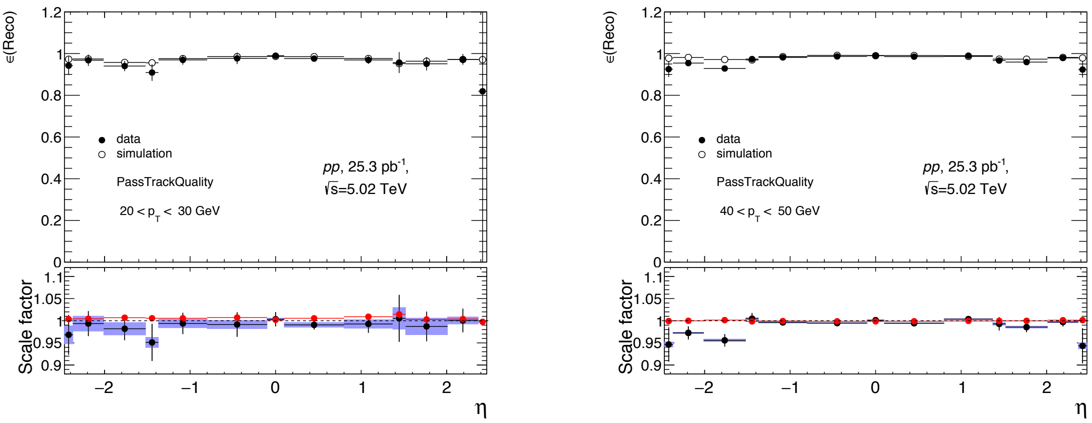

Figure 35: Each figure shows the electron reconstruction efficiency in data (full markers) and simulation (open markers) in the upper panel and the SFs (black markers) in the lower panel versus electron η. The two figures correspond to a specific range of the probe electron p_{T} as indicated in the upper panel. The statistical uncertainties are shown as bars and the systematics as blue bands in the lower panel. Red markers in the lower panel correspond to SF values for the same measurement performed in 13 TeV pp data for comparison.

Identification. Electron identification (ID) efficiency is defined as the fraction of reconstructed electrons passing the medium working point. Probes in this measurement are all reconstructed electrons that pass a minimal track quality requirement explained above. All tag and probe electron candidates are required to be inside the EMCal precision region of $|\eta| < 2.47$ and to pass additional object quality requirements ("isGoodOQ").

The tag electron is required to pass tighter quality requirements, to be match to a trigger element and has a transverse momentum cut of $p_{\mathrm{T}} > 20$ GeV. The tag also needs to satisfy the track isolation requirement of ptcone20/$p_{\mathrm{T}} < 0.1$. Probes are required to pass the cut of $p_{\mathrm{T}} > 4.5$ GeV and finally a veto for the probes being inside of an energetic 0.4 cone jet with $E_{\mathrm{T}}^{\mathrm{jet}} > 20$ GeV is imposed. The results are shown in Fig 36. The upper panel of each figure shows the efficiencies in the MC and the data versus the electron pseudorapidity for a specific range of the electron momentum and in the lower panel is the comparison of the scale factors between 13 TeV data set (blue markers) and the 5 TeV data set (black markers). The orange bands are showing the systematic uncertainties on the 5 TeV measurement and the black bars are just the statistical uncertainty.

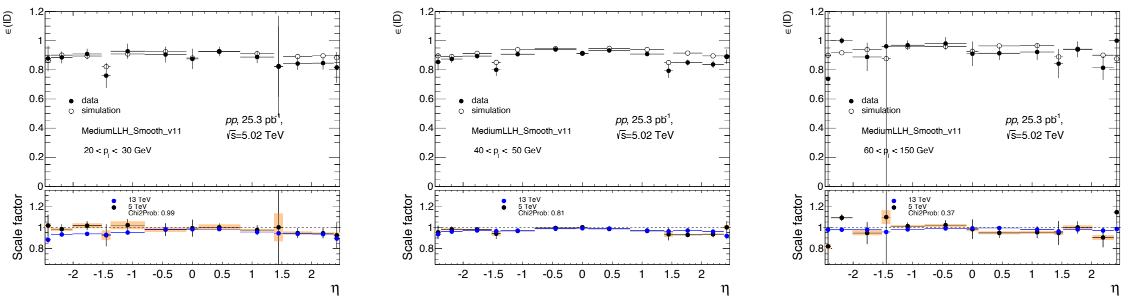

Figure 36: Each figure shows the electron ID efficiency in data (full markers) and simulation (open markers) in the upper panel and the SFs in 13 TeV (blue markers) and 5 TeV data sets (black markers) in the lower panel versus electron η. Each figure corresponds to a specific range of the electron p_{T} indicated in the upper panel. The points where the statistical uncertainty is very large corresponds to points with very low statistics. The statistical uncertainties are shown as bars and the systematics as orange bands in the lower panel.

Isolation and trigger. An analogous procedure was applied in measuring the electron isolation and trigger efficiencies and scale factors. Isolation *FixedCutTight* efficiency is defined as the fraction of medium LH identified electrons passing the isolation working point requirements. The trigger efficiency is defined as a fraction of all the LH medium isolated electrons that match the trigger element of the event trigger "HLT_e15_lhloose_L1EM13VH". Results for the isolation measurements are shown in Figure 37 and for the trigger measurements in Figure 38.

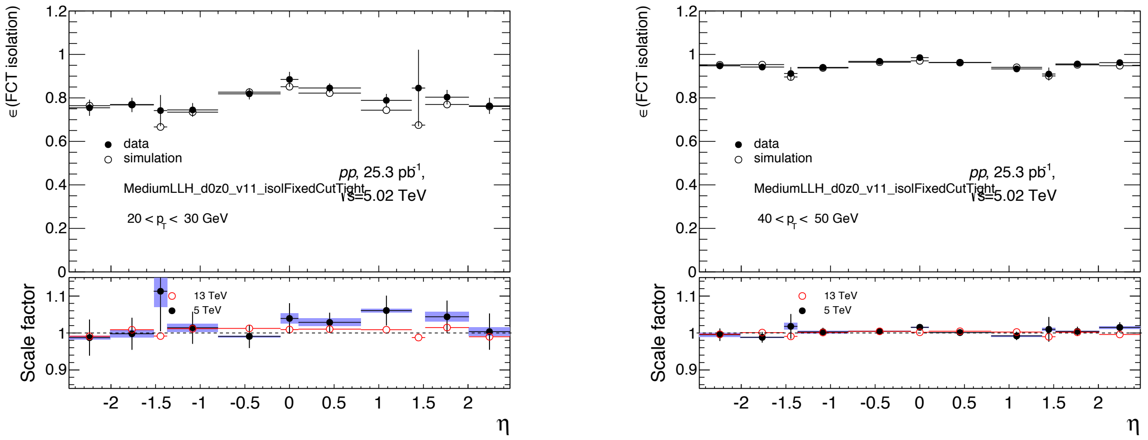

Figure 37: Each figure shows the electron isolation efficiency in data (full markers) and simulation (open markers) in the upper panel and the SFs in 13 TeV (red markers) and 5 TeV data sets (black markers) in the lower panel as a function of the probe η. Each figure corresponds to a specific range of the electron p_{T} indicated in the upper panel. The points where the statistical uncertainty is very large corresponds to points with very low statistics. The statistical uncertainties are shown as bars and the systematics as blue bands in the lower panel.

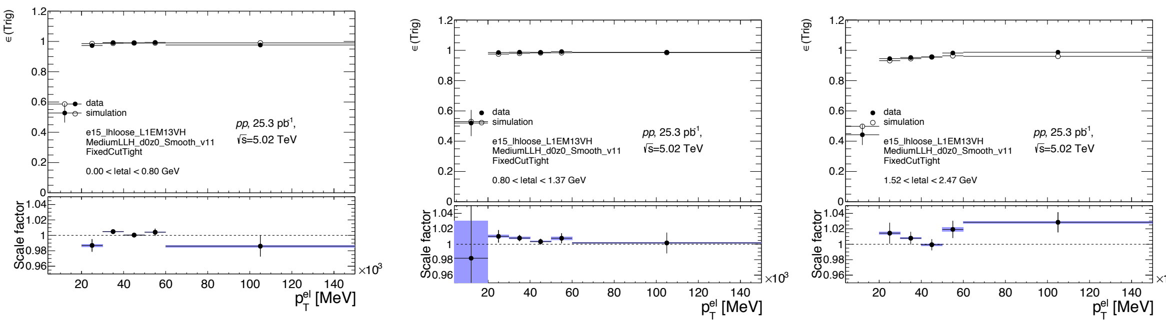

Figure 38: The upper panel in each of the figures shows the trigger efficiency measured in data (full markers) and simulation (open markers) and the lower panel shows the measured trigger SF. Each figure corresponds to a specific η region indicated on the upper panel. Uncertainties on the efficiency measurements are statistical only whereas the uncertainties on the SF are represented separately as statistical (bars) and systematic (blue bands).

5.6.2.2 SF(e) in the Pb+Pb system

Similarly, as in the pp sample, a clean sample of TnP electron pairs from the Z decays was selected by applying a set of event selection cuts, cuts on the tag and finally on the tag-and-probe pair. Tag electron is required to have $pt > 25$ GeV and $|\eta| < 2.47$ and to satisfy LH loose identification quality. An additional isolation requirement is further imposed on tags to suppress the background, namely $p_{\mathrm{T}}\mathrm{cone}20/2p_{\mathrm{T}} < 0.05\Sigma E_{\mathrm{T}}^{\mathrm{FCal}}+0.025$.

Probes are selected as all reconstructed EM clusters by selecting the clusters with author=1 (electron), author=16 (ambiguous) from the reconstructed electron container and only the photon clusters from the container of reconstructed photons. This is to ensure no double counting of EM clusters since those with author 16 are duplicated both in the electron and the photon container. Further, they are required to pass the cuts: $p_{\mathrm{T}}^{\mathrm{clus}} > 15$ GeV and $|\eta^{\mathrm{clus}}| < 1.37$ or $1.52 < |\eta^{\mathrm{clus}}| < 2.47$ so to be in the precision region of the calorimeter. “Loose” electron track requirements are applied for the probes passing the ID requirement (efficiency numerator) for the number of pixel and silicon hits, $N_{\mathrm{Pix}} > 2$ and $N_{\mathrm{SCT}} > 7$.

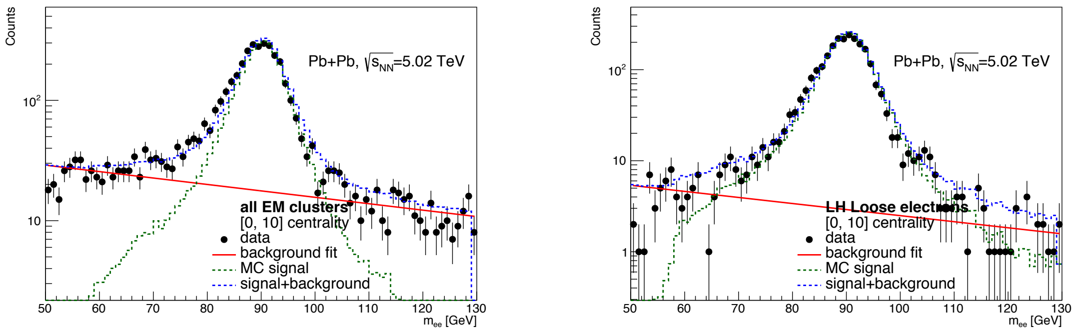

Figure 39: Number of signal TnP pairs (black markers) for denominator (*left*) and numerator (*right*) in the 0–10% centrality bin. Green dashed curve shows the MC prediction normalized to data and the red line shows the background fit obtained outside of the signal region in two sidebands (for details see text). The total prediction is shown with the blue dashed curve.

The signal region for the measurement in different kinematic bins is determined by the invariant mass range of TnP pairs. The default signal region is taken to be $80 < m_{\mathrm{pair}} < 100$ GeV. The background subtraction is done by fitting an exponential in two mass sidebands: [50, 75] U [115, 130] GeV, both for the numerator and the denominator. The efficiency is calculated as:

$$\epsilon = \frac{N^{\text{pass}} - N^{\text{pass}}_{\text{bkg}}}{N^{\text{clus}} - N^{\text{clus}}_{\text{bkg}}},$$

where N^{pass} is the number of electrons passing the identification requirement, N^{clus} is the number of reconstructed EM clusters and $N^{\text{pass, clus}}_{\text{bkg}}$ is the number of background candidates obtained with a fit procedure both in the numerator and the denominator. Figure 39 shows the denominator (*left*) and the numerator (*right*) TnP pairs from data (black markers) integrated over p_{T} and η in one centrality bin 0–10%. The green dashed line denotes the signal MC simulation which is normalized to the data by the ratio of a very clean sample of tight electrons. The background estimate is shown as the exponential fit (red line) which is obtained by fitting the sideband regions. The total prediction of the MC signal and the background estimate is shown in the blue dashed line and it is found to agree with the data yields.

Different variations to the tag quality, sideband ranges and the signal pair mass were applied in order to derive the systematic uncertainty for the efficiency and the scale factor measurement. The scale factor was calculated as a ratio of the efficiency between the data and the simulation in each kinematic bin of p_{T}, η and $\Sigma E_{\text{T}}^{\text{FCal}}$. After applying all the variations, the final SF was calculated as the mean value over all the systematic variations and the systematic uncertainty is obtained by calculating the RMS over all the variations. Statistical uncertainty on the final SF is calculated as an average over all the statistical uncertainties in different variations.

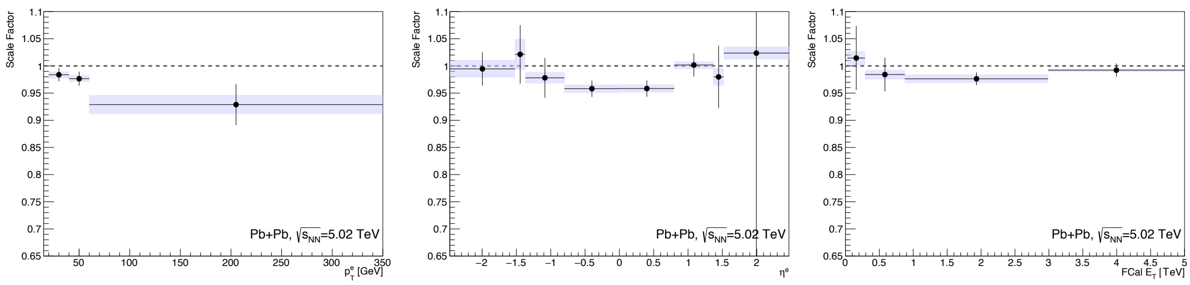

Figure 40: The final electron reconstruction SF as a function of the probe p_{T} (*left*), η (*middle*) and $\Sigma E_{\text{T}}^{\text{FCal}}$ in the event (*right*). Black markers with lines represent results with the corresponding statistical uncertainty and the grey boxes represent systematic uncertainty.

The final scale factor and with corresponding statistical and systematic uncertainties is given in Figure 40 with respect to probe p_{T}, η and the $E_{\mathrm{T}}^{\mathrm{FCal}}$. Uncorrelated uncertainty is on the level of 2-5% per bin and the correlated uncertainty obtained with systematic variations is on the level of 1-2% per bin. The results show no significant dependence of the SF on the centrality of the event ($E_{\mathrm{T}}^{\mathrm{FCal}}$) or the probe p_{T}, but there is a significant shape dependence in η where SF values reach up to 5% away from unity in the barrel. A better agreement between the channels was observed after applying the SF(η) in the analysis.

5.7 Systematic uncertainties

Here we discuss the main sources of systematic uncertainties for the measurement of the Z boson production in *pp* and Pb+Pb collision systems separately for the muon and the electron decay channel. The dominant uncertainty sources in both systems are related to lepton selection efficiency measurements and the corresponding scale factors. Further sources are coming from the background subtraction procedures employed in each measurement. Finally, factors such as luminosity in the *pp* measurement and the $\langle T_{\mathrm{AA}} \rangle$ arising from the Glauber modeling introduce an overall scaling uncertainty as discussed below.

5.7.1 Uncertainties in the *pp* measurement

The main source of the measurement uncertainty in both muon and electron channel are uncertainties in the determination of lepton trigger, reconstruction, identification and isolation efficiency scale factors. These enter the measurement through correction factors C_Z.

In the muon channel, the statistical components of the scale factor uncertainties are propagated to the measurements via MC pseudo-experiments, while systematic components are propagated as a single variation fully correlated across all muon $|\eta|$ intervals. The largest contribution to systematic uncertainty comes from the muon isolation efficiency measurement and amounts to 0.7%. Uncertainties coming from the muon p_{T} scale and resolution are below 0.2%.

The uncertainties of the electron efficiency measurements are divided into contributions correlated across electron η and p_{T} intervals and uncorrelated ones and are propagated to the cross-section measurement accordingly. The final contribution to systematic uncertainty is 1.3%. Uncertainties in the modeling of the electron charge identification are at the level of 0.1% and neglected for the cross-section measurement. Systematic effects related to the electron p_{T} scale and resolution are subdominant, yielding less than 0.2% uncertainty for the final measurement.

Another uncertainty contribution arises from the background evaluation. Since all individual background contributions are below 0.2% of the selected data sample, the final uncertainty on the fiducial cross section is negligible. Finally, the luminosity measurement uncertainty contributes to the overall scale uncertainty for the final measurement. Luminosity measurements in ATLAS are calibrated using dedicated van der Meer scans [125]. The analysis of data from the scan performed in pp collisions at $\sqrt{s}$ =5.02 TeV, which uses the LUCID-2 detector for the baseline luminosity measurements [126], yields a relative systematic uncertainty of 1.9% in the measured luminosity. The largest sources of uncertainty are systematic effects related to the van der Meer scan procedure and the long-term stability of the luminosity calibration.

The full summary of systematic uncertainty sources for the muon and the electron channel is given in Table 7.

	$Z \to \mu^+\mu^-$	$Z \to e^+e^-$
Trigger efficiency	0.4%	$<$ 0.1%
Reconstruction efficiency	0.4%	0.4%
Identification efficiency	–	1.0%
Isolation efficiency	0.7%	0.6%
Lepton p_{T} resolution	$<$ 0.1%	0.1%
Lepton p_{T} scale	$<$ 0.1%	0.1%
Multi-jet background	$<$ 0.1%	$<$ 0.1%
Electroweak+top background	$<$ 0.1%	$<$ 0.1%

Table 7: Relative uncertainties in the measured integrated cross sections for the muon and the electron channel in the pp measurement integrated over rapidity.

5.7.2 Uncertainties in the Pb+Pb measurement

Uncertainties in the determination of lepton reconstruction and identification efficiency scale factors, as well as the parametrization of the centrality dependence of the total correction, affect the measurements through the correction factors C_Z.

In the muon channel, the scale factors in the three η regions are modified by their errors to derive the corresponding systematic uncertainty of C_Z. Also, the impact of the measured SF dependence of the final C_Z value on the event centrality is evaluated. The total relative uncertainty from these two sources ranges from 3.1% at midrapidity ($|y| < 0.5$) to 4.5% at forward Z boson rapidities and gives a contribution, constant as a function of the event centrality, of ~3.4% for Z boson yields.

The main contribution to the systematic uncertainty in the electron channel comes from the uncertainties in measuring the reconstruction scale factor. Uncertainties related to efficiency are classified as either correlated or uncorrelated and are propagated accordingly to the final measurement uncertainty. The correlated uncertainty component of the SF is obtained by varying the requirements on the tag electron identification and isolation and the invariant mass of the TnP pair. The uncorrelated statistical components of the scale factor uncertainties are propagated to the measurements via MC pseudo-experiments, while the systematic components are propagated as a single variation fully correlated across all electron η intervals. This source gives a 2.5–5% uncertainty as a function of rapidity and around 3% for all centrality intervals.

In both decay channels, the trigger efficiency is derived from the TnP results in the data. The statistical limitation of the measured sample determines the uncertainty associated with trigger correction. Although the uncertainties in each bin are relatively large in the muon trigger efficiency, after propagating this uncertainty to the dimuon efficiency, where only one of the muons is required to fire the trigger, the total uncertainty is quite small, between 0.2% and 0.5% when derived as a function of centrality and 0.1–0.2% when derived as a function of Z boson rapidity. The uncertainty is propagated using MC pseudo-experiments and the uncertainties in the linear fit coefficients of the trigger efficiency as a function of centrality. In the electron channel, this uncertainty is at most 0.5%.

The NLO cross section of the background samples of $Z \to \tau^+\tau^-$ and top-quark production is varied by 10% to derive the corresponding uncertainties [74]. However, in both decay channels, the multi-jet background dominates the uncertainty contribution. In the muon channel, the multi-jet background contribution is varied by 10%, which produces a 0.5% uncertainty in the final Z boson yield. In the electron channel, the multi-jet template normalization is varied by 20%, which corresponds to the level of statistical uncertainty in the number of same-sign candidates in the low-mass control region. The overall contribution to the systematic uncertainty is about 0.5% in rapidity bins and 0.5–2% in centrality bins.

In the 50–100% centrality interval, the uncertainty in subtracting the photon-induced background is evaluated by considering two sources. The first source is the difference between the acoplanarity cut efficiencies for hadronic Z boson production evaluated from data and simulation. An uncertainty of 0.4% accounts for this difference. For the second source, the uncertainty in the background rejection efficiency of the acoplanarity cut is evaluated from the candidates with large rapidity gaps. This uncertainty has two contributions. One is the statistical uncertainty of the event sample with large rapidity gaps, which amounts to 7%. The other contribution is due to the difference between the acoplanarity distributions for electrons and muons, which amounts to about 8%. In the 0–50% centrality interval, where the background subtraction is not performed, an uncertainty of 0.4%, evaluated from the difference between the data and simulation acoplanarity distributions, is introduced to account for a possible residual EM background contribution.

An additional uncertainty of the bin-by-bin correction is due to the correlation parametrization of the rapidity and centrality dependence of C_Z described in Eq. (20) and it stems primarily from the statistical uncertainty of the MC data set. To estimate uncertainties associated with these assumptions the parameters of the function $G(y, \Sigma E_{\mathrm{T}}^{\mathrm{FCal}})$ are varied by the errors of the parameters of the parabolic fit. The data are corrected with these variations, and the difference between these results and the standard correction is taken as an estimate of the systematic uncertainty. In the muon channel, the uncertainty associated with this source ranges from 0.4% to 1.4% in rapidity bins and is constant at $\sim$0.5% as a function of centrality, with the exception of the most peripheral bin where the uncertainty is $\sim$1%. In the electron channel, the uncertainty as a function of the rapidity ranges from 0.4% to 1.6% and is $\sim$1% in centrality bins, whereas in the most peripheral bin this contribution rises to $\sim$2%.

For both channels and the combined result, the uncertainties of the geometric parameters ($\langle T_{\mathrm{AA}} \rangle$ and $\langle N_{\mathrm{part}} \rangle$) listed in Table 1 range from about 1% in central collisions to about 12% in peripheral collisions. They are treated as fully correlated between the channels. Finally, the total uncertainty for the pp measurement [74] used for the R_{AA} calculation is 2.3%. The summary of uncertainty contributions for both decay channels is shown in Figure 41 versus dilepton rapidity.

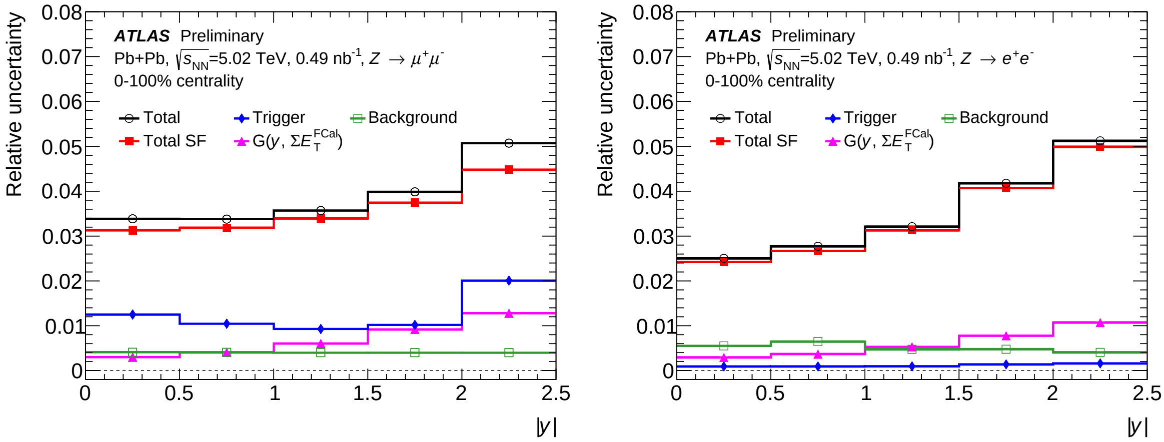

Figure 41: Relative systematic uncertainties in the Pb+Pb measurement for the muon (*left*) and the electron decay channel (*right*) as a function of dilepton rapidity. The total systematic uncertainty containing all independent sources added in quadrature is shown in open black circles.

6 Results

In this chapter, we present the final results of the Z boson production yield measurements in pp and Pb+Pb systems. The measured fiducial Z production cross section in the pp system is discussed in Section 6.1. In Section 6.2 we present the nuclear modification factor measurement obtained from the previously published ATLAS data and the pp cross section measured in this work. Finally, the measured Z boson yield in the Pb+Pb system is presented in Section 6.3 together with the nuclear modification factor R_{AA} obtained for the first time for this type of measurement by using the reference pp result.

6.1 Z-boson cross section in the pp system

Results of the pp measurement in the electron and muon channels are summarized in Table 8. In the table, the statistical uncertainty is defined from the variance of the background-subtracted number of observed events, and the systematic uncertainty includes all of the uncertainty components described above, except for the luminosity uncertainty, which is given separately. The systematic uncertainties coming from lepton efficiency corrections are measured as a function of lepton η and p_{T} and include a significant statistical component due to the number of Z boson events used to derive the corrections. This relative statistical component is substantially reduced for the integrated cross sections compared to the differential ones.

The electron and muon channel measurements are combined using the Best Linear Unbiased Estimate (BLUE) method [127]. Sources of systematic uncertainties corresponding to lepton reconstruction and identification are naturally uncorrelated between electron and muon channel and therefore there is a reduction in the systematic uncertainty for the combined result. The luminosity uncertainty is not taken into account when performing the combination since it is a scaling uncertainty in both channels. The rapidity distributions for the muon channel, electron channel and combined results are shown in Figure 42 and the results are listed in Table 8. The combination yields χ^2/d.o.f$= 3.0/5$ for the Z boson result. Using the same data set and the same set of systematic uncertainty sources, the W boson differential cross sections were also measured in the two lepton decay channels. A simultaneous combination of all measurements, accounting for the correlation of the experimental systematic uncertainties between the W and Z measurement results for a given lepton flavor, gives χ^2/d.o.f $= 37.5/25$, corresponding to a probability of 5.2%. Since the observed trend of the muon channel cross section is that it is systematically higher than the electron channel cross section, the systematic uncertainties are scaled such that χ^2/d.o.f=1; Table 8 reflects this scaling.

After the channel combination, one can construct ratios of fiducial cross sections in which the luminosity uncertainty as well as other correlated uncertainties are eliminated or strongly reduced. The measured ratio of fiducial W^+ and W^- production cross sections, as well as ratios of fiducial $W^\pm$ and Z boson production cross sections, are summarized in Table 9. The precision of these ratio measurements is very high with a total experimental uncertainty of 0.8% for the W^+/W^- ratio and 1.3% for the $W^\pm/Z$ ratio.

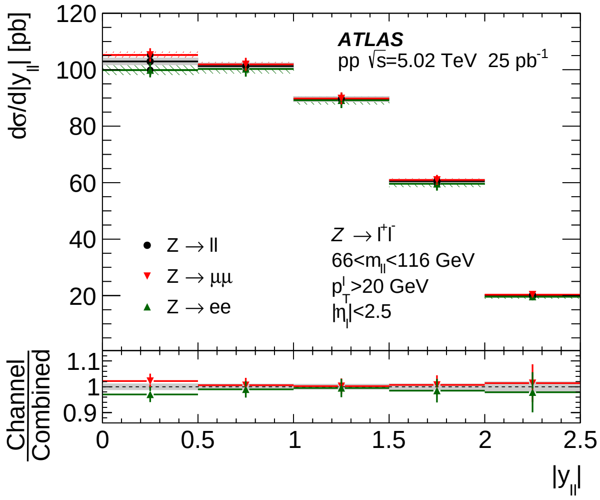

Figure 42: Differential Z boson production cross section as a function of absolute lepton-pair rapidity, for the electron, muon and combined results [74]. Statistical and systematic errors are shown as corresponding bars and shaded bands. The luminosity uncertainty is not included. The lower panel shows the ratio of channels to the combined differential cross section in each bin. In the lower panel, error bars represent statistical uncertainties in the ratio, while the shaded band represents systematic uncertainties in the combined differential cross sections.

$\lvert y_{\ell\ell}\rvert$	$Z \to \mu^+\mu^-$	$Z \to e^+e^-$	$Z \to \ell^+\ell^-$
0.0 – 0.5	$105.2 \pm 2.4 \pm 1.1 \pm 2.0$	$99.9 \pm 2.5 \pm 1.6 \pm 1.9$	$103.0 \pm 1.7 \pm 1.2 \pm 1.9$
0.5 – 1.0	$101.9 \pm 2.3 \pm 1.0 \pm 1.9$	$100.3 \pm 2.7 \pm 1.6 \pm 1.9$	$101.3 \pm 1.8 \pm 1.1 \pm 1.9$
1.0 – 1.5	$89.8 \pm 2.1 \pm 0.8 \pm 1.7$	$89.2 \pm 2.7 \pm 1.4 \pm 1.7$	$89.6 \pm 1.7 \pm 0.9 \pm 1.7$
1.5 – 2.0	$61.0 \pm 1.8 \pm 0.6 \pm 1.1$	$59.6 \pm 2.4 \pm 1.2 \pm 1.1$	$60.5 \pm 1.4 \pm 0.7 \pm 1.1$
2.0 – 2.5	$20.3 \pm 1.2 \pm 0.2 \pm 0.4$	$19.6 \pm 1.3 \pm 0.7 \pm 0.4$	$20.0 \pm 0.9 \pm 0.4 \pm 0.4$
0.0 – 2.5	$377.9 \pm 4.4 \pm 3.4 \pm 7.1$	$369.0 \pm 5.3 \pm 4.7 \pm 6.9$	$374.5 \pm 3.4 \pm 3.6 \pm 7.0$

Table 8: Measured Z boson differential cross section $\mathrm{d}\sigma/\mathrm{d}|y_{\ell\ell}|$ in muon and electron decay channels and the final combined cross section. Values quoted are given in the form: value $\pm$ stat $\pm$ syst $\pm$ lumi in pb.

The measured cross sections are compared with theoretical predictions obtained using a modified version of DYNNLO 1.5 [128, 129] optimized for speed of computation. The calculation is performed at $O(\alpha_S^2)$ in QCD and at leading order in the EW theory, with parameters set according to the G_μ scheme [130]. The input parameters (the Fermi con-

$R^{\text{fid}}_{W^+/Z}$	6.06 ± 0.08 (stat) ± 0.01 (syst)
$R^{\text{fid}}_{W^-/Z}$	3.75 ± 0.05 (stat) ± 0.01 (syst)
$R^{\text{fid}}_{W/Z}$	9.81 ± 0.13 (stat) ± 0.01 (syst)

Table 9: Ratios of integrated W and Z production cross sections [74].

stant G_{F}, the masses and widths of the W and Z bosons, and the CKM matrix elements) are taken from Ref. [131]. The DYNNLO predictions are calculated using the NNLO PDF sets from CT14NNLO [132], NNPDF3.1 [40], MMHT14NNLO68CL [133], HERAPDF2.0 [134] and ABMP16 [135]. All considered PDF sets except HERAPDF2.0 are evaluated from global fits which include to varying extents the LHC measurements of W/Z boson, Drell-Yan, top-quark and inclusive jet production. The renormalization and factorization scales, respectively denoted as μ_{R} and μ_{F}, are set equal to the decay lepton-pair invariant mass, $m_{\ell\nu}$ or $m_{\ell\ell}$.

Uncertainties in these predictions are derived as follows. PDF uncertainties are evaluated from the variations of the NNLO PDFs (the PDF uncertainties of CT14nnlo are rescaled from 90% confidence level to 68% confidence level). Scale uncertainties are defined by the envelope of the variations obtained by changing μ_{R} and μ_{F} by a factor of two with respect to their nominal values and imposing $0.5 \leq \mu_{\text{R}}/\mu_{\text{F}} \leq 2$. The uncertainty induced by the strong coupling constant is estimated by varying α_{S} by ± 0.001 around the central value of $\alpha_{\text{S}}(m_Z) = 0.118$, following the prescription of Ref. [132]; the effect of these variations is estimated by comparing the CT14nnlo_as_0117 and CT14nnlo_as_0119 PDF sets to CT14nnlo. Finally, intrinsic limitations of the NNLO calculations for fiducial cross-section predictions lead to systematic differences between results from different programs, as explained in Ref. [136]. Therefore, an additional uncertainty of 0.7%, estimated from a comparison of predictions calculated with Fewz 3.1 and DYNNLO, is assigned. Theory uncertainties are dominated by our knowledge of the proton PDFs.

The differential cross section for the Z-boson production is shown in Figure 43

as a function of $|y_{\ell\ell}|$. The combined measurement is compared to theoretical calculations with the CT14NNLO, NNPDF3.1, MMHT14NNLO68CL, HERAPDF2.0 and ABMP16 PDF sets, with uncertainties assigned as described above. A comparison shows that the predictions obtained with the NNPDF3.1 PDF set are in good agreement with the measured values, mainly because the NNPDF3.1 global fit includes high precision

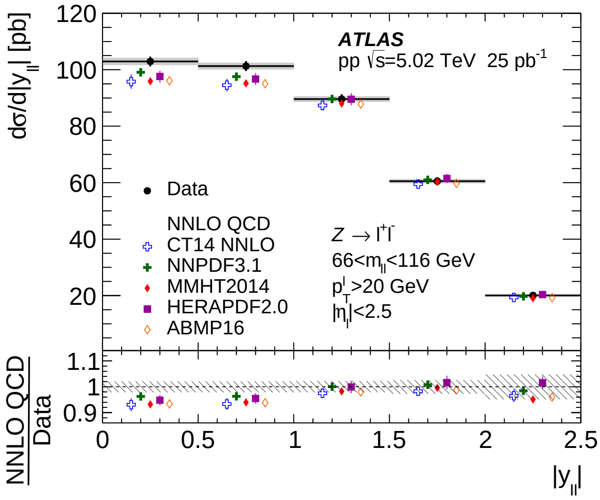

Figure 43: Differential cross section for Z-boson production as a function of absolute lepton-pair rapidity compared with theoretical predictions [74]. Statistical and systematic errors are shown as corresponding bars and shaded bands on the data points. The luminosity uncertainty is not included. Only the dominant uncertainty (PDF) is displayed for the theory. The lower panel shows the ratio of predictions to the measured differential cross section in each bin, and the shaded band shows the sum in quadrature of statistical and systematic uncertainties of the data.

LHC measurements of W/Z boson production [85, 137]. On the other hand, the predictions obtained with other recent PDF sets systematically deviate from the measured values. These deviations are largest at central rapidity for Z boson production.

6.2 Nuclear modification in the p+Pb system

The Z boson measurement in the pp reference system was used to investigate nuclear modification present in the p+Pb system at the same energy. The nuclear modification factor was calculated by using the measurement published by the ATLAS Collaboration in Ref. [63].

The fiducial cross section, in this case, is defined in the full decay lepton kinematic phase space while limiting the Z boson rapidity to $|y_Z| < 2.5$. It was published as a preliminary pp result in this work [138]. It is measured to be 590 ± 9 (stat.)± 12 (syst.)± 32 (lumi.) pb. The simulated MC sample which is used for corrections and contains NLO CT10 PDF has a significantly lower cross section of 537 pb. However, a similar but more accurate NNLO calculation using the CT14 PDF [139] and calculated using a version of

DYNNLO 1.5 [140, 141] yields a cross section of 573.77^{+14}_{-16} pb (where the uncertainties are largely coming from the scale, α_S, and PDF), which agrees well with the measurement within its uncertainties.

The rapidity differential cross section is shown in Figure 44. The data are compared to the simulated MC generated with the CT10 PDF at NLO, scaled to the integrated cross section calculated at NNLO using the CT14 PDF. The scaled simulation is in good agreement with the data.

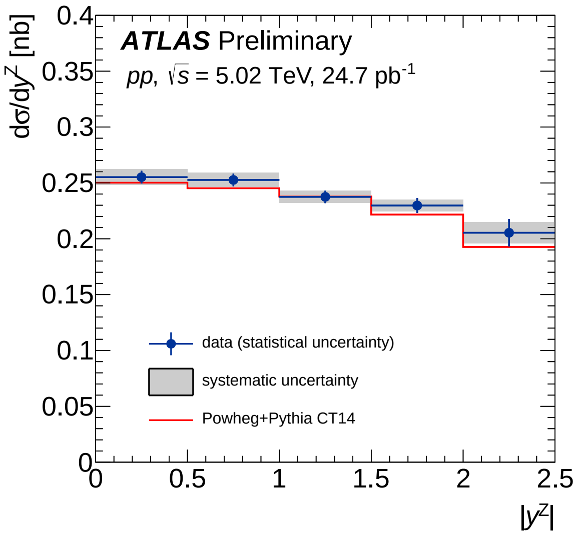

Figure 44: Differential cross section for Z-boson production as a function of absolute lepton-pair rapidity [138]. The data is compared to the simulated MC generated with the CT10 PDF at NLO, scaled to the integrated cross section calculated with DYNNLO at NNLO using the CT14 PDF set.

The Z-boson cross section measured in pp collisions is further used as a baseline to study nuclear modifications which may be present in the previously measured cross section in p+Pb collisions [63]. In the p+Pb collisions the reference system is defined such that the proton travels forward in the positive-rapidity direction and the lead ion travels backwards in the negative-rapidity direction. The nuclear modification factor $R_{p\text{Pb}}$ defined by Eq. 17 is shown in Figure 45 as a function of rapidity. It is compared to the $R_{p\text{Pb}}$ obtained from the MC simulations that include different nucleon combinations, which deviates from unity due to the isospin effects discussed in Section 3.3. The nuclear modification seen in the data demonstrates an enhancement in the lead-going direction and suppression in the proton-going direction. The magnitudes of these effects are larger than expected from one

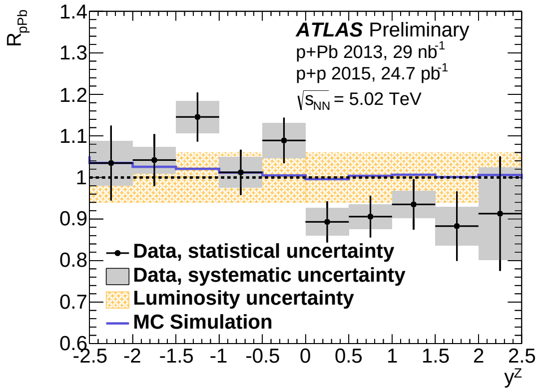

Figure 45: The nuclear modification factor as a function of Z boson rapidity [138]. The uncertainties on each point include statistical and systematic uncertainties from p+Pb and pp measurements. The band around unity represents the uncertainty of the luminosities. The blue line shows an expected $R_{p\mathrm{Pb}}$ based on simulation (see text).

the isospin effects and can be due to the modified nuclear PDF inside the lead nucleus as discussed in [63].

For a better physical understanding of the nuclear modification, one may study its effects as a function of the p+Pb centrality [63]. Using the rapidity differential yield of Z boson candidates in different centrality classes measured in p+Pb collisions [63], the centrality dependent nuclear modification factor is plotted in Figure 46. The p+Pb data are rebinned compared to Figure 45, because of the limited statistical precision in each centrality class. To quantify the change in asymmetry in different centrality classes, the

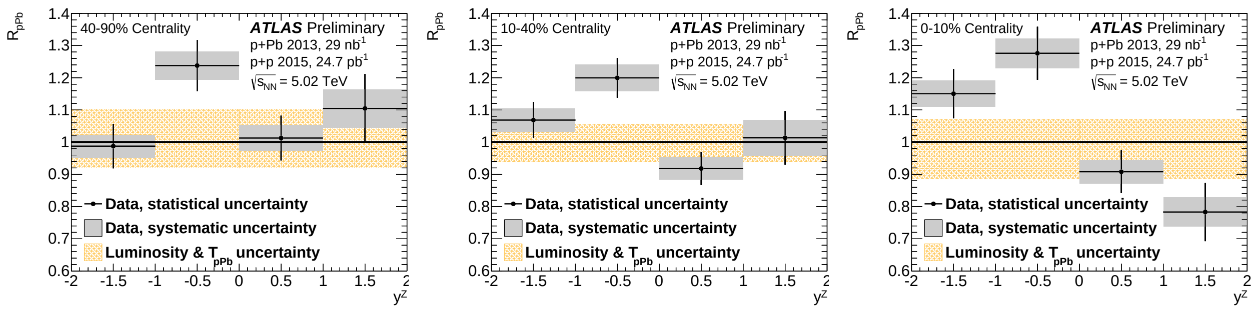

Figure 46: The nuclear modification factor for 40–90% (*left*), 10–40% (*middle*) and 0–10% (*right*) centrality bins [138]. The uncertainties on each point include statistical and systematic uncertainties from p+Pb and pp measurements. The band around unity represents the uncertainty of $\langle T_{p\mathrm{Pb}} \rangle$ and luminosity.

$R_{p\mathrm{Pb}}$ rapidity distributions are fit to a linear function. The slopes for 40–90%, 10–40% and 0–10% centrality bins are measured to be: 0.02 ± 0.04, -0.05 ± 0.03, and -0.14 ± 0.04, respectively. The uncertainties come from the fitting and are dominated by the limited statistics of the p+Pb data. Results suggest that the asymmetry seen in Figure 45 is more pronounced in more central collisions.

6.3 Z-boson production in the Pb+Pb system

The measured cross section in pp data discussed above is used for measuring the nuclear effects in the Pb+Pb system. Z boson production yields per inelastic Pb+Pb collision normalized by the thickness function T_{AA} (normalized yield introduced in Equation 16) are measured deferentially in Z boson rapidity and collision centrality (as a function of the number of participants, N_{part}). The data points are compared with simulation including Z boson signal and background components.

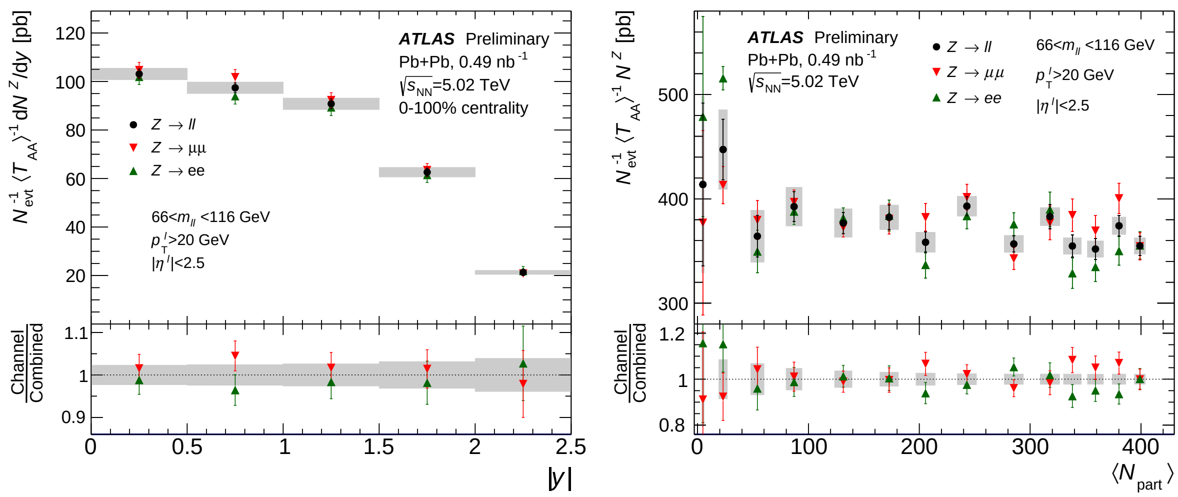

Figure 47: Normalized Z boson yields as a function of lepton-pair rapidity (*left*) and as a function of the number of participants N_{part} (*right*), for the electron, muon and combined results [71]. Lower panels show the ratio of individual channels to the combined result. The error bars in the upper panels show the total uncertainty for muons and electrons and the statistical uncertainty for the combined data. In the lower panel, the error bar shows the statistical uncertainty. The shaded area show the systematic uncertainty of the combined result in both panels. The width of the error band in the right panel corresponds to the systematic uncertainty on $\langle N_{\mathrm{part}} \rangle$, scaled by a factor three for clarity.

The procedure to combine the measurement in Pb+Pb is the same as used in pp. A good agreement between the channels was obtained in different rapidity and centrality bins and the combination yields overall χ^2/d.o.f= 1.7/5 for the rapidity differential result and χ^2/d.o.f= 21.6/14 for the centrality differential measurement. Therefore, electron and muon channels are found to be in agreement. The rapidity distributions for the electron and the muon channel, as well as the combined results, are shown in the left panel of Figure 47. The right panel shows the yields measured versus N_{part}.

The measured cross sections are compared with theoretical predictions obtained using a modified version of DYNNLO 1.5 [128, 129]. The calculation is performed analogously to predictions derived for the *pp* measurement, except for the fact that it is calculated at the NLO order. This is consistent with the order of the calculation for the input nPDFs. The predictions are calculated using the free proton PDF set CT14 NLO [132] typically used to compare with the *pp* data and the nuclear PDF sets nCTEQ15 NLO [142] and EPPS16 NLO [143] which are averaged over the whole Pb nucleus. In addition, the parton-level NLO prediction from the MCFM code [144], interfaced with the CT14 NLO PDF set, is calculated. This takes into account the isospin effect, arising from different partonic compositions of protons and neutrons in Pb nuclei, which is neglected in DYNNLO calculations. The uncertainties on the theory predictions are derived following the same procedure as described for the *pp* system above. In Figure 48 the normalized

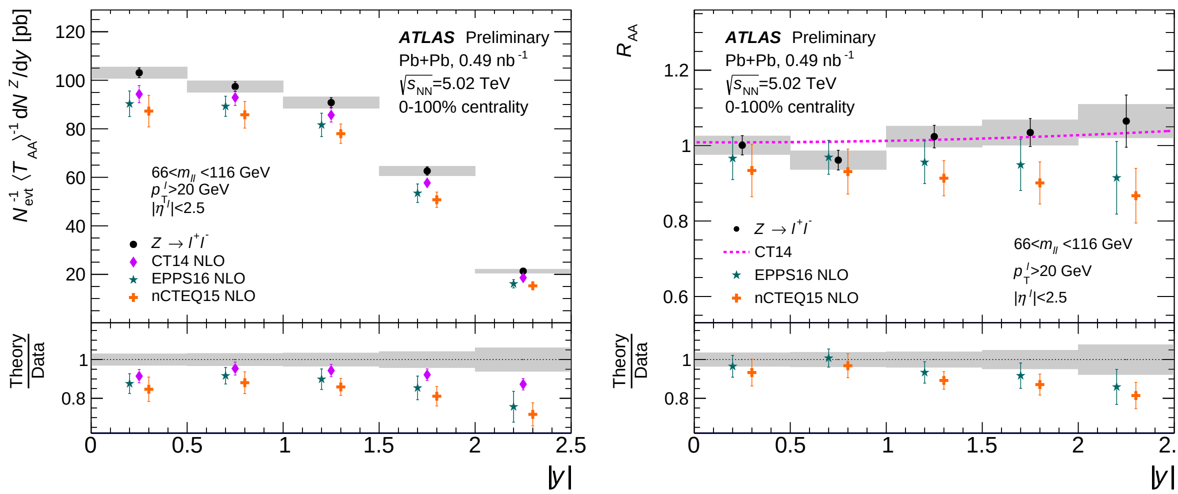

Figure 48: Normalized Z boson yields as a function of rapidity (*left*) and the R_{AA} (*right*) compared to theoretical predictions [71]. The lower panels show the ratio of predictions to the data. The band is the total uncertainties of the data less the luminosity.

yields are compared for the combined measurement and theoretical predictions calculated with the CT14nlo, nCTEQ15 and EPPS16 PDF sets. All the calculations lie 1–3 combined standard deviations below the measured result. In modeling the R_{AA}, only the nPDF uncertainties play a role since the CT14nlo uncertainties cancel out. Calculations are consistent with the data within one standard deviation for PDF and 1–2 standard deviations for nPDF. The trend observed in data can be entirely explained by the isospin effect as shown in the upper right panel of Figure 48 by the dashed line.

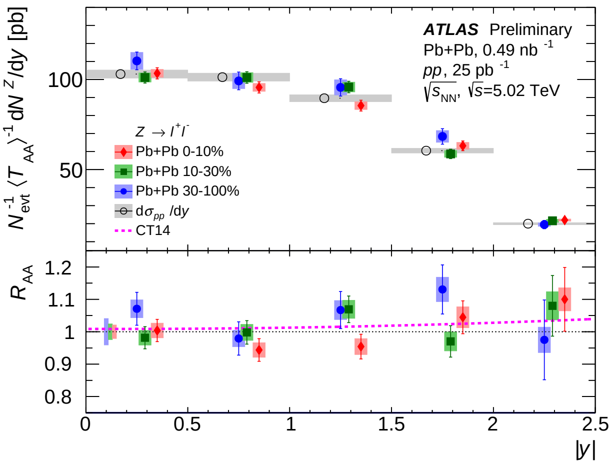

Figure 49: Normalized Z boson yield versus rapidity measured in three centrality intervals: peripheral 30–100% (blue circles), mid-central 10–30% (green squares) and central 0–10% (red diamonds) [71]. The differential Z boson cross sections measured in pp collisions are shown by open circles [74]. The lower panel shows the R_{AA} and the contribution from the isospin effect calculated with CT14 NLO PDF (dashed line). The shaded boxes at unity indicate the combined uncertainty from the pp data added in quadrature to the T_{AA} uncertainty. The points in each centrality interval are shifted horizontally relative to the bin centre for clarity.

Figure 49 shows in the upper panel the rapidity distributions of the Z boson normalized yields compared to σ^Z_{pp} in three centrality intervals. The Pb+Pb and pp production yields are used to construct the R_{AA} shown in the lower panels. The results are consistent with each other within the statistical uncertainties. The current data statistics precludes making a more definitive statement about any possible modification of the Z boson rapidity distribution with centrality.

Figure 50 shows the centrality dependence of the normalized Z boson yield and of the R_{AA}. The point corresponding to the pp cross section [74] is added to the plot at

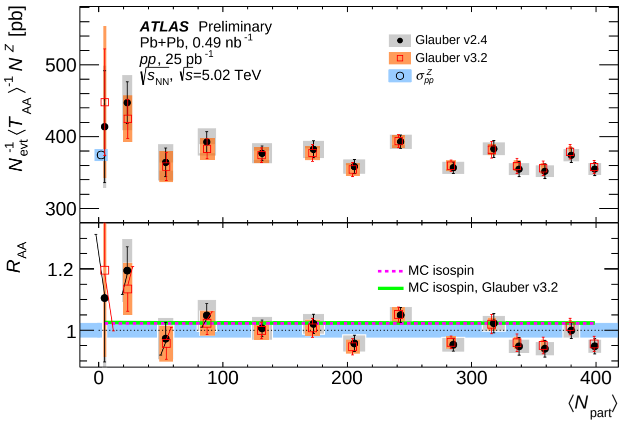

Figure 50: The upper panel shows the normalized Z boson yield as a function of $\langle N_{\text{part}}\rangle$ [71]. The integrated fiducial cross section measured in the pp system is shown at $N_{\text{part}} = 2$ (open circle) [74]. The lower panel shows the nuclear modification factor. The band indicates the uncertainty of the pp data. The figure shows the results calculated with the Glauber MC v2.4 [4] and v3.2 [145]. The dashed and the full line indicate CT14 NLO PDF calculations that account for isospin effects for the two Glauber MC versions. The width of the error band in each centrality interval corresponds to the systematic uncertainty in $\langle N_{\text{part}}\rangle$, scaled by a factor of three for clarity.

$N_{\text{part}} = 2$. The results are derived based on the Glauber MC v2.4 and a newer version v3.2 following the same procedure as described in Ref. [70]. The results are found to be consistent with each other within measurement uncertainties. The new Glauber MC calculation [145] implements a more advanced treatment of the nuclear density profile and the updated experimental value of the nucleon–nucleon inelastic cross section, where the former directly affects the normalized Z boson yield derived in this analysis. The new model also leads to a set of reduced systematic uncertainties compared with the previous version.

In the estimation of the isospin effect contribution shown with dashed lines, the Glauber MC v3.2 model accounts for different distributions of protons and neutrons in Pb nuclei known as the neutron skin effect. Due to the weak dependence of Z boson production on isospin, the prediction is essentially constant.

The normalized yields are consistent with the pp cross section at all measured centralities and show only a weak dependence on N_{part}. The values of R_{AA}, shown in the lower panel, are consistent with unity within the total systematic uncertainty. When the

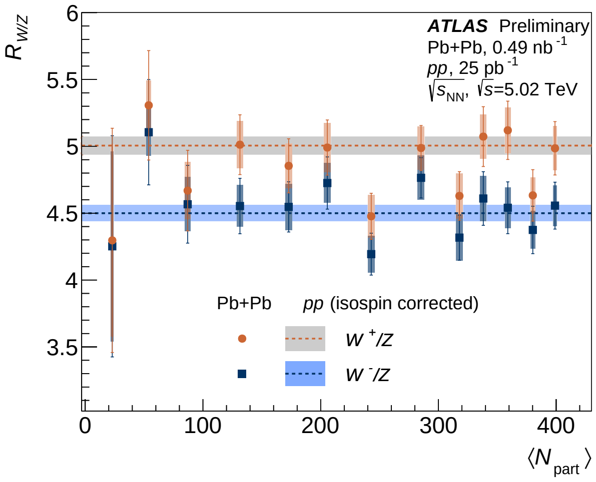

Figure 51: Ratio of W^+ (circles) and W^- (squares) yields measured in the same data set [70] to the yields of Z bosons [71] versus $\langle N_{\text{part}} \rangle$, compared with the ratios measured in pp data [74] (shaded line) scaled by the isospin factor obtained from the CT14 NLO PDF calculation.

isospin effect is taken into account as shown with the dashed line, the model tends to better agree with the data at low N_{part} values rather than at high values.

For both Glauber model versions, an apparent decrease is observed in the R_{AA} with the event centrality. To quantify this dependence, a linear fit was performed taking into account statistical and systematic uncertainties coming from the measurement and the inherent model systematic uncertainties related to the Glauber modeling (such as the inelastic nucleon-nucleon cross section, nucleon hard core radius and Woods-Saxon parameters). In addition to these variations, another uncertainty in the Glauber model is related to a working point chosen for the fit to the data. Details on the extraction of the geometrical parameters in the Glauber MC modeling can be found in Ref. [52]. The decrease in the R_{AA} between the most-peripheral (80–100%) and most-central (0–2%) centrality intervals is found to be $(10 \pm 7)\%$ and $(6 \pm 6)\%$ for the Glauber MC v2.4 and v3.2, respectively.

The Z boson measurement is used to compare the N_{part} dependence of the W [70] and Z bosons by calculating their yield ratios as shown in Figure 51, where the uncertainties of the two measurements are treated as uncorrelated. The data points are compared with the ratio measured in pp collisions [74], which is scaled by the isospin factors calculated based on the CT14 NLO PDF set. The measurements for both channels are found to be

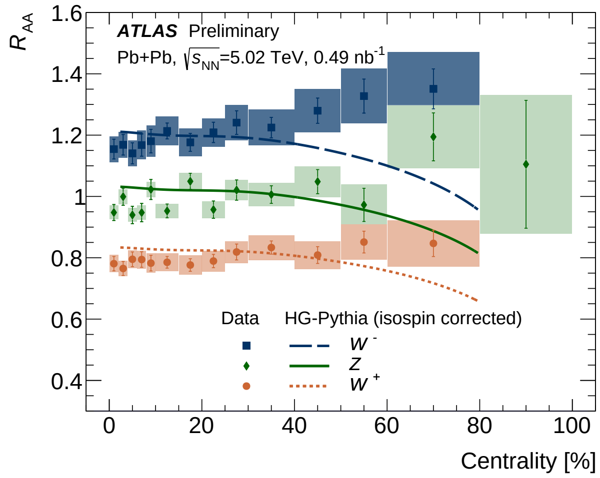

Figure 52: Nuclear modification factor R_{AA} in centrality intervals compared with the HG-PYTHIA model [93] scaled by the isospin factor obtained from the CT14 NLO PDF calculation [71]. The model accounts for a biased classification of the event geometry for events containing a hard process. The bins are ordered in the centrality percentile, starting from central events on the left and going towards more peripheral on the right. The comparison is shown in the 0–80% centrality interval where the different smearing of the ATLAS centrality estimator ($\Sigma E_{\mathrm{T}}^{\mathrm{FCal}}$) is found to have a negligible effect.

consistent with the scaled pp measurement and show constant behavior as a function of centrality.

The trend of the points shown in Figure 50 for Z bosons is different from the trend observed by the ALICE Collaboration in the measurements with charged hadrons with high transverse momentum [96] and the one predicted by the HG-PYTHIA model [93] discussed in Section 4.3. Figure 52 shows the R_{AA} for $W^{\pm}$ [70] and Z bosons compared with the HG-PYTHIA model [93].

To compare the model with the measurements done with massive electroweak bosons the results are corrected for the isospin effects using the CT14 NLO PDF. All three data sets show consistent trends between the species but are different from their corresponding model predictions. This suggests that the apparent suppression mechanism [93] that explains the ALICE data [96] for the yields of high-p_{T} charged particles does not have the same effect on the yields of massive electroweak bosons.

7 Discussion

This thesis presented the results on the Z boson cross-section measurement in the pp data at 5.02 TeV center-of-mass energy and the measurement of the Z boson normalized yield in the Pb+Pb system at the same collision energy. The rapidity differential cross section was compared with the NNLO pQCD calculations including the latest proton PDFs as shown in Figure 43. The same was done in the Pb+Pb data for the normalized Z boson yield and the nuclear modification factor R_{AA} where the comparisons are done with NLO pQCD calculations with the latest PDF and nPDF sets, shown in Figure 48. In the same data set the Z yield and the R_{AA} were measured as a function of the event centrality and compared with the GMC calculation (Figure 50) and the HG-PYTHIA model (Figure 52).

The Z boson result in the pp system is a new contribution to the set of Standard Model heavy EW boson measurements and forms the baseline for comparisons to HI results. The fiducial Z cross section is measured with a high precision of 2.3% (1.3% without the luminosity uncertainty) with the ATLAS detector. The result is in agreement with the pQCD NNLO calculations [74]. Figure 53 shows the ratio of cross sections measured in electron and muon decay channels for W and Z boson from previous ATLAS measurements including the results of this thesis compared to the Standard Model prediction of lepton universality [146]. Theoretical calculations of the rapidity differential cross section based on different PDF sets are consistent with the measurements at the level of 1–2 standard deviations with the largest discrepancy measured at mid-rapidity. This trend in rapidity was already measured with ATLAS at the higher center-of-mass energy of $\sqrt{s} = 7$ TeV [85, 147]. A follow-up ATLAS measurement using the 2017 pp data sample with approximately 10 times larger statistics compared to the result presented in this work and at the same energy of 5.02 TeV will provide more precise input to the future PDF fits.

By using the pp measurement as a baseline, the nuclear modification factor is measured in the p+Pb and Pb+Pb systems. A significant suppression is observed in the p+Pb system in the forward rapidity region on the proton going side which reveals the presence of the nuclear modification to the free proton PDF (Figure 46). This result has the final word since the previous results [63] were compared to NLO predictions which underestimated the cross section. Furthermore, the nPDF modification shows indications of centrality

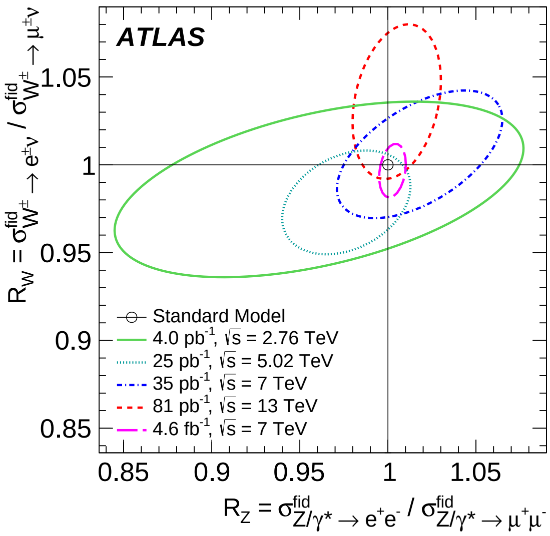

Figure 53: The measured ratio of $W \to e^{\pm}\nu$ and $W \to \mu^{\pm}\nu$ cross sections versus the measured ratio of $Z \to e^{+}e^{-}$ and $Z \to \mu^{+}\mu^{-}$ cross sections is shown as a dotted cyan ellipse which indicates the total of the statistical and systematic uncertainties at 68% confidence level for this measurement. This result is compared with the Standard Model expectation (open circle marker) and the uncertainty ellipses for previous measurements of this quantity by ATLAS [146].

dependence, where the largest effect, on the level of 3 standard deviations, is observed in most central collisions. The centrality dependence of the nPDF modification has yet to be described by the theoretical models. This result is in agreement with the ATLAS preliminary result for the W boson production at the same energy [64].

The normalized Z boson yield measured as a function of rapidity in Pb+Pb collisions was compared to current NLO pQCD predictions with free and nuclear PDF sets. It was found to lie 1–3 standard deviations above the calculations, where the difference increases towards forward Z rapidity ($y > 2$). A better description of the data concerning the overall normalization was measured for the free proton PDF set. This is consistent with the W boson measurement performed by ATLAS in the same data set [70] but it stands in tension with the recent Z boson result from the ALICE collaboration performed at large rapidities that reports a better agreement with nPDF calculations [73]. More precise data available in the 2018 Pb+Pb data set is expected to address this discrepancy in more detail while a partial overlap in the rapidity coverage between the experiments can be accomplished by employing ATLAS capabilities for reconstructing forward electrons.

Furthermore, the Z production yield measured in the Pb+Pb system is the first measurement of the Z boson R_{AA} and provides a test of the centrality association made by all HI experiments with unprecedented precision. Even though the R_{AA} decreases from peripheral to central events, it is found to be consistent with a constant behavior in centrality and to agree with the prediction based on the CT14 PDF set that takes isospin into account. A difference between the slopes evaluated for R_{AA} in centrality for two Glauber MC calculations might indicate an improvement in the modeling. Similar behavior in centrality that was studied for the Z boson R_{AA} was also reported for W boson R_{AA} in the same data set [70], where the peripheral excess in measured yields is 1–2 standard deviations above the Glauber model prediction. This might point to a need of introducing additional corrections in the fitting procedure of the GMC model that would account for the behavior measured in data and reproduce a globally flat fit for the yields of EW bosons. Furthermore, we suggest constructing double ratios of yields of colored hard probes (such as jets or quarkonia) to the yields of EW bosons in centrality classes as a better and more robust measure of QGP medium effects. Finally, no apparent suppression in the peripheral collisions reported by the ALICE experiment in the measurement of high-p_{T} charged hadrons [148, 96] is detected in the Z boson ATLAS measurement. This could shed more light on the nature of the effect measured by ALICE, which may be different from the interpretation given in the original paper [93]. The centrality dependence needs further study, which may be possible with a higher statistics 2018 data sample.

As discussed in Section 5.4.3 the background contribution coming from photon-induced processes consists of two components. One is the photon-photon scattering that was previously measured [111] while the second component comes from the photonuclear Z boson production that has not been observed so far. One can try to distinguish between the two contributions based on the event topology, namely by measuring rapidity gaps in the detector that are predominantly both-sided for photon-photon scattering events and single-sided for photonuclear events. The breakdown of all events with and without large gaps found in data is given in Table 6 together with the response registered in ZDC detectors. There are in total 34 events with large rapidity gaps in both decay channels, from which 27 have gaps on both sides of the detector and 7 have one-sided gaps. Here we examine whether these 7 events can be considered as photonuclear event candidates.

From 7 events with one-sided gaps, 4 have one-sided ZDC signal and 3 two-sided.

This is consistent with a probability of ZDC measuring neutrons fragmented from nuclei undergoing EM interactions. The evidence for this comes from studying 27 events with two-sided gaps. The analysis of these events reveals that in about 40% of interactions at least one neutron reaches the ZDC. This fraction is consistent with predictions from the STARLIGHT 1.1 generator and therefore explains 3 two-sided events observed in this analysis. We examine three other potential sources for events with one-sided gaps: 1) $\gamma + \gamma$ processes with in-time pileup, 2) hadronic collisions that contain gaps and finally, 3) $\gamma + \gamma$ events with additional particle production masking the gap on one side. It is easy to show that the first contribution is negligible. Assuming all 27 events with two gaps are $\gamma + \gamma$ events a probability that there is such an event with pile-up is given by instantaneous luminosity during the data taking (discussed in Section 5.4.4) which yields 0.05 events. This estimate neglects the fact that such an event should have no gaps due to a large hadronic activity of Pb+Pb inelastic events and the same is true for the interaction of the Pb ion with residual gas in the collider. The second contribution is a probability for a hadronic event with a Z boson to have gaps which in Section 5.4.3 was estimated to about 0.05 events. Finally, one can assume that $\gamma + \gamma$ events can produce high-mass dilepton states with an additional particle production. This process has not yet been studied in detail and no quantitative analysis exists. At this point, we cannot estimate this background source.

Making an explicit assumption that the last background source is small we consider 7 events with large one-sided gaps as candidates for yet unmeasured $\gamma + A$ process suggested in Ref. [109]. This would result in a cross section of about 20 nb assuming that the detector efficiencies for this process are similar to the ones of the hadronic Z production. That cross section is two orders of magnitude larger compared to the calculation reported in the literature (0.2 nb as quoted in Ref. [109] after accounting for the leptonic branching ratio). This apparent discrepancy is very intriguing and should further be studied in larger Pb+Pb data sets at the LHC. Finally, this demonstrates the capability of the ATLAS detector to for the first time detect the photonuclear Z production.

In conclusion, this work is an important, incremental step in our understanding of QCD and the quark-gluon plasma via analyzing the Z boson production. High precision estimates of the Z boson yields were performed in 2015 pp and Pb+Pb data sets. This improves the fitting of theoretical models and highlights the need to take into account centrality dependence. It also brings to attention the importance of understanding the contribution of ultra-peripheral hard processes. Finally, this work assists in the analysis of future measurements and paves the way for discovering new phenomena in high-energy nuclear physics.

References

[1] Michele Arneodo. Nuclear effects in structure functions. Physics Reports, 240(5): 301–393, 1994. doi: http://dx.doi.org/10.1016/0370-1573(94)90048-5.

[2] P. R. Norton. The EMC effect. Reports on Progress in Physics, 66:1253–1297, 2003. doi: 10.1088/0034-4885/66/8/201.

[3] Simona Malace, David Gaskell, Douglas W. Higinbotham, and Ian Cloet. The Challenge of the EMC Effect: existing data and future directions. Int. J. Mod. Phys., E23(08):1430013, 2014. doi: 10.1142/S0218301314300136.

[4] Michael L. Miller, Klaus Reygers, Stephen J. Sanders, and Peter Steinberg. Glauber modeling in high energy nuclear collisions. Ann. Rev. Nucl. Part. Sci., 57:205–243, 2007. doi: 10.1146/annurev.nucl.57.090506.123020.

[5] R. C. Hwa and X. N. Wang (editors). Quark-gluon plasma. Vol. 3. World Scientific, River Edge, USA, 2004.

[6] L. Lellouch, R. Sommer, B. Svetitsky, A. Vladikas, and L. F. Cugliandolo. Modern perspectives in lattice QCD: Quantum field theory and high performance computing. Oxford University Press, Oxford, UK, 2011.

[7] R. K. Ellis, W. J. Stirling, and B. R. Webber. QCD and Collider Physics. Cambridge Monographs on Particle Physics, Nuclear Physics and Cosmology. Cambridge University Press, 1996. doi: 10.1017/CBO9780511628788.

[8] David J. Gross and Frank Wilczek. Ultraviolet behavior of non-abelian gauge theories. Phys. Rev. Lett., 30:1343–1346, Jun 1973. doi: 10.1103/PhysRevLett.30.1343.

[9] ALICE Collaboration. Direct photon production in Pb-Pb collisions at $\sqrt{s_{NN}} =$ 2.76 TeV. Phys. Lett., B754:235–248, 2016. doi: 10.1016/j.physletb.2016.01.020.

[10] Szabolcs Borsanyi, Gergely Endrodi, Zoltan Fodor, Antal Jakovac, Sandor D. Katz, Stefan Krieg, Claudia Ratti, and Kalman K. Szabo. The QCD equation of state with dynamical quarks. JHEP, 11:077, 2010. doi: 10.1007/JHEP11(2010)077.

[11] C. Y. Wong. Introduction to High-Energy Heavy Ion Collisions. 1995.

[12] R. Hagedorn. Statistical thermodynamics of strong interactions at high-energies. Nuovo Cim. Suppl., 3:147–186, 1965.

[13] STAR Collaboration. Experimental and theoretical challenges in the search for the quark gluon plasma: The STAR Collaboration's critical assessment of the evidence from RHIC collisions. Nucl. Phys., A757:102–183, 2005. doi: 10.1016/j.nuclphysa.2005.03.085.

[14] BRAHMS Collaboration. Quark gluon plasma and color glass condensate at RHIC? The Perspective from the BRAHMS experiment. Nucl. Phys., A757:1–27, 2005. doi: 10.1016/j.nuclphysa.2005.02.130.

[15] PHOBOS Collaboration. The PHOBOS perspective on discoveries at RHIC. Nucl. Phys. A, 757:28–101, 2005. doi: 10.1016/j.nuclphysa.2005.03.084.

[16] PHENIX Collaboration. Formation of dense partonic matter in relativistic nucleus-nucleus collisions at RHIC: Experimental evaluation by the PHENIX collaboration. Nucl. Phys., A757:184–283, 2005. doi: 10.1016/j.nuclphysa.2005.03.086.

[17] E. Shuryak. Why does the quark gluon plasma at RHIC behave as a nearly ideal fluid? Prog. Part. Nucl. Phys., 53:273–303, 2004. doi: 10.1016/j.ppnp.2004.02.025.

[18] G. Odyniec. Future of the beam energy scan program at rhic. EPJ Web of Conferences, 95:03027, 2015. doi: 10.1051/epjconf/20149503027.

[19] Wit Busza, Krishna Rajagopal, and Wilke van der Schee. Heavy Ion Collisions: The Big Picture, and the Big Questions. Ann. Rev. Nucl. Part. Sci., 68:339–376, 2018. doi: 10.1146/annurev-nucl-101917-020852.

[20] UA1 Collaboration. Experimental observation of isolated large transverse energy electrons with associated missing energy at $\sqrt{s} = 540$ GeV. Phys. Lett. B, 122: 103–116, 1983. doi: 10.1016/0370-2693(83)91177-2.

[21] UA2 Collaboration. Observation of single isolated electrons of high transverse momentum in events with missing transverse energy at the CERN $\bar{p}p$ collider. Phys. Lett. B, 122:476–485, 1983. doi: 10.1016/0370-2693(83)91605-2.

[22] UA1 Collaboration. Observation of muonic Z^0-decay at the $\bar{p}p$ collider. Phys. Lett., 147B:241–248, 1984. doi: 10.1016/0370-2693(84)90628-2.

[23] UA2 Collaboration. Evidence for $Z^0 \rightarrow e^+e^-$ at the CERN $\bar{p}p$ Collider. Phys. Lett. B, 129:130–140, 1983. doi: 10.1016/0370-2693(83)90744-X.

[24] P. Zerwas. W & Z physics at LEP. Eur. Phys. J. C, 34:41–49, 2004. doi: 10.1140/epjc/s2004-01765-9.

[25] D. Chakraborty. Top quark and W/Z results from the Tevatron. In Proceedings, 37th Rencontres de Moriond, pages 53–58, 2002.

[26] ATLAS Collaboration. Observation of centrality-dependent acoplanarity for muon pairs produced via two-photon scattering in Pb+Pb collisions at $\sqrt{s_{\mathrm{NN}}} = 5.02$ TeV with the ATLAS detector. Phys. Rev. Lett., 121(21):212301, 2018. doi: 10.1103/PhysRevLett.121.212301.

[27] Krzysztof Cichy and Martha Constantinou. A guide to light-cone PDFs from Lattice QCD: an overview of approaches, techniques and results. Adv. High Energy Phys., 2019:3036904, 2019. doi: 10.1155/2019/3036904.

[28] M. Wing. Zeus papers, 2016. URL https://www-zeus.desy.de/zeus_papers/zeus_papers.html. Last update: August 19, 2016.

[29] S. Schmitt. The h1 experiment at hera, 2019. URL https://h1.desy.de/e104552/e104555/. Last update: 18 June 2019.

[30] New Muon Collaboration. Accurate measurement of F_2^d/F_2^p and $R_d - R_p$. Nucl. Phys. B, 487:3–26, 1997. doi: 10.1016/S0550-3213(96)00673-6.

[31] New Muon Collaboration. Measurement of the proton and deuteron structure functions, F_2^p and F_2^d, and of the ratio σ_L/σ_T. Nucl. Phys. B, 483:3–43, 1997. doi: 10.1016/S0550-3213(96)00538-X.

[32] BCDMS Collaboration. A high statistics measurement of the proton structure functions $f_2(x, q^2)$ and r from deep inelastic muon scattering at high q^2. Phys. Lett. B, 223:485, 1989.

[33] BCDMS Collaboration. A high statistics measurement of the deuteron structure functions $f_2(x, q^2)$ and r from deep inelastic muon scattering at high q^2. Phys. Lett. B, 237:592, 1990.

[34] L. W. Whitlow, E. M. Riordan, S. Dasu, S. Rock, and A. Bodek. Precise measurements of the proton and deuteron structure functions from a global analysis of the SLAC deep inelastic electron scattering cross-sections. Phys. Lett. B, 282:475–482, 1992.

[35] CHORUS Collaboration. Measurement of nucleon structure functions in neutrino scattering. Phys. Lett. B, 632:65–75, 2006.

[36] NuTeV Collaboration. Precise Measurement of Dimuon Production Cross-Sections in ν_μ Fe and $\bar{\nu}_\mu$ Fe Deep Inelastic Scattering at the Tevatron. Phys. Rev. D, 64: 112006, 2001. doi: 10.1103/PhysRevD.64.112006.

[37] D0 Collaboration. Measurement of the shape of the boson rapidity distribution for $p\bar{p} \to Z/\gamma^* \to e^+e^- + X$ events produced at $\sqrt{s}$ of 1.96 TeV. Phys. Rev. D, 76: 012003, 2007. doi: 10.1103/PhysRevD.76.012003.

[38] CDF Collaboration. Measurement of the inclusive jet cross section at the Fermilab Tevatron $p\bar{p}$ collider using a cone-based jet algorithm. Phys. Rev. D, 78:052006, 2008. doi: 10.1103/PhysRevD.79.119902,10.1103/PhysRevD.78.052006. [Erratum: Phys. Rev.D79,119902(2009)].

[39] CDF Collaboration. Measurement of $d\sigma/dy$ of Drell-Yan e^+e^- pairs in the Z mass region from $p\bar{p}$ collisions at $\sqrt{s} = 1.96$ TeV. Phys. Lett. B, 692:232–239, 2010. doi: 10.1016/j.physletb.2010.06.043.

[40] Richard D. Ball et al. Parton distributions for the LHC Run II. JHEP, 04:040, 2015. doi: 10.1007/JHEP04(2015)040.

[41] Kari J. Eskola, Petja Paakkinen, Hannu Paukkunen, and Carlos A. Salgado. EPPS16: Nuclear parton distributions with LHC data. Eur. Phys. J. C, 77(3): 163, 2017. doi: 10.1140/epjc/s10052-017-4725-9.

[42] Donald F. Geesaman, K. Saito, and Anthony William Thomas. The nuclear EMC effect. Ann. Rev. Nucl. Part. Sci., 45:337–390, 1995. doi: 10.1146/annurev.ns.45.120195.002005.

[43] R. J. Glauber. High-Energy Collision Theory, In Lectures in Theoretical Physics. 1959.

[44] R. J. Glauber. Cross sections in deuterium at high energies. Phys. Rev., 100:242–248, Oct 1955. doi: 10.1103/PhysRev.100.242.

[45] V. Franco and R. J. Glauber. High-energy deuteron cross sections. Phys. Rev., 142:1195–1214, Feb 1966. doi: 10.1103/PhysRev.142.1195.

[46] R.J. Glauber and G. Matthiae. High-energy scattering of protons by nuclei. Nuclear Physics B, 21(2):135–157, 1970. doi: https://doi.org/10.1016/0550-3213(70)90511-0.

[47] W. Czyż and L. Leśniak. Elastic scattering of very high energy particles from nuclei. Physics Letters B, 24(5):227–229, 1967. ISSN 0370-2693. doi: https://doi.org/10.1016/0370-2693(67)90469-8.

[48] W. Czyż and L. C. Maximon. High energy, small angle elastic scattering of strongly interacting composite particles. Annals of Physics, 52:59–121, 1969.

[49] A. Białłas, M. Bleszyński, and W. Czyż. Multiplicity distributions in nucleus-nucleus collisions at high energies. Nuclear Physics B, 111:461–476, 1976. doi: https://doi.org/10.1016/0550-3213(76)90329-1.

[50] Nuclear charge-density-distribution parameters from elastic electron scattering. Atomic Data and Nuclear Data Tables, 36(3):495 – 536, 1987. doi: https://doi.org/10.1016/0092-640X(87)90013-1.

[51] C. Loizides, J. Nagle, and P. Steinberg. Improved version of the PHOBOS Glauber Monte Carlo. 2014. doi: 10.1016/j.softx.2015.05.001.

[52] D. Perepelitsa, P. Steinberg, M. Zhou, S. Radhakrishnan, and S. Tapia-Araya. Centrality determination in $\sqrt{s_{NN}} = 5.02$ TeV Pb+Pb collision data in 2015. Technical

Report ATL-COM-PHYS-2016-1287, 2016. URL https://cds.cern.ch/record/2212936/.

[53] ATLAS Collaboration. The ATLAS Experiment at the CERN Large Hadron Collider. JINST, 3:S08003, 2008. doi: 10.1088/1748-0221/3/08/S08003.

[54] ATLAS Collaboration. ATLAS Insertable B-Layer Technical Design Report. ATLAS-TDR-19, 2010. URL https://cds.cern.ch/record/1291633.

[55] ATLAS Collaboration. ATLAS Insertable B-Layer Technical Design Report Addendum. ATLAS-TDR-19-ADD-1, 2012. URL https://cds.cern.ch/record/1451888.

[56] B. Abbott et al. Production and integration of the ATLAS Insertable B-Layer. JINST, 13(05):T05008, 2018. doi: 10.1088/1748-0221/13/05/T05008.

[57] Christian W. Fabjan and Fabiola Gianotti. Calorimetry for particle physics. Rev. Mod. Phys., 75:1243–1286, Oct 2003. doi: 10.1103/RevModPhys.75.1243.

[58] P. Puzo. Atlas calorimetry. Nuclear Instruments and Methods in Physics Research Section A: Accelerators, Spectrometers, Detectors and Associated Equipment, 494 (1):340 – 345, 2002. doi: https://doi.org/10.1016/S0168-9002(02)01490-0.

[59] Xin-Nian Wang and Miklos Gyulassy. Energy and centrality dependence of rapidity densities at RHIC. Phys. Rev. Lett., 86:3496–3499, 2001. doi: 10.1103/PhysRevLett.86.3496.

[60] ATLAS Collaboration. Measurement of photon–jet transverse momentum correlations in 5.02 TeV Pb+Pb and *pp* collisions with ATLAS. Phys. Lett. B, 789:167–190, 2019. doi: 10.1016/j.physletb.2018.12.023.

[61] ATLAS Collaboration. Measurement of the production and lepton charge asymmetry of W bosons in Pb+Pb collisions at $\sqrt{s_{\mathrm{NN}}} = 2.76$ TeV with the ATLAS detector. Eur. Phys. J. C, 75(1):23, 2015. doi: 10.1140/epjc/s10052-014-3231-6.

[62] ATLAS Collaboration. Measurement of Z boson Production in Pb+Pb Collisions at $\sqrt{s_{NN}} = 2.76$ TeV with the ATLAS Detector. Phys. Rev. Lett., 110(2):022301, 2013. doi: 10.1103/PhysRevLett.110.022301.

[63] ATLAS Collaboration. Z boson production in p+Pb collisions at $\sqrt{s_{NN}} = 5.02$ TeV measured with the ATLAS detector. Phys. Rev. C, 92(4):044915, 2015. doi: 10.1103/PhysRevC.92.044915.

[64] ATLAS Collaboration. Measurement of $W \to \mu\nu$ production in p+Pb collision at $\sqrt{s_{\rm NN}} = 5.02$ TeV with ATLAS detector at the LHC. Technical Report ATLAS-CONF-2015-056, CERN, Geneva, 2015. URL https://cds.cern.ch/record/2055677.

[65] CMS Collaboration. Study of Z boson production in PbPb collisions at $\sqrt{s_{NN}} = 2.76$ TeV. Phys. Rev. Lett., 106:212301, 2011. doi: 10.1103/PhysRevLett.106.212301.

[66] CMS Collaboration. Study of W boson production in PbPb and pp collisions at $\sqrt{s_{NN}} = 2.76$ TeV. Phys. Lett. B, 715:66–87, 2012. doi: 10.1016/j.physletb.2012.07.025.

[67] CMS Collaboration. Study of W boson production in pPb collisions at $\sqrt{s_{\rm NN}} = 5.02$ TeV. Phys. Lett. B, 750:565–586, 2015. doi: 10.1016/j.physletb.2015.09.057.

[68] CMS Collaboration. Study of Z boson production in pPb collisions at $\sqrt{sNN}$=5.02TeV. Phys. Lett. B, 759:36–57, 2016. doi: 10.1016/j.physletb.2016.05.044.

[69] LHCb Collaboration. Observation of Z production in proton-lead collisions at LHCb. JHEP, 09:030, 2014. doi: 10.1007/JHEP09(2014)030.

[70] ATLAS Collaboration. Measurement of $W^{\pm}$ boson production in Pb+Pb collisions at $\sqrt{s_{\rm NN}} = 5.02$ TeV with the ATLAS detector. CERN-EP-2019-123, 2019.

[71] ATLAS Collaboration. Z boson production in Pb+Pb collisions at $\sqrt{s_{NN}} = 5.02$ TeV measured by the ATLAS detector. Technical Report ATLAS-CONF-2019-024, CERN, Geneva, Jul 2019. URL https://cds.cern.ch/record/2681562.

[72] CMS Collaboration. Observation of nuclear modifications in $W^{\pm}$ boson production in pPb collisions at $\sqrt{s_{\rm NN}} = 8.16$ TeV. CERN-EP-2018-283, 2019.

[73] ALICE Collaboration. Measurement of Z^0-boson production at large rapidities in Pb-Pb collisions at $\sqrt{s_{\rm NN}} = 5.02$ TeV. Phys. Lett. B, 780:372–383, 2018. doi: 10.1016/j.physletb.2018.03.010.

[74] ATLAS Collaboration. Measurements of W and Z boson production in pp collisions at $\sqrt{s} = 5.02$ TeV with the ATLAS detector. Eur. Phys. J. C, 79(2):128, 2019. doi: 10.1140/epjc/s10052-019-6870-9,10.1140/epjc/s10052-019-6622-x. [Erratum: Eur. Phys. J.C79,no.5,374(2019)].

[75] CMS Collaboration. Observation of long-range near-side angular correlations in proton-lead collisions at the LHC. Phys. Lett. B, 718:795–814, 2013. doi: 10.1016/j.physletb.2012.11.025.

[76] ALICE Collaboration. Long-range angular correlations on the near and away side in p-Pb collisions at $\sqrt{s_{\rm NN}}$ =5.02 TeV. Phys. Lett. B, 719:29–41, 2013. doi: 10.1016/j.physletb.2013.01.012.

[77] ATLAS Collaboration. Observation of Associated Near-Side and Away-Side Long-Range Correlations in $\sqrt{s_{\rm NN}}$ =5.02 TeV Proton-Lead Collisions with the ATLAS Detector. Phys. Rev. Lett., 110(18):182302, 2013. doi: 10.1103/PhysRevLett.110.182302.

[78] PHENIX Collaboration. Quadrupole Anisotropy in Dihadron Azimuthal Correlations in Central $d + Au$ Collisions at $\sqrt{s_{\rm NN}}$=200 GeV. Phys. Rev. Lett., 111(21):212301, 2013. doi: 10.1103/PhysRevLett.111.212301.

[79] ALICE Collaboration. Measurements of the heavy-flavour nuclear modification factor in p-Pb collisions at with ALICE at the LHC. Nuclear Physics A, 931:546 – 551, 2014. doi: http://dx.doi.org/10.1016/j.nuclphysa.2014.08.067.

[80] PHENIX Collaboration. Cold-Nuclear-Matter Effects on Heavy-Quark Production at Forward and Backward Rapidity in d+Au Collisions at $\sqrt{s_{\rm NN}}$=200 GeV. Phys. Rev. Lett., 112(25):252301, 2014. doi: 10.1103/PhysRevLett.112.252301.

[81] PHENIX Collaboration. Cold-nuclear-matter effects on heavy-quark production in d+Au collisions at $\sqrt{s_{\rm NN}}$ =200 GeV. Phys. Rev. Lett., 109(24):242301, 2012. doi: 10.1103/PhysRevLett.109.242301.

[82] ATLAS Collaboration. Centrality and rapidity dependence of inclusive jet production in $\sqrt{s_{\rm NN}} = 5.02$ TeV proton-lead collisions with the ATLAS detector. Phys. Lett. B, 748:392–413, 2015. doi: 10.1016/j.physletb.2015.07.023.

[83] ATLAS Collaboration. Measurement of the nuclear modification factor for high- p_T charged hadrons in p+Pb collisions with the ATLAS detector. Nucl. Part. Phys. Proc., 289-290:281–284, 2017. doi: 10.1016/j.nuclphysbps.2017.05.064.

[84] CMS Collaboration. Charged-particle nuclear modification factors in PbPb and pPb collisions at $\sqrt{s_{\mathrm{N\,N}}} = 5.02$ TeV. JHEP, 04:039, 2017. doi: 10.1007/JHEP04(2017)039.

[85] ATLAS Collaboration. Precision measurement and interpretation of inclusive W^+ , W^- and Z/γ^* production cross sections with the ATLAS detector. Eur. Phys. J., C77(6):367, 2017. doi: 10.1140/epjc/s10052-017-4911-9.

[86] ATLAS Collaboration. Measurement of charged-particle spectra in Pb+Pb collisions at $\sqrt{s_{\mathsf{NN}}} = 2.76$ TeV with the ATLAS detector at the LHC. JHEP, 09:050, 2015. doi: 10.1007/JHEP09(2015)050.

[87] ATLAS Collaboration. Measurements of the Nuclear Modification Factor for Jets in Pb+Pb Collisions at $\sqrt{s_{\mathrm{NN}}} = 2.76$ TeV with the ATLAS Detector. Phys. Rev. Lett., 114(7):072302, 2015. doi: 10.1103/PhysRevLett.114.072302.

[88] ATLAS Collaboration. Measurement of the nuclear modification factor for inclusive jets in Pb+Pb collisions at $\sqrt{s_{\mathrm{NN}}} = 5.02$ TeV with the ATLAS detector. Phys. Lett. B, 790:108–128, 2019. doi: 10.1016/j.physletb.2018.10.076.

[89] CMS Collaboration. Study of high-pT charged particle suppression in PbPb compared to *pp* collisions at $\sqrt{s_{NN}} = 2.76$ TeV. Eur. Phys. J. C, 72:1945, 2012. doi: 10.1140/epjc/s10052-012-1945-x.

[90] CMS Collaboration. Measurement of inclusive jet cross sections in *pp* and PbPb collisions at $\sqrt{s_{NN}} = 2.76$ TeV. Phys. Rev. C, 96(1):015202, 2017. doi: 10.1103/PhysRevC.96.015202.

[91] ALICE Collaboration. Constraints on jet quenching in p-Pb collisions at $\sqrt{\mathbf{s_{NN}}} =$ 5.02 TeV measured by the event-activity dependence of semi-inclusive hadron-jet distributions. Phys. Lett., B783:95–113, 2018. doi: 10.1016/j.physletb.2018.05.059.

[92] CMS Collaboration. Measurement of inclusive jet production and nuclear modifications in pPb collisions at $\sqrt{s_{\mathrm{NN}}} = 5.02$ TeV. Eur. Phys. J. C, 76(7):372, 2016. doi: 10.1140/epjc/s10052-016-4205-7.

[93] Constantin Loizides and Andreas Morsch. Absence of jet quenching in peripheral nucleus–nucleus collisions. Phys. Lett. B, 773:408–411, 2017. doi: 10.1016/j.physletb.2017.09.002.

[94] Xin-Nian Wang and Miklos Gyulassy. HIJING: A Monte Carlo model for multiple jet production in p p, p A and A A collisions. Phys. Rev. D, 44:3501–3516, 1991. doi: 10.1103/PhysRevD.44.3501.

[95] Torbjorn Sjostrand, Stephen Mrenna, and Peter Z. Skands. PYTHIA 6.4 Physics and Manual. JHEP, 05:026, 2006. doi: 10.1088/1126-6708/2006/05/026.

[96] ALICE Collaboration. Analysis of the apparent nuclear modification in peripheral Pb–Pb collisions at 5.02 TeV. Phys. Lett. B, 793:420–432, 2019. doi: 10.1016/j.physletb.2019.04.047.

[97] Carlos A. Bertulani, Spencer R. Klein, and Joakim Nystrand. Physics of ultra-peripheral nuclear collisions. Ann. Rev. Nucl. Part. Sci., 55:271–310, 2005. doi: 10.1146/annurev.nucl.55.090704.151526.

[98] STAR Collaboration. ρ^0 photoproduction in ultraperipheral relativistic heavy ion collisions at $\sqrt{s_{NN}} = 200$ GeV. Phys. Rev. C, 77:034910, 2008. doi: 10.1103/PhysRevC.77.034910.

[99] STAR Collaboration. ρ^0 Photoproduction in AuAu Collisions at $\sqrt{s_{NN}}$=62.4 GeV with STAR. Phys. Rev. C, 85:014910, 2012. doi: 10.1103/PhysRevC.85.014910.

[100] ALICE Collaboration. Coherent ρ^0 photoproduction in ultra-peripheral Pb-Pb collisions at $\sqrt{s_{\mathrm{NN}}} = 2.76$ TeV. JHEP, 09:095, 2015. doi: 10.1007/JHEP09(2015)095.

[101] PHENIX Collaboration. Photoproduction of J/psi and of high mass e+e- in ultra-peripheral Au+Au collisions at s**(1/2) = 200-GeV. Phys. Lett. B, 679:321–329, 2009. doi: 10.1016/j.physletb.2009.07.061.

[102] ALICE Collaboration. Coherent J/ψ photoproduction in ultra-peripheral Pb-Pb collisions at $\sqrt{s_{NN}} = 2.76$ TeV. Phys. Lett. B, 718:1273–1283, 2013. doi: 10.1016/j.physletb.2012.11.059.

[103] ALICE Collaboration. Charmonium and e^+e^- pair photoproduction at mid-rapidity in ultra-peripheral Pb-Pb collisions at $\sqrt{s_{\mathrm{NN}}}$=2.76 TeV. Eur. Phys. J. C, 73(11): 2617, 2013. doi: 10.1140/epjc/s10052-013-2617-1.

[104] CMS Collaboration. Evidence for light-by-light scattering and searches for axion-like particles in ultraperipheral PbPb collisions at $\sqrt{s_{\mathrm{NN}}} = 5.02$ TeV. Phys. Lett. B, 797:134826, 2019. doi: 10.1016/j.physletb.2019.134826.

[105] ATLAS Collaboration. Evidence for light-by-light scattering in heavy-ion collisions with the ATLAS detector at the LHC. Nature Phys., 13(9):852–858, 2017. doi: 10.1038/nphys4208.

[106] Carlos A. Bertulani and Gerhard Baur. Electromagnetic Processes in Relativistic Heavy Ion Collisions. Phys. Rept., 163:299, 1988. doi: 10.1016/0370-1573(88)90142-1.

[107] F. Krauss, M. Greiner, and G. Soff. Photon and gluon induced processes in relativistic heavy ion collisions. Prog. Part. Nucl. Phys., 39:503–564, 1997. doi: 10.1016/S0146-6410(97)00049-5.

[108] Gerhard Baur. Coherent photon-photon interactions in very peripheral relativistic heavy ion collisions. Eur. Phys. J. D, 55:265–269, 2009. doi: 10.1140/epjd/e2009-00019-7.

[109] V Gonçalves and Magno Machado. Diffractive photoproduction of Z^0 bosons in coherent interactions at CERN-LHC. Eur. Phys. J. C, 56:33–38, 07 2008. doi: 10.1140/epjc/s10052-008-0633-3.

[110] ATLAS Collaboration. Measurement of exclusive $\gamma\gamma \to \ell^+\ell^-$ production in proton-proton collisions at $\sqrt{s} = 7$ TeV with the ATLAS detector. Phys. Lett. B, 749: 242–261, 2015. doi: 10.1016/j.physletb.2015.07.069.

[111] ATLAS Collaboration. Measurement of dimuon production in ultra-peripheral Pb+Pb collisions at $\sqrt{s_{NN}} = 5.02$ TeV with the ATLAS detector. Technical report, CERN, 2016. URL https://cds.cern.ch/record/2157689.

[112] CMS Collaboration. Exclusive photon-photon production of muon pairs in proton-proton collisions at $\sqrt{s} = 7$ TeV. JHEP, 01:052, 2012. doi: 10.1007/JHEP01(2012)052.

[113] ATLAS Collaboration. Calorimeter Clustering Algorithms: Description and Performance. Technical Report ATL-LARG-PUB-2008-002. ATL-COM-LARG-2008-003, CERN, 2008. URL https://cds.cern.ch/record/1099735.

[114] ATLAS Collaboration. Electron reconstruction and identification in the ATLAS experiment using the 2015 and 2016 LHC proton-proton collision data at $\sqrt{s} = 13$ TeV. Eur. Phys. J. C, 79(8):639, 2019. doi: 10.1140/epjc/s10052-019-7140-6.

[115] ATLAS Collaboration. Improved electron reconstruction in ATLAS using the Gaussian Sum Filter-based model for bremsstrahlung. Technical Report ATLAS-CONF-2012-047, CERN, Geneva, May 2012. URL https://cds.cern.ch/record/1449796.

[116] ATLAS Collaboration. Optimization of electron likelihood identification in Pb+Pb collisions. Technical Report ATL-COM-PHYS-2016-1398, CERN, Geneva, 2016. URL https://https://cds.cern.ch/record/2217208.

[117] Simone Alioli, Paolo Nason, Carlo Oleari, and Emanuele Re. NLO vector-boson production matched with shower in POWHEG. JHEP, 07:060, 2008. doi: 10.1088/1126-6708/2008/07/060.

[118] Torbjorn Sjostrand, Stephen Mrenna, and Peter Z. Skands. A Brief Introduction to PYTHIA 8.1. Comput. Phys. Commun., 178:852–867, 2008. doi: 10.1016/j.cpc.2008.01.036.

[119] Hung-Liang Lai et al. New parton distributions for collider physics. Phys. Rev. D, 82:074024, 2010. doi: 10.1103/PhysRevD.82.074024.

[120] ATLAS Collaboration. Measurement of $W^{\pm}$ and Z-boson production cross sections in pp collisions at $\sqrt{s}$ = 13 TeV with the ATLAS detector. Phys. Lett. B, 759: 601–621, 2016. doi: 10.1016/j.physletb.2016.06.023.

[121] ATLAS Collaboration. Supporting note for two particle azimuthal correlation analysis in UPC events with ATLAS. Technical report, CERN, 2019. URL https://cds.cern.ch/record/2668489.

[122] Spencer R. Klein, Joakim Nystrand, Janet Seger, Yuri Gorbunov, and Joey Butterworth. STARlight: A Monte Carlo simulation program for ultra-peripheral collisions of relativistic ions. Comput. Phys. Commun., 212:258–268, 2017. doi: 10.1016/j.cpc.2016.10.016.

[123] ATLAS Collaboration. Electron and photon energy calibration with the ATLAS detector using 2015-2016 LHC proton-proton collision data. JINST, 14(03):P03017, 2019. doi: 10.1088/1748-0221/14/03/P03017.

[124] ATLAS Collaboration. Muon reconstruction performance of the ATLAS detector in proton–proton collision data at $\sqrt{s}$ =13 TeV. Eur. Phys. J. C, 76(5):292, 2016. doi: 10.1140/epjc/s10052-016-4120-y.

[125] ATLAS Collaboration. Luminosity determination in pp collisions at $\sqrt{s}$ = 8 TeV using the ATLAS detector at the LHC. Eur. Phys. J., C76(12):653, 2016. doi: 10.1140/epjc/s10052-016-4466-1.

[126] G. Avoni et al. The new LUCID-2 detector for luminosity measurement and monitoring in ATLAS. JINST, 13(07):P07017, 2018. doi: 10.1088/1748-0221/13/07/P07017.

[127] A. Valassi. Combining correlated measurements of several different physical quantities. Nucl. Instrum. Meth., A500:391–405, 2003. doi: 10.1016/S0168-9002(03)00329-2.

[128] Stefano Catani and Massimiliano Grazzini. Next-to-Next-to-Leading Order Subtraction Formalism in Hadron Collisions and its Application to Higgs Boson Production at the Large Hadron Collider. Phys. Rev. Lett., 98:222002, 2007. doi: 10.1103/PhysRevLett.98.222002.

[129] Stefano Catani, Leandro Cieri, Giancarlo Ferrera, Daniel de Florian, and Massimiliano Grazzini. Vector Boson Production at Hadron Colliders: A Fully Exclusive QCD Calculation at Next-to-Next-to-Leading Order. Phys. Rev. Lett., 103:082001, 2009. doi: 10.1103/PhysRevLett.103.082001.

[130] W. F. L. Hollik. Radiative Corrections in the Standard Model and Their Rôle for Precision Tests of the Electroweak Theory. Fortsch. Phys., 38:165–260, 1990. doi: 10.1002/prop.2190380302.

[131] Particle Data Group, K. A. Olive et al. Review of Particle Physics. Chin. Phys. C, 38:090001, 2014. doi: 10.1088/1674-1137/38/9/090001.

[132] Sayipjamal Dulat, Tie-Jiun Hou, Jun Gao, Marco Guzzi, Joey Huston, Pavel Nadolsky, Jon Pumplin, Carl Schmidt, Daniel Stump, and C. P. Yuan. New parton distribution functions from a global analysis of quantum chromodynamics. Phys. Rev. D, 93(3):033006, 2016. doi: 10.1103/PhysRevD.93.033006.

[133] L. A. Harland-Lang, A. D. Martin, P. Motylinski, and R. S. Thorne. Parton distributions in the LHC era: MMHT 2014 PDFs. Eur. Phys. J. C, 75(5):204, 2015. doi: 10.1140/epjc/s10052-015-3397-6.

[134] H1 and ZEUS Collaborations. Combination of measurements of inclusive deep inelastic $e^{\pm}p$ scattering cross sections and QCD analysis of HERA data. Eur. Phys. J. C, 75(12):580, 2015. doi: 10.1140/epjc/s10052-015-3710-4.

[135] S. Alekhin, J. Blümlein, S. Moch, and R. Placakyte. Parton distribution functions, α_s, and heavy-quark masses for LHC Run II. Phys. Rev., D96(1):014011, 2017. doi: 10.1103/PhysRevD.96.014011.

[136] ATLAS Collaboration. Measurements of top-quark pair to Z-boson cross-section ratios at $\sqrt{s} = 13, 8, 7$ TeV with the ATLAS detector. JHEP, 02:117, 2017. doi: 10.1007/JHEP02(2017)117.

[137] CMS Collaboration. Measurement of the differential cross section and charge asymmetry for inclusive $\mathrm{pp} \to \mathrm{W}^{\pm} + X$ production at $\sqrt{s} = 8$ TeV. Eur. Phys. J., C76 (8):469, 2016. doi: 10.1140/epjc/s10052-016-4293-4.

[138] ATLAS Collaboration. Z Boson Production in pp Collisions at $\sqrt{s} = 5.02$ TeV with the ATLAS detector at the LHC. ATLAS-CONF-2016-107. URL https://cds.cern.ch/record/2220375.

[139] Sayipjamal Dulat et al. New parton distribution functions from a global analysis of quantum chromodynamics. Phys. Rev. D, 93:033006, Feb 2016. doi: 10.1103/PhysRevD.93.033006.

[140] Stefano Catani and Massimiliano Grazzini. Next-to-next-to-leading-order subtraction formalism in hadron collisions and its application to higgs-boson production at the large hadron collider. Phys. Rev. Lett., 98:222002, May 2007. doi: 10.1103/PhysRevLett.98.222002.

[141] Stefano Catani, Leandro Cieri, Giancarlo Ferrera, Daniel de Florian, and Massimiliano Grazzini. Vector boson production at hadron colliders: A fully exclusive qcd calculation at next-to-next-to-leading order. Phys. Rev. Lett., 103:082001, Aug 2009. doi: 10.1103/PhysRevLett.103.082001.

[142] K. Kovarik et al. nCTEQ15 - Global analysis of nuclear parton distributions with uncertainties in the CTEQ framework. Phys. Rev. D, 93(8):085037, 2016. doi: 10.1103/PhysRevD.93.085037.

[143] Kari J. Eskola, Petja Paakkinen, Hannu Paukkunen, and Carlos A. Salgado. The EPPS16 nuclear PDFs. PoS, DIS2017:197, 2018.

[144] John M. Campbell, R. Keith Ellis, and Walter T. Giele. A Multi-Threaded Version of MCFM. Eur. Phys. J. C, 75(6):246, 2015. doi: 10.1140/epjc/s10052-015-3461-2.

[145] Constantin Loizides, Jason Kamin, and David d'Enterria. Improved Monte Carlo Glauber predictions at present and future nuclear colliders. Phys. Rev. C, 97(5):054910, 2018. doi: 10.1103/PhysRevC.97.054910,10.1103/PhysRevC.99.019901. [erratum: Phys. Rev.C99,no.1,019901(2019)].

[146] ATLAS Collaboration. Measurement of $W^{\pm}$-boson and Z-boson production cross-sections in pp collisions at $\sqrt{s} = 2.76$ TeV with the ATLAS detector. CERN-EP-2019-095, 2019.

[147] ATLAS Collaboration. Measurement of the inclusive $W^{\pm}$ and Z/gamma cross sections in the electron and muon decay channels in pp collisions at $\sqrt{s} = 7$ TeV with the ATLAS detector. Phys. Rev. D, 85:072004, 2012. doi: 10.1103/PhysRevD.85.072004.

[148] ALICE Collaboration. Transverse momentum spectra and nuclear modification factors of charged particles in pp, p-Pb and Pb-Pb collisions at the LHC. JHEP, 11:013, 2018. doi: 10.1007/JHEP11(2018)013.